Template-assisted synthesis and characterisation of quasi-one-dimensional ceramic nanomaterials

TECHNISCHE UNIVERSITÄT DARMSTADT

Vom Fachbereich Chemie
der Technischen Universität Darmstadt

zur Erlangung des akademischen Grades eines

Doktor rerum naturalium (Dr. rer. nat.)

genehmigte
Dissertation
eingereicht von

Dipl.-Chem. Mikhail Pashchanka
aus Minsk, Belarus

Referent: Prof. Dr. J.J. Schneider
Korreferent: Prof. Dr. R. Riedel
Tag der Einreichung: 26.05.2010
Tag der mündlichen Prüfung: 12.07.2010

Darmstadt 2010
D17

Acknowledgements

First of all, I would like to express my thanks to my family and friends for the encouragement during the last four and a half years, and especially to my mother, who visited me from time to time during my stay in Germany.

I would like to thank my advisor Prof. Dr. J.J. Schneider for his guidance and the opportunities that were provided both in our group and in collaboration with some other scientific institutions.

I thank Prof. Dr. R. Riedel for valuable advices during common work on a project and for his agreement to be a co-referee of the present thesis.

I appreciate the help, comments and suggestions from my colleagues: Dr. J. Engstler, Dr. R.C. Hoffmann, Dr. J. Khanderi, Dr. A. Issanin, Dr. G. Cherkashinin, Dr. B. Corzilius, Dr. O. Burghaus, Dr. P. Komissinskiy, Dr. M. Nowotny, and Dipl.-Ing. I. Balog. I would like to say many thanks to Dr. E. Rikowski and Dr. T. Herntrich for helping me with texts in German.

I am very grateful to Dr. A. Gurlo for the opportunity to perform experiments at ESRF in Grenoble and for reading of some my drafts and manuscripts, as well as for other common experiments, which not only provided useful results for the present work but also were a great educational experience. I also would like to thank Dr. J. Grattage for her assistance at ESRF in Grenoble.

I express my thanks to Dr. P. Kraikivskii for his help in interpretation of ESR spectra and for the fruitful discussion of some other theoretical and practical aspects of the work.

I am grateful to Dr. D. Dzivenko and Dr. O. Avrutina for support during my stay in Darmstadt.

Results from this work already published or submitted for publication

[1] M. Pashchanka, J. Engstler, J. J. Schneider, V. Siozios, C. Fasel, R. Hauser, I. Kinski, R. Riedel, S. Lauterbach, H. J. Kleebe, S. Flege, W. Ensinger, *European Journal of Inorganic Chemistry* **2009**, 3496.

[2] M. Pashchanka, R. C. Hoffmann, J. J. Schneider, *Physics, Chemistry and Application of Nanostructures* **2009**, 373.

[3] M. Pashchanka, R. C. Hoffmann, J. J. Schneider, *Journal of Materials Chemistry* **2010**, *20*, 957.

[4] M. Pashchanka, R. C. Hoffmann, A. Gurlo and J. J. Schneider, *"Molecular based chimie douce approach to 0D and 1D indium oxide nanostructures. Evaluation of their sensing properties towards CO and H_2"*, submitted to *Journal of Materials Chemistry*

Talks and conferences:

[1] Scientific Colloquium for Graduate Students. Joint Workshop of the Inorganic Chemistry Department of TU Darmstadt and Merck KGaA, 13 March 2008, Darmstadt, Germany

[2] TU Darmstadt – METU Ankara, Joint Graduate Workshop on Nanotechnology, 28 April 2009, Darmstadt, Germany

[3] International Conference NANOMEETING-2009, Talk № 6 in '*Chemistry of Nanostructures'* section, 26-29 May 2009, Minsk, Belarus

Table of content

Abbreviations and definitions

BET	Brunauer-Emmet-Teller
EDX	Energy Dispersive X-ray Analysis
ESR	Electron Spin Resonance
FTIR, IR	(Fourier Transform) Infrared Spectroscopy
HERFD	High Energy Resolution Fluorescence Detected Spectroscopy
PAOX	porous anodic aluminium oxide
Q0D	quasi zero dimensional
Q1D	quasi one dimensional
SAED	Selected Area Electron Diffraction
SEM	Scanning Electron Microscopy
TEM	Transmission Electron Microscopy
XANES	X-ray Absorption Near Edge Structure
XPS	X-ray Photoelectron Spectroscopy
XRD	Powder X-ray Diffraction
D	mean Scherrer crystallite size [nm]
D_{rot}	rotation Moiré period [nm]
d	interplanar spacing [nm, Å]
G	conductance
j	current density [mA · cm^{-2}]
p	pressure [bar]
R	resistance [Ω]
r	particle radius [Å, nm]
t	time [s, h]
Z	atomic number
ρ	density [g · cm^{-3}]
λ	wavelength [nm]
λ_D	Debye screening length [m]

1 General introduction

Synthesis and characterisation of novel nanomaterials have become an important task over the last few years.[1] Since many chemical and physical properties of a substance in the surface layer and near-surface region are different to those in the volume, tiny particles and their assemblies often have special behaviours not observed for the bulk.[2]

The contribution of the surface behaviour (surface energy) of composite particles into bulk properties is determined by the degree of dispersion, as the specific surface area is increasing with the decrease in size. This correlation is clearly illustrated, for example, by the influence of filaments in composite materials, which has the maximal effect at the filament grain dimensions between 1 and 100 nm. A transition from atoms or molecules to the bulk takes place in this size range, and the number of surface atoms or ions becomes a significant fraction of the total number of the units. However, since surface properties do not change linearly with size below 1 nm, one cannot predict the permanent improvement of physical properties just by further reduction of particles dimensions.

Not only particles size, but also their shape is of great importance for the preparation of promising materials with tailored properties. As particles become more anisometric, a lower concentration of them is required to form a three-dimensional pattern. Thus many important characteristics of structural composites, such as the electric conductivity, elasticity and heat resistance may be influenced just changing the geometry of particles.

Elongated units (e.g. nanoscale rods and tubes) may find applications as sensors and catalysts since this type of morphology provides a significant increase of specific surface area.[3] In this regard, the fabrication of quasi one-dimensional (Q1D) nanomaterials (here ‘quasi’ means that the nanostructures still remain too thick to observe quantum confinement effects), characterized by a high length-to-width aspect ratio, has attracted special attention. The aspect ratio is considered to be larger than 20 for fibers and nanowires, and smaller than 20 for whiskers and nanorods. This classification is often a little arbitrary, but nevertheless helpful to compare and describe the dimensions. In many cases, nanotubules, nanocables, as well as segmented or core-shell heterostructures are also considered as one-dimensional structures.[4]

The techniques for the synthesis and formation of one-dimensional nanostructured materials can be grouped into four categories:[1]

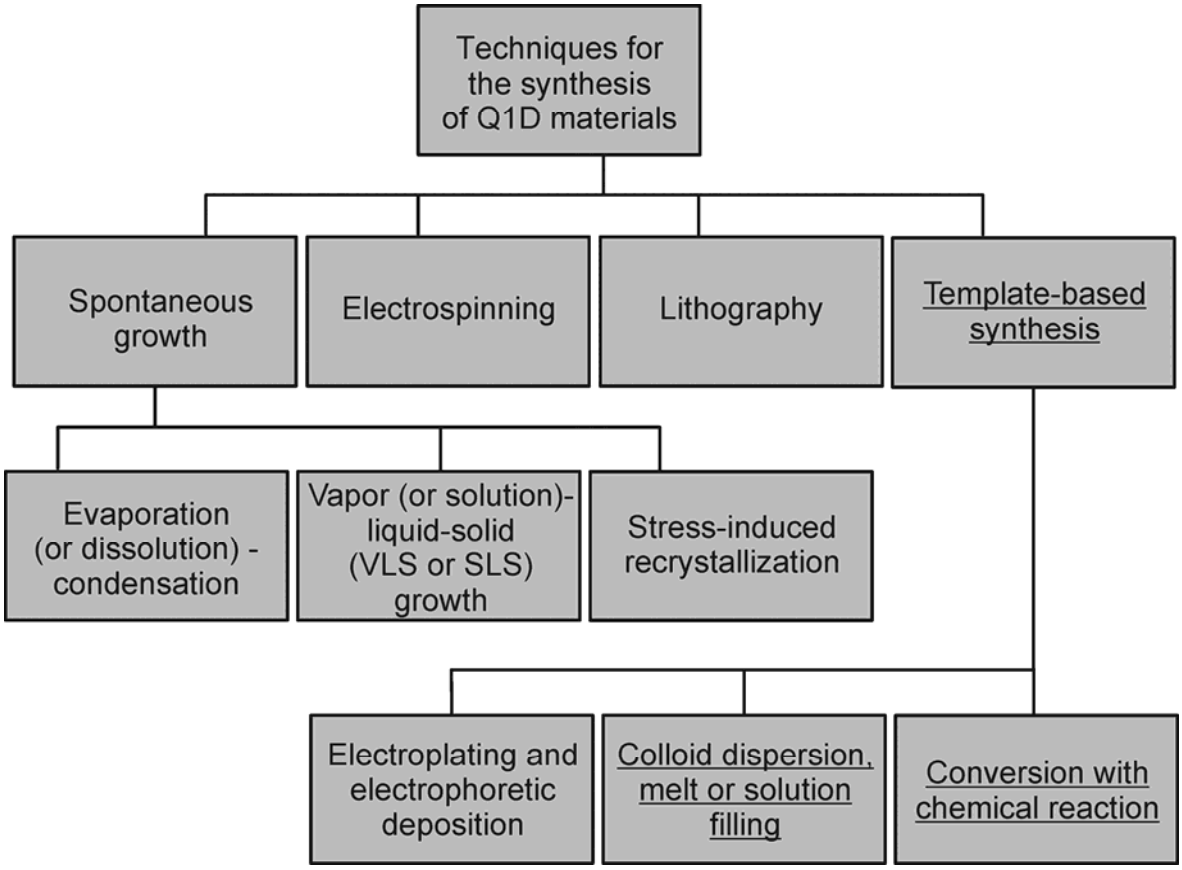

Scheme 1. Classification of the synthetic methods, used for Q1D nanostructures fabrication; underlined are the techniques, which are used in this work.

When self-assembly or lithographic method is inconvenient or does not provide desired results, the template-based approach can be alternatively used.[5, 6] Template directed wet routes (sol-gel, or chemical polymerisation techniques based on the chemical conversion of a liquid precursor within the pores of a membrane[5]) have been intensively explored as a simple and relatively inexpensive alternative to the chemical vapor deposition technique.

Coaxial cylindrical channels in some porous templates enable one to produce final molded products in the form of a columnar array. Such nanomaterials, combining properties of one-dimensional units and the three-dimensional aligned structures, can potentially provide high efficiency in sensing and electrode applications. In comparison with non-template techniques, template-directed methods offer low processing temperatures and do not necessarily require vacuum conditions. These

features often determine the choice of the template-based method for the fabrication of vertically aligned nanowires on a flexible polymeric substrate. The main possible field of application of these methods is the fabrication of various devices, e.g. micro- (or nano-) electromechanical systems, photo-electronic units, non-volatile memory storages or field-emission displays.

In contrast to spontaneous growth that commonly results in the formation of single-crystal inorganic nanowires or nanorods, template-based synthesis (Scheme 2) mostly produces polycrystalline or even amorphous products.

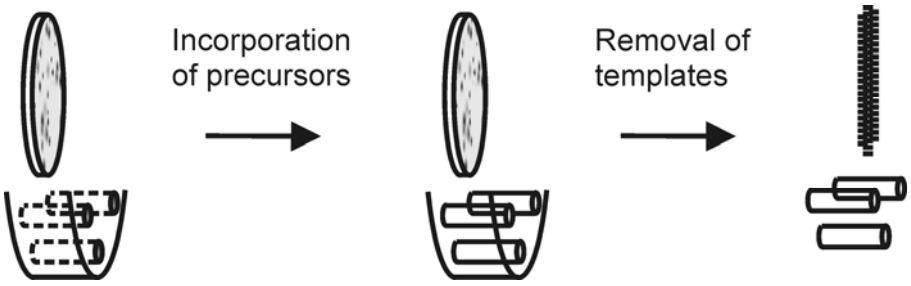

Scheme 2. The synthetic process of template-based approach

There are several types of useful templates for the fabrication of one-dimensional nanostructures: porous anodic alumina films, nuclear track-etched polymeric membranes, mesoporous silicate thin films prepared via sol-gel technique over a lithographically patterned (100)-orientated Si substrate (this is not a spontaneous pore formation, but the method allows to engineer the pore geometry),[7] as well as some other mesoporous or microporous materials with high surface areas, adjustable pore sizes and narrow pore size distributions (e.g. hexagonal arrays of uniform pores in aluminosilicate MCM-41,[8, 9] or replicas of SBA-15 silica rods[10]).

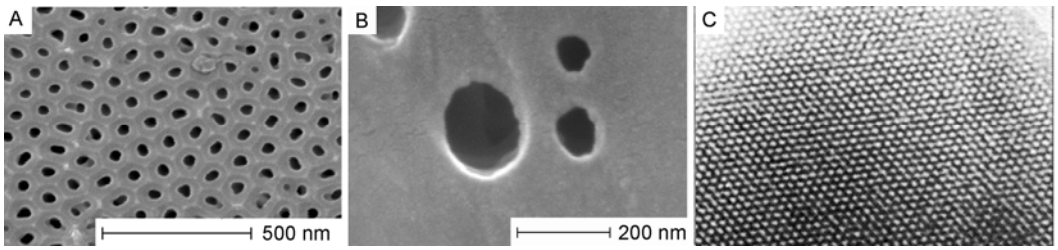

Fugure 1. SEM images of porous anodic alumina templates (A) track-etch polycarbonate films (B) and a TEM micrograph of MCM-41 with pore size of ca. 4 nm (C[9])

In the present study, two types of templates have been employed: porous aluminium oxide (PAOX) and track-etched polycarbonate films.

Porous aluminium oxide often serves for the preparation of nanowires and nanotubules from liquid precursors. A set of empirically grounded aluminium anodization conditions combined with the chemical etching methods may be used to control the size and the ordering of the straight cylindrical pores of the oxide films and, consequently, of the final molded structures. Additionally, porous alumina is resistant to organic solvents and can retain the porous structure with monodisperse pore diameters at elevated temperatures that may be needed for precursors thermal cure.

Polycarbonate track-etched membranes are used in many laboratories as filters and are commercially available in a wide range of pore diameters. A thin film of the polymer is bombarded with high-energy accelerated ions in a cyclotron to create straight damage tracks. The tracks are subsequently etched to achieve the pores of different size. Due to the relatively low thermal stability, polycarbonate track-etched membranes are mainly used for low-temperature methods of target substance impregnation (e.g. electrochemical deposition from a solution).

The subject of the present work is the fabrication and characterisation of tailored quasi one-dimensional (Q1D) amorphous and polycrystalline ceramic materials. All the products under study were made by means of thermal decomposition of liquid precursors molded by mesoporous templates, or solid precursors, impregnated into the pores in form of liquid solutions. Both the commercially available inorganic and polymeric membranes and self-prepared anodic alumina films with a smaller pore size have been used. All materials of interest were infiltrated into pores by the direct filling method, and capillary action was the only driving force.

The compositional and structural changes in the resulting tailored ceramic nanomaterials were followed by diverse optical, spectral and structural characterisation methods. Examination was carried out to find the correlation between structure and composition properties of Q1D materials and the presence of various components in the template. A wealth of previously obtained characterisation results makes it now possible to compare the properties of a nanostructured Q1D samples and bulk species or unmolded powders made from the same precursors.

Further questions arise when we compare bulk and nanostructured materials:

- Did the chemical composition of molded materials change in comparison with known bulk counterparts due to the possible reactivity of a template, or a reagent, which is used for the isolation of nanostructures from a template?
- If no chemical composition change is observed, did the desired properties of nanostructured materials improve specifically due to the Q1D shaping?

2 Issues to be addressed in this work

The key issue to be addressed is the possibility of forming of Q1D-structures with desired dimensions, chemical composition, purity and physical-chemical properties using a tailored porous template.

The materials of interest are following:

- silicon-based carbon containing ceramics (SiC, SiOC), which can be potentially applied as a catalyst carrier or elements in micro- or nano-electromechanical systems;
- magnesium oxide, which has been extensively explored for catalytic applications;
- indium oxide, which is an *n*-type semiconductor showing gas sensing properties;
- zinc oxide for photoelectronic devices, as well as Mn-doped ZnO (the key material to room-temperature ferromagnetics) or Cu-doped ZnO (the possible route to tune the band gap in zinc oxide and, presumably, even to synthesise *p*-type ZnO).

In the section 4.1 of this work, the characterisation of routinely produced PAOX templates with SEM, XRD, BET surface analysis, and TGA is given. This preliminary investigation gives information about the available pore sizes, and helps to gain a better understanding of possible chemical interactions between the pore walls and a precursor. Some aspects of chemical etching and thermal treatment of PAOX templates from different electrolyte solutions are discussed.

Section 4.2 focuses on the detailed study of PAOX template assisted formation of aligned ceramic nanowires starting from commercially available silicon-based polymers (KiON Ceraset™ and Starfire Systems SP Matrix™). The template-based

synthesis was carried out in alumina membranes with pore diameters of 20 and 40 nm (before the wet etching step).

In the section 4.3, track-etched polycarbonate templates, traditionally used by other working groups for low-temperature replication methods only, are studied. The majority of pre-ceramic precursors cannot be thermally converted into the waterless crystalline compounds within polycarbonate without destroying of the porous morphology. The thermal properties of the Whatman Nuclepore™ filters are thoroughly investigated to draw conclusions about their applicability, as well as the optimal experimental conditions for each replication experiment further in the present work.

Synthesis of polycrystalline magnesium oxide nanorods using track-etched polycarbonate films and magnesium oximato complex solution in ethanol as starting materials is discussed in section 4.4. Metal oximato complexes of corresponding metals were chosen as precursors for the inorganic oxide materials since they are available via straightforward synthetic procedures and yield a wide range of metal oxides at relatively low conversion temperatures. This line of investigation was previously developed in our group.[11]

In section 4.5, the template based approach to the synthesis of polycrystalline indium oxide nanotubes using track-etched polycarbonate films and a novel indium oximato complex is described. The aim of performed sensor tests was to study gas sensors based on chemically identical material (In_2O_3 derived from the same precursor) but with different morphology (nanotubes and Q0D particles), to evaluate the role of an increased accessible surface area of Q1D nanomaterials in comparison with Q0D particles.

In section 4.6, template-based synthesis of undoped ZnO and doped ZnO:Mn nanorods is discussed. The synthesis is carried out at low temperatures of 160-180 °C, and the polymeric template can then be selectively removed in an organic solvent, which does not damage the metal oxide. Structure of the material, as well as the oxidation state and chemical surrounding of manganese cations are studied with spectroscopic (XPS, FTIR) and resonance (ESR) methods.

Section 4.7 injuries into the synthesis of polycrystalline nanorods aggregated of Cu-doped ZnO nanoparticles with the help of polycarbonate templates. Spectroscopic methods confirm the oxidation state (II) of doping Cu ion (XANES/HERFD), as well as the band gap contraction increasing with the doping concentration (PL).

Some results, which are supplementary to the declared main objectives of the work, are presented in sections 4.1.4, 4.2.3, and 4.8. The aim of the described chemical functionalisation of porous alumina was to increase the affinity of template interior to silicon-based precursors. Experiments with pulse current anodisation were made to optimize PAOX templates morphology. An attempt to produce core-shell Q1D heterojunctions is also presented.

3 Literature survey

3.1 Porous anodic aluminium oxide (PAOX) templates

3.1.1 Historical sketch and phenomenological theories of pores formation

The electrochemical oxidation of aluminium and its alloys belongs to the most familiar and well-studied methods of corrosion and abrasion protection and decorative coating.[12, 13] The main characteristics of commercially used aluminium oxide films were the high porosity and uniform pore size distribution, which made them a good base for colouring by infiltration of pigments.[14] The ease of organic pigments adsorption and electrochemical coloration (impregnation of Ni^{2+} used in industry) also suggested that the pores in anodic alumina can be filled with other organic or inorganic materials for the purpose of nanochannels replication.[15]

Electrolytes in which the formed oxide film is slightly soluble (sulphuric, oxalic, phosphoric, chromic acid in various concentrations, pH < 4) are known to produce porous films, whereas those in which it is insoluble (e.g. boric acid, ammonium borate or tartrate, neutral or slightly acidic pH values around 5-7) produce barrier-type films.[16] The chemical reactions in the porous alumina growth are (see, for example, [17]):

Anode

$2Al + 3H_2O \rightarrow Al_2O_3 + 6H^+ + 6e^-$

(Dissolution of alumina)

$Al_2O_3 + 6H^+ \rightarrow 2Al^{3+} + 3H_2O$

Cathode

$6H^+ + 6e^- \rightarrow 3H_2\uparrow$

The presence of at least three types of aluminium oxide was found in the formed films: hydrated boehmite AlO(OH) at the oxide-electrolyte interface, irregular patches of crystalline γ-Al_2O_3, and the amorphous oxide constituting the majority of the film.
The current density-time transients (Fig. 2) observed for a constant voltage step preparation of a porous and a barrier film showed that at a certain point *A* two curves begin to diverge. The pore initiation occurs at some point close to *A*, and requires the thickness of a barrier layer formed up to this point.

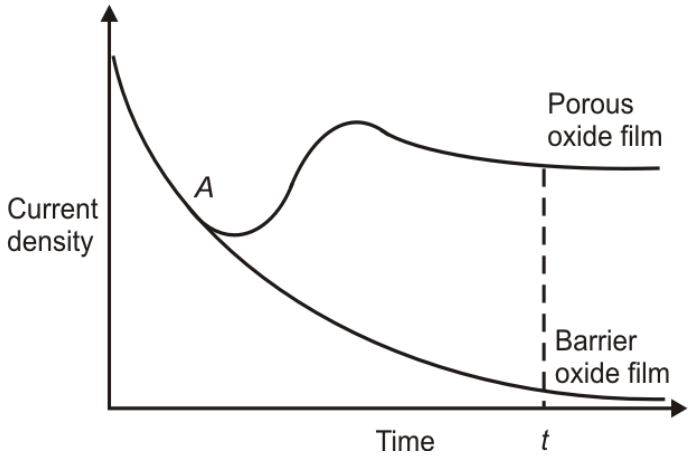

Figure 2. Dependence of the current density on time, modified from[16]: *A*, the point at which the divergence of two curves occurs, may be related to pore initiation phenomenon; time *t* is typically 25 s for a 15 V step application in 15 % H_2SO_4 (aq).

The first systematic microscopic study of the films morphology is found in the classical work of Keller, Hunter and Robinson.[18] The essential points of the proposed structure are: each pore is star-shaped and lies in the centre of a hexagonal oxide cell. After oxide stripping in phosphochromic acid, the metal surface was covered with a large number of hemispherical depressions, density corresponds to the density of pores.
The geometrical model of Keller et al. was confirmed with some exceptions.[19] The pores were found to be 'trumpet-shaped' (Fig. 3), presumably, due to the chemical dissolution of the pore walls at the outer surface. The pore diameter, the cell diameter and the barrier layer thickness (see Fig. 4) were found to be interrelated and dependent on the formation voltage. No evidence has been found for star-shaped pore sections.

Figure 3. Illustration of the 'trumpet-shaped' pore morphology

Thompson[20-22] and coworkers produced a rather comprehensive theory of porous alumina films formation in the period between 1978 and 1987. The results of other researchers may be included in the framework of this theory.

The morphology and composition of porous films formed in H_3PO_4 solutions were studied.[20] It was confirmed that the barrier layer thickness is the function of the applied voltage. A flattening of the initially rough aluminium surface was attributed to the more rapid growth of the barrier layer at the ridges.

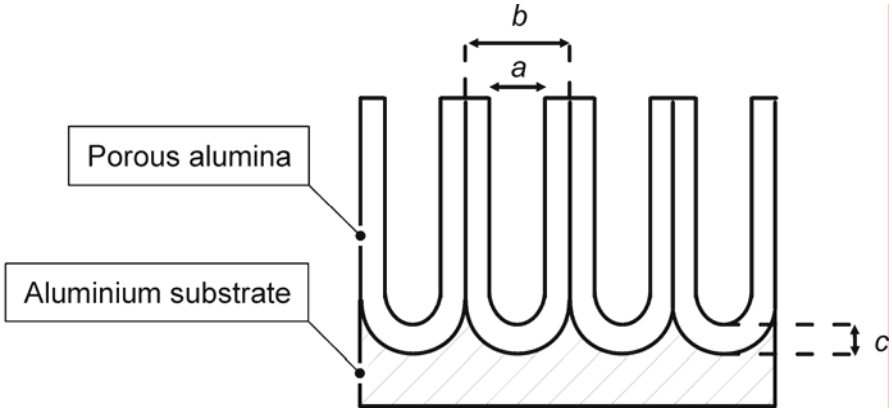

Figure 4. Basic geometric parameters of porous alumina films: *a* – pore diameter, *b* – cell diameter (inter-pore distance), *c* – barrier layer thickness.

The proposed model included two simultaneous processes:

- diffusion of Al^{3+} ions from metal and O^{2-} and OH^- ions from solution towards metal/film interface and formation of new oxide there;
- ejection of hydrated Al^{3+} ions to the solution.

Solid alumina forms afterwards by deprotonation of hydrated Al^{3+} ions, aggregation and thence precipitation from initially colloidal aqueous alumina. This aggregation of Al^{3+} ions with phosphate ions can produce negatively charged stable colloidal

particles, which are deposited under the electric field above the phosphate-free layer to produce an outer layer of fine microcrystallites.

The most important aspects of the pores development mechanism were postulated:[21]

- electropolishing, i.e. smoothing of aluminium foils in the mixture of ethanol and perchloric acid (normally 4:1 by volume) at high current densities and temperatures under 10 °C, leaves a slightly scalloped Al surface;
- a scalloped 'native' barrier oxide grows over this scalloped surface;
- as anodization starts, pores will start at cracks and imperfections in the surface, leaving an electric field concentrated below the regions where the oxide film is thinner, thus,
- aiding the local dissolution of oxide;
- this new pore bottom deepens, and a 'major' pore forms, at the expense of the former shallow pores.

The average field across the barrier layer determines the barrier film growth rate at the metal/oxide interface, while at the oxide/electrolyte interface the local field at the pore bottom determines the dissolution rate. The film growth rate is constant, while the dissolution rate increases as the pore curvature radius decreases. Thus, the film dissolution rate enlarges the undersize pores, and slows if the pore radius becomes too big. These two competing processes are supposed to keep the pore radius constant.

The voltage-time diagrams under constant current density conditions but for different Faraday current efficiency values were analysed.[22] A barrier film is developed at a current efficiency above approximately 60% [23, 24]. With reduction in current density *j*, the efficiency decreases, until a so-called critical current density is achieved, when a porous anodic film results. The ionic current density was shown to be proportional to the slope of the voltage-time curves.[22] The following hypothesis was proposed: at the critical current density the formed Al^{3+} cations remain outwardly mobile (which is the necessary condition for the porous anodic alumina formation), otherwise Al^{3+} would return and 'heal' pores at initial stages of development.

Some differences in the first-time (flat aluminium sheets) and the second-time (pre-textured aluminium sheets) anodization current density – time (*j* – *t*) curves (Fig. 5) were found.[25] First, the minimum *j* is larger for the textured sheets. Next, there is no

current overshoot for textured sheets. Last, the voltage increases more slowly for the second anodization.

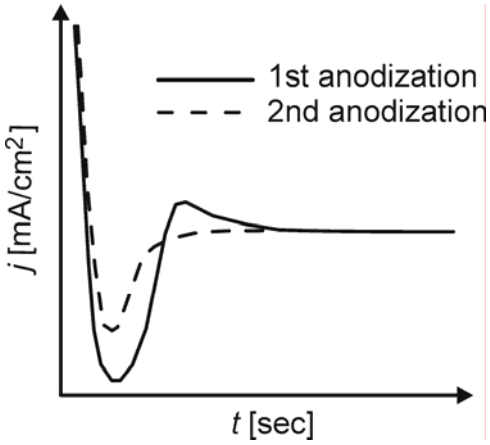

Figure 5. Current-time curves for first and second anodisation (modified from [25]).

In microscopic studies, the hexagonally ordered regions were found to form domains. The average domain area was found to be a linear function of the time.[25]

3.1.2 Specific anodization conditions for size tailoring and hexagonal arrangement of pores

The highly hexagonally ordered porous structures were obtained in a 0.3 M oxalic acid ($H_2C_2O_4$) solution at 40 V constant voltage and temperature 0 °C.[26] The anodic oxidation was carried out over a period of 160 hours. Similar ordered films were obtained under following conditions: at 25-27 V in a 5 wt.-% sulphuric acid (H_2SO_4) solution at 0 °C, at 40 and 60 V in a 0.3 M $H_2C_2O_4$ solution at 17 °C, and at 80 V in a 0.04 M $H_2C_2O_4$ solution at 3 °C, as well as in a 10 wt.-% phosphoric acid (H_3PO_4) solution at 195 V and temperature 0 °C.[27-29] In all cases the cell size had a good linear relationship with the applied voltage, where the proportionality constant was 2.5 $nm \cdot V^{-1}$. At the same time, ordering of the pores was considered as a function of the porous layer thickness. The voltage was decreased from 27 V to 25 V, 23 V and 20 V, in order to decrease the pore diameter, but the oxidation time was prolonged to achieve the same film thickness 25 ± 3 µm in all cases and to save the highly

ordered structure.[27] It was found, nevertheless, that a lower potential at a longer oxidation time and an equal film thickness gives a worse ordering of the pores.

To promote the hexagonal arrangement, the high current density (> 500 $mA \cdot cm^{-2}$) electropolishing of aluminium substrate is frequently performed.[30] This procedure is carried out using a mixture of ethanol and concentrated perchloric acid (4:1 by volume) at temperatures below 10 °C. After electropolishing, aluminium foils have an almost flat surface, exhibiting small etch pits and bumps, which could be seeds for pore nucleation. To create long-range hexagonal ordering in thin porous films, the two-step process can be used. After the first long anodization, the film is removed in a mixture of phosphoric and chromic acid. Due to this process, a scalloped surface is prepared on aluminium substrate after the first step and can act as initiation sites for hole development and the hexagonal arrangement during the second anodic oxidation.

The pores diameter obtained during anodization in 15% H_2SO_4 is very small [17], it equals to approximately 20 nm at 15 V and decreases to about 10 nm at 10 V. As can be seen from the TEM images (Fig. 6)[17], there is no naturally occurring hexagonal ordering of the holes at lower voltage.

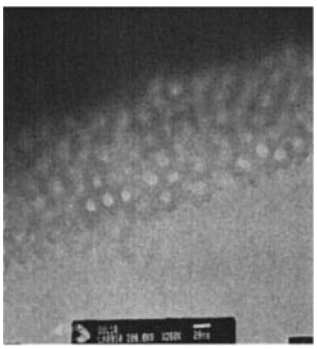

Figure 6. TEM image of 10 nm pores, obtained from sulphuric acid solution.[17]

Shallow concaves were formed on aluminium by replicating of a two-dimensional array of Fe_2O_3 nanoparticles with diameters 11±1.3 nm. [31] The following oxidation in 0.3 M H_2SO_4 at 16 °C for 15 min resulted in films with a pore size under 10 nm and the interpore distance around 13 nm.

Selected available pore diameters are presented in Tab. 1.[6]

Table 1 Pore sizes and experimental conditions from selected literature sources.

Reference	Pore diameter, nm	Voltage, V	Temperature, °C	Type and concentration of the electrolyte
[32]	5-8	15	10	10 % H_2SO_4
[33]	22	27	2	3 M H_2SO_4
[32]	30	40	20	3% $H_2C_2O_4$
[34]	33	25	10	0.3 M H_2SO_4
[35]	35	40	12	0.3 M $H_2C_2O_4$
[36]	35	18-25	1	20% H_2SO_4
[37]	40-50	-	-	$H_2C_2O_4$
[38]	45	40	0	0.2 M $H_2C_2O_4$
[39]	50	45	-	0.3 M $H_2C_2O_4$
[34]	67	40	1	0.3 M $H_2C_2O_4$
[36]	70	30-60	1	0.3 M $H_2C_2O_4$
[32]	150	130	7	10 % H_3PO_4
[34]	267	160	3	10 % H_3PO_4

3.2 Track-etched polycarbonate templates

Track-etched polymeric templates are made by exposing organic films to a heavy ion source (U, Xe). The incident ions form randomly located holes on the surface of the film (around 10^9 pores·cm^{-2}) and straight track channels in the volume, which can be subsequently chemically etched to enlarge the channels to a desired size.

Polycarbonate has been used for the formation of track-etched membranes since the 1970's. The advantage of this polymer in comparison with other alternatives, such as polyethylene terephthalate or polypropylene, is that the pore sizes up to 0.01 μm are available. On the other hand, this material is characterised by a lower wettability and a lower resistance to organic solvents.[40] Porous track-etched polycarbonate films are commercially available as filters with various channel diameters ranging from 0.01 to 12 μm (e.g. Whatman Nuclepore® filters with 0.03 or 0.1 μm nominal pore sizes, used in this work).

Polycarbonate filters have been widely used for the low-temperature template-based synthesis of Q1D materials.[41, 42] One of the important aspects to be mentioned here is the generally observed cigar-like morphology of pores in polycarbonate films, which are always wider inside than at the surface. It is supposed, that, along with the primary damage from the ion track, destruction from generated secondary electrons (electronic collision cascade) takes place as well. The resulting small polymeric fragments are then easily etched in the positions far from the track center.[43] This effect is also known in e-beam lithography.

To carry out a reaction of a precursor thermal decomposition within the pores, a detailed knowledge of the thermal behaviour of polycarbonate is important. Polycarbonate degradation was studied in the range 300-389 °C, the products were analysed by mass-spectrometry and gas chromatography.[44] The registered products were carbon dioxide, carbon monoxide, methane, phenol, diphenyl carbonate, 2-(4-hydroxyphenyl)-2-phenylpropane and bisphenol-A. At 360 °C, the analysed gas mixture was 95% CO_2, 3% CO, and 2% CH_4. At higher temperatures, the proportions of CO_2 decreased slightly. The degradation in air is studied and decomposition products at temperatures above 400 °C are listed: phenol, *p*-cresol, 4-ethylphenol, 4-isopropylphenol, tetramethylbutylphenol, bisphenol-A.[45] According to the TGA curve of polycarbonate decomposed in N_2 atmosphere, presented in [46, 47], the weight loss starts at the temperature above 300 °C, and the constant mass carbon residue appears at 550-600 °C. Among the decomposition products, CO_2, phenols, and other mentioned in previous works are stated. No obvious weight loss until 300 °C is visible in TG and DTG. [47]

3.3 Synthesis of Q1D nanostructures from materials, relevant to the present work – prerequisites and previous studies

3.3.1 Silicon-based carbon-containing ceramics

Silicon-based ceramic materials are of particular interest for the preparation of micro- and nanoscale structures and composites.[48-51] Owing to strong covalent bonds, silicon carbide, carbide-nitride and other doped systems have high cohesion and surface tension values, and, as a result, good mechanical strength and low volatility at high temperatures. Specific electric properties and high chemical resistance make

these materials attractive for electronic devices and harsh environment applications.[52-54] In particular, SiCN-based systems can be applied at high temperatures and in harsh environments and do not tend to deform even under mechanical load up to 1000 °C.

From a synthetic point of view their preparation via pyrolytic conversion of liquid organosilicon polymers as precursors is attractive. These substances are now commercially available as stable, low viscosity liquid thermosetting resins, and have significantly lower temperatures of the transition into ceramic components (800-1100°C) than in chemical metallurgical processes. Due to the low surface tension, those liquid precursors are also good candidates for coating and capillarity-driven infiltration of porous media.

Silicon-based ceramic nanorods and nanotubes were synthesized by a variety of different methods such as chemical vapour deposition (CVD),[55] carbothermal reduction,[56, 57] sol-gel,[58, 59] catalytic growth on metal particles[60] as well as via infiltration of silicon containing polymers in templates.[49, 61]

The fabrication of hollow SiC tubes from organosilicon polymers in PAOX templates has already been reported.[49-51] However, commercially available macroporous membranes (Whatman Anopore filters, nominal pore diameter 200-300 nm) have only been employed, and the advantage of pore size tailoring has not been used yet. The rod-like structures were obtained afterwards by a series of tube infiltrations followed by thermal cure. It would be definitely interesting to produce these structures with smaller diameters in order to explore the effects of size on the properties of these materials.

Metal oxides often serve as passive fillers during a pre-ceramic polymer thermolysis without any signs of chemical interaction.[62] However, it has been claimed that the specific composition of the pore walls in PAOX makes them active participants of different reactions, rather than an inert matrix.[63] Acidified PAOX surface is covered with additional Lewis acid cites, which are efficient host centres for Lewis bases, such as unsaturated organic compounds. Those Lewis acid cites play an important role during the pyrolytic conversion of organic precursors into carbon-like composite materials over PAOX supporting structure.[63] Another example of the interaction with a Lewis basis is the application of PAOX films as substrate in metal-oxide ammonia sensor fabrication.[64]

Aluminium oxide obtained from acidic aqueous solutions by means of their pH increase (process, similar to PAOX membranes synthesis) usually has a complex composition, expressed as $AlO(OH)\cdot nH_2O$. The water-free adsorbent can be subsequently produced by calcination at 300-400°C, but even the evacuation of alumina samples to 650°C leaves approximately 10 per cent of the surface covered with hydroxyl groups.[65] At the same time, many organosilicon polymers are hydrolytically sensitive substances. High oxygen content in resulting ceramics (over 5 wt %[62]) will lead to structural changes and harmfully influence its properties. The reported oxygen content in SiC nanotubes prepared from a liquid precursor in non dehydrated membranes was 3,6 wt % (6 mol %), which is already close to the critical value.[50]

3.3.2 Magnesium oxide

Crystalline magnesium oxide is a widely applied functional material, which possesses a rather high chemical inertness, thermal stability, low heat capacity, high dielectric constant and low refractive index. It has been successively used as a reactive adsorbent in surface chemistry,[66, 67] heterogeneous catalysis,[68-73] environmental decontamination,[74] as a chemically inactive filament in superconducting composites,[75, 76] coating for solar cells efficiency improvement,[77] high electron mobility transistors passivator[78] and a heat-conducting stiff component in nanodevices.[79] Although thin MgO films (thickness up to 25 Å) may be able to conduct electrical current,[80] bulk oxide is a pronounced non-conductor (bandgap 7.8 eV, dielectric constant $\varepsilon_r \approx 10$), what limits the utilisation in chemical sensing, but opens wide possibilities to use it for insulation applications.[81]

It is known that surface morphology of MgO plays an important role in many processes. Decrease of the particles size results not only in development of the specific surface area, but also in a larger concentration of lattice imperfections on the surface, like edges of steps, corners, kinks or divacancies. These defects act as active centres and can improve chemisorption and reactivity of the oxide towards adsorbed species. Nanoscale MgO structures with increased surface area often require low preparation temperatures (commonly up to 500 °C [82, 83]) because calcination at a high temperature will increase the size of MgO crystallites or initiate their assembly into micrometer-scale agglomerates.[83] It must be also noted that some important properties of MgO are sensitive to the presence of contamination,

which varies by thermal decomposition of different generally accepted precursors (magnesium hydroxide, oxalate or carbonate). For example, the catalysis of alcohol dehydrogenation is only observed when MgO is contaminated with CO_2 from an incompletely decomposed precursor.[68] Such catalytic destructive processes do not take place over carbon-based adsorbents with inactive nonpolar surface.[84]

One-dimensional nanostructures composed of MgO, i.e. rods, tubes, whiskers, are promising for many technological applications, primarily nanoscale electronic and optical devices,[85] as well as in heterogeneous catalysis due to the increased surface-to-volume ratio. There is a big variety of methods for producing one-dimensional MgO structures described in literature sources. Single-crystal nanorods, nanotubes (including polycrystalline), and nanobelts have been made by means of rod-like $Mg(OH)_2$ crystals conversion,[86] chemical vapour deposition,[87] solution based approach,[88] vapour-liquid-solid[89, 90] and vapour-solid[75, 91] methods, pulsed laser deposition,[92] decomposition of powder precursors,[76, 93] and a solid-gas reaction using ZnO rods as nanotube templates.[94] However, such convenient and flexible method for adjusting geometric parameters as replication of the cylindrical pores in conventional hard templates like porous anodic alumina or track-etch polycarbonate membranes has not been reported yet. The major assumed drawback to the use of porous alumina templates is that the interfacial reaction between crystalline MgO and amorphous Al_2O_3 may lead to the formation of $MgAl_2O_4$ spinel structure at relatively low temperature, which is needed for the conversion of the precursor.[95]

3.3.3 Indium oxide

Indium oxide (In_2O_3) is one of the most extensively studied metal oxide materials, especially for its gas sensing properties. Since In_2O_3 is an *n*-type semiconductor, its conductivity depends on the composition of the ambient atmosphere. The chemisorption of gas molecules results in surface charging that modifies the potential energy distribution (the energy bands are bending) and, by that, the effective carrier concentration near the surface. For example, the effect of oxygen ionosorption creates a negative charge at the surface and an increase in the band bending and work function. For an *n*-type semiconductor this results in the creation of a depletion layer and a decrease in surface conductance.[96-98] Accordingly, these effects have

been used for sensing purposes. The response of In_2O_3 towards numerous gases was investigated,[99] such as ozone,[100-102] nitrogen dioxide,[103, 104] hydrogen,[101, 105, 106] carbon monoxide,[105, 106] methane[107, 108] and hydrogen sulphide,[109, 110] The performance of the metal-oxide-based sensors depends strongly on particle size and microstructure of an oxide material.

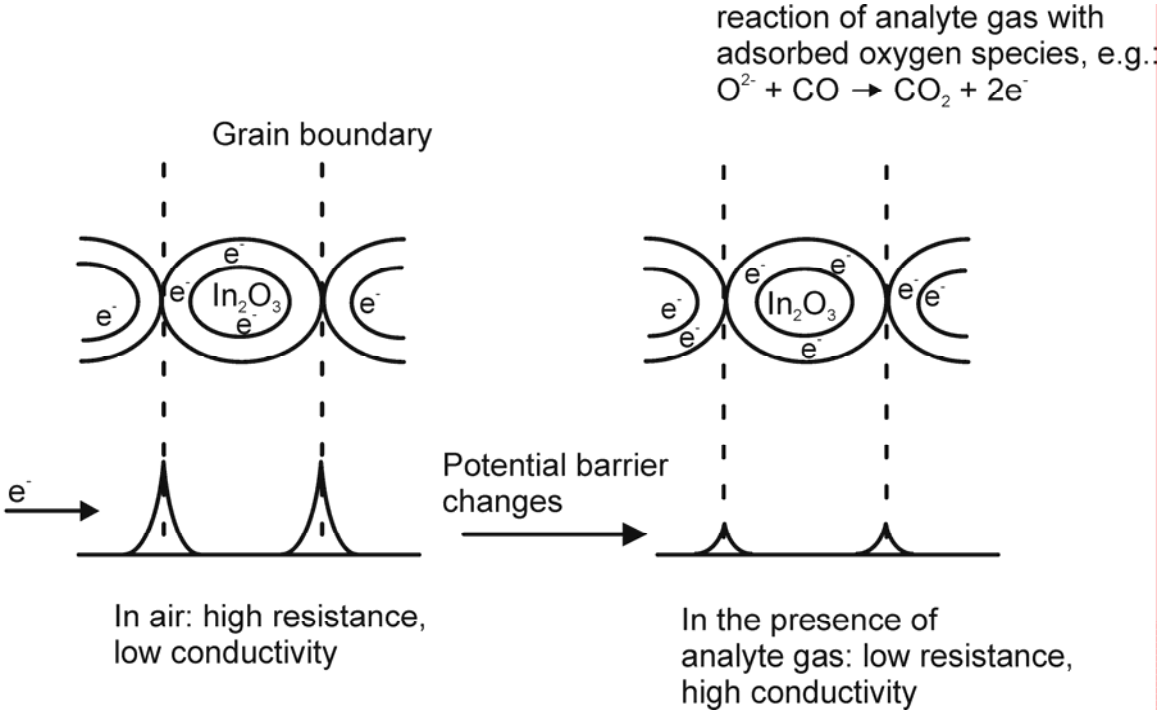

Figure 7. Sensing mechanism of a polycrystalline *n*-type gas sensor (modified from [111]): reaction of analyte gas with adsorbed oxygen species increases the number of charge carriers.

The general aim is to ensure a sufficiently large contact area between the oxide surface and the gaseous analyte. Mostly two strategies are applied to achieve this condition.

On one hand mesoporous materials[107, 108, 112] were used, which is a traditional route to ensure a high surface to volume ratio of ceramics.[113] Ordered mesoporous In_2O_3 materials were synthesized by structure replication from hexagonal mesoporous SBA-15 silica and cubic KIT-6 silica[107, 108] and solvothermal self-assembly reaction using surfactants such as sodium dodecyl sulphate or lysine.[112]

On the other side quasi one dimensional (Q1D) structures like nanorods, nanowires, or, especially, nanotubes are also of interest, as the aspect ratio intrinsically provides

a larger accessible surface area.[3, 114-116] Q1D In_2O_3 nanostructures, such as solid rods or wires, are available by a number of methods, e.g. vapor deposition techniques,[117, 118] annealing of In films with sputtered Au catalyst,[119] sol-gel technique,[120] thermal treatment of In salts within porous silica[121] or salts or $In(OH)_3$ within porous alumina.[122, 123]

The two above-mentioned strategies might also be applied at the same time. Porous Q1D nanostructures (i.e. composed of sintered smaller nanoparticles with the presence of micro- and mesopores in-between) obviously possess a larger surface and accordingly should have a better potential in fields of catalysis and gas sensors.[124, 125]

Hollow In_2O_3 nanotubes have been formed by CVD, but have the disadvantage of the presence of incorporated Au-catalyst particles, which are essential for this technique.[126, 127] Other attempts employed porous alumina membranes as templates. Filling of the pores with a suitable precursor could be achieved from the gas phase[128] or from solution by infiltration with a sol.[129] Also the electrolytic deposition of indium metal in alumina membranes and subsequent conversion to indium oxide nanowires was described.[130]

In all of these cases, the major drawback to the use of porous alumina is the difficulty to remove the templates selectively without destroying the nanostructured indium oxide. This is usually achieved by etching in concentrated akali metal hydroxide solutions. Residues of the membrane are always found, under mild etching conditions.[129]

3.3.4 Undoped and Mn-doped ZnO

Plain and doped ZnO nanostructures are a promising material for various electronic and optoelectronic devices.[131, 132] In particular, Mn-doped ZnO can be used in spintronics because of ferromagnetic behaviour at room temperature.[133] However, it is often discussed in the literature that not all of the synthesised ZnO:Mn samples exhibit ferromagnetic properties. The experimental data suggests that the ferromagnetism of this material substantially depends on its preparation procedure.[134] This concerns the processes, which induce repelling of impurities from nanoparticles and phase separation, e.g. reactions at elevated temperatures. This

phase separation is especially visible in cases with Mn-doping because of the tendency of manganese-related phases towards clustering.

Main efforts in fabrication of ZnO and doped ZnO:Mn nanomaterials have been made in obtaining of quasi one-dimensional (Q1D) structures like nanorods, nanowires or nanotubes, which is most often performed by vapour phase methods. For instance, aligned ZnO nanotube arrays are accessible by porous alumina assisted CVD process at 500 °C.[135] ZnO:Mn systems were also synthesised by CVD-process (600°C, 50 torr), however an uncertain doping concentration below 1.0% was reported.[136]

Besides high-temperature vapour phase synthesis, a lot of attention has been paid to low-themperature methods of ZnO and ZnO:Mn Q1D materials formation. Plain ZnO nanowires were reported by microwave assisted aqueous synthesis at 120 °C,[137] irregular disordered ZnO nanorods were fabricated by solvothermal methods in the temperature range 80-120 °C.[138, 139] ZnO:Mn systems have been made by surfactant-assisted assembly with subsequent reaction at 280-310°C, and a solvent assisted route at 250°C (electron microscopy revealed irregular elongated nanoparticles).[140] Mn-doped ZnO nanorods were made by thermal diffusion at 95 °C,[141] or by solution-based doping into ZnO nanorods (95 nm long).[142]

ZnO nanotubules and nanorods have also been formed by sol-gel method in porous alumina templates followed by annealing of gels at 500°C[143] or 650 °C[144] in air. Synthesis of mesoporous ZnO wires has also been reported by precipitation in alumina membranes as templates.[145] The obvious disadvantage of porous alumina templates is that both alumina and ZnO are amphoteric oxides and the selective etching of templates (usually in concentrated alkaline solutions) is difficult, since alumite films and ZnO nanostructures are dissolved under the same pH conditions.[146, 147] However, sol-gel technique allows to vary the concentration of a doping agent more precisely than in a CVD-process or in a solid-state reaction. This method is usually based on coprecipitation from aqueous nitrate or chloride solutions by means of pH-decrease with basic agents and the annealing product may contain irrelevant components.

3.3.5 Cu-doped ZnO

There is currently growing interest in studying Cu-doped ZnO systems, which belong to the class of diluted magnetic semiconductors (DMS)[148, 149] and are considered as a key materials for spintronic devices.[150] Magnetism in ZnO:Cu seems to be an acquired property and can not be reduced to a combination of impurities characteristics, since no Zn- or Cu-related phases found in the doped zinc oxide are magnetic by themselves. Cu^{2+} is also considered by many researchers as a possible dopant for achieving of p-type ZnO.[151, 152] Isovalent impurities do not change concentrations of electrons and holes in semiconductors directly, but they can alter the band-gap energy, which, in its turn, affects the concentration of free charge carriers.

Many issues about ZnO:Cu systems still remain open. For instance, the data about the state of copper in ZnO:Cu from different literature sources is very controversial. It seems to be highly dependent on the doping concentration and, particularly, on synthesis routes, which may differ for nanoscale materials with various morphologies, e.g. thin films,[153, 154] powders,[155] nanoparticles[156] and nanorods or nanowires.[141, 157]

Cu^{+} is the most obvious oxidation state found in the literature,[149] but Cu^{2+} and Cu^{0} are also found very often in varying proportions.[158] Formation of substitutional solid solutions with Cu^{2+} ions in Zn^{2+} normal lattice points is mostly desirable for tailoring of semiconducting properties, but the solubility of Cu^{2+} in ZnO matrix is rather restricted because ZnO and CuO do not meet the necessary conditions for unlimited solubility completely: Zn and Cu have a small atomic radii difference and similar configurations of outer electron shells, but different crystal structures of the corresponding oxides (for ZnO it is derived from hexagonal close arrangement, and for CuO it is monoclinic structure). Maximal reported achieved concentrations normally do not exceed 10%,[159] a concentration up to 16% was reached taking into account Cu^{0} clusters inclusion as well.[160]

Quasi one-dimensional (Q1D) ZnO:Cu nanostructures, such as nanorods or nanowires, are particularly interesting as eventual building blocks for spintronic nanodevices. The high specific surface area of these structures opens up the possibility of effective chemical functionalisation of the surface and altering of the material properties in this way.

The most intensively studied approach to the synthesis of Cu-doped ZnO nanowires is the vapor deposition technique[161, 162] because it is also widely used for the formation of plain ZnO nanorods. However, in this method, the dopant concentration depends on sublimation and transport processes and has an accidental character to a greater or lesser extent.[163, 164] Along with vapor phase methods, thermal diffusion[141] or template-based synthesis[165] have been applied. The thermal diffusion yields only anisometric particles with small aspect ratios. For the template-based method, porous anodic alumina membranes have been employed. The disadvantage of this approach is the contamination of the material with alumina. Some analysis procedures showed characteristics, which are intrinsic to Al^{3+} impurities.[165]

4 Results and Discussion

In this section, the characterisation of routinely produced PAOX templates with SEM, XRD, BET surface analysis, and TGA is given. This preliminary investigation gives information about the available pore sizes, and helps to gain a better understanding of possible chemical interactions between the pore walls and a precursor. Some aspects of chemical etching and thermal treatment of PAOX templates from different electrolyte solutions are discussed.

4.1 Characterisation of Porous Anodic Aluminium Oxide (PAOX) Films

4.1.1 Variation of PAOX Geometric Parameters

The pore diameter of PAOX films obtained from 0.3 M oxalic acid solution (estimated from SEM micrographs, Fig. 8) was 41±3 nm and showed a good correlation with BET-measurements (pore size 41.75 nm; surface area 156.7 $m^2 \cdot g^{-1}$ after dehydration of the samples at 700 °C).

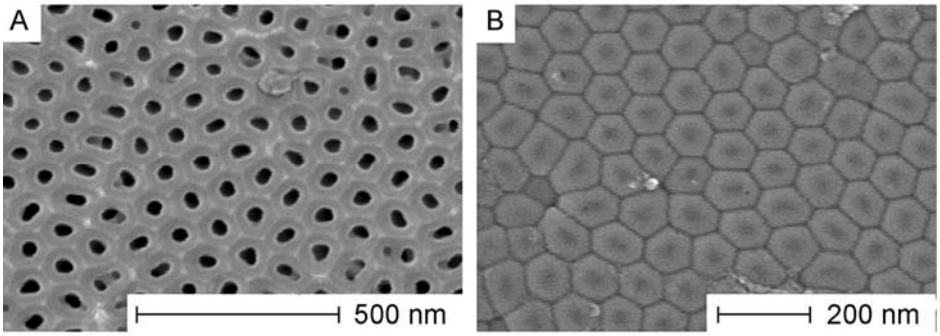

Figure 8. SEM micrographs of porous (A) and barrier (B) layer of PAOX, obtained from 0.3 M oxalic acid solution at 40 V anodization voltage (pore size 41 nm).

The thickness of the membranes depends on anodization time (typically 17-19 hours in the present work) and was around 60-70 μm.

PAOX templates from 10 wt % H_2SO_4 aqueous solutions at 20 V anodization potential, from 0.3 M H_2SO_4 at 27 V, and from 0.3 M $H_2C_2O_4$ solution at 60 V possess identical morphology, as obtained at 40 V, but different pore diameters (see Tab. 5 for details). The sample from 0.3 M $H_2C_2O_4$ solution at 60 V has no hexagonal ordering of the pores, as well as a large spread in pore size values.

4.1.2 Removal of Barrier Layer from PAOX by Wet Etching Method

At the stage of barrier layer removal either in orthophosphoric acid or in a mixture with potassium dichromate (by simply immersing of a membrane into the aqueous solution), the pores become widened and their diameter increases to approximately 75-80 nm. The compact barrier oxide layer dissolves slower than the porous layer, which can lead to the complete inter-pore walls dissolution even before all the channels are open through.[166] This pore widening effect makes the reproducible removal of the barrier layer and opening of a reasonable number of nanochannels from both sides for the subsequent capillary driven infiltration difficult. The examples compared in SEM-images in Fig. 9 are meant to illustrate the poor quality of the results. The majority of the pores are still blocked even under optimal experimental conditions. The following increase of the etching time at a given temperature will result in a larger degree of barrier layer dissolution, but still far from complete before the porous layer becomes unusable.

To solve the problem, the method of a protective layer was employed. If the porous PAOX layer is isolated (in our case - firmly pressed to a flat teflon) so that only barrier layer stays in contact with the etchant, it helps to strip the barrier layer off selectively without critical destruction of the nanochannels (Fig. 10). The front side of the pores, nevertheless, increased to approximately 52 - 55 nm. One difference is apparent between the examples in Fig. 9 and Fig. 10: in the latter case all the pores are unblocked completely without critical inter-pore walls destroying. The method provides reproducible results, and the etching time can be noted less accurately than in a conventional procedure. Another advantage of this innovative approach in comparison with the methods described elsewhere (e.g., a protective layer made of a mixture of nitrocellulose and polyester resin in ethyl acetate, butyl acetate and heptane,[167] or the use of nail polish[168]) is that it leaves no organic residues on highly sorptive surface of PAOX after the protective layer removal.

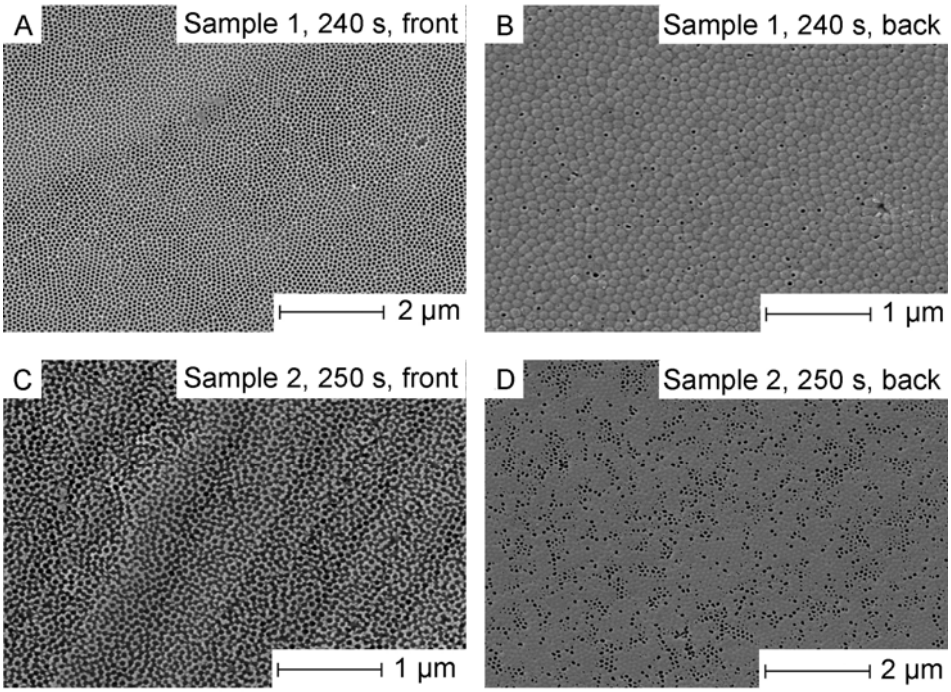

Figure 9. PAOX membranes etched for 240 s (A, B) and 250 s (C, D) in $H_3PO_4/K_2Cr_2O_7$ solution at 52 °C. Despite large pore walls destruction, only a minority of the pores is open.

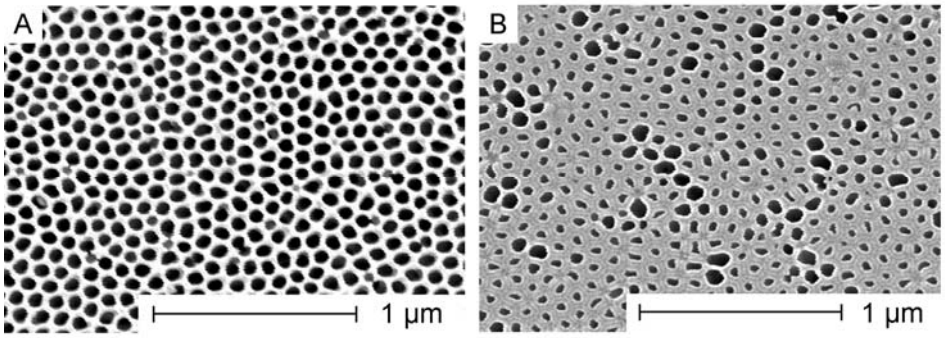

Figure 10. PAOX membranes etched with a protective teflon for approximately 6 minutes. The complete absence of the barrier layer (B) is evident (A – front side, B - backside).

Table 2 summarizes the data about pore diameters of the PAOX membranes before and after the wet etching step. The time of the treatment in the etching solution (not shown) was individual for each sample.

Table 2 Pore diameters of the self-made PAOX templates (from SEM images)

Electrolyte	Voltage [V]	Average pore diameter [nm]	Pore diameter after wet etching [nm]	
			Without porous layer protection	With a protective layer (teflon)
10 wt % H_2SO_4	20	23	-	26-28
0.3 M H_2SO_4	27	30	-	30-33
0.3 M $H_2C_2O_4$	40	41	75-80	52-55
0.3 M $H_2C_2O_4$	60	70	-	ca. 110

4.1.3 Structural and Composition Changes in PAOX during Thermal Cure

4.1.3.1 Thermogravimetric analysis of oxalic PAOX before and after wet etching

TG curves of an unetched oxalic PAOX membrane and a membrane after the barrier layer removal are presented in Fig. 11. In both cases, the weight loss between the ambient temperature and 400 °C is attributed to dehydration process, involving absorbed and coordinated water. A moderate weight loss between 400 and approximately 800 °C is due to a dehydroxylation process.

A steep mass loss event above 800 °C is attributed to the thermal decomposition of anion impurities (oxalate groups) accompanied by release of CO_2. This behaviour distinguishes both sulphuric and oxalic PAOX templates with tailored smaller pore diameters from commercial membranes (pore diameter around 200 nm) obtained from phosphoric acid solutions.[169] The former are known to show a similar multi-step weight-loss process up to 1000 °C, but with quantitative differences, and the latter are thermally stable and show no mass loss above 400 °C. The release of gaseous products (CO_2 and SO_2) can be a serious difficulty in obtaining of Q1D-structures of a desired chemical composition, when switching from commercial phosphoric templates to self-made.

Thermogravimetric analysis of self-made PAOX membranes obtained from oxalic acid solution suggests that the amount of anion impurities is reduced after the wet etching step. The comparison of the TG curves reveals a mass loss event due to the oxalate anion decomposition between 880 - 980 °C for both the unetched and etched membranes, but the quantitative characteristics are clearly different.

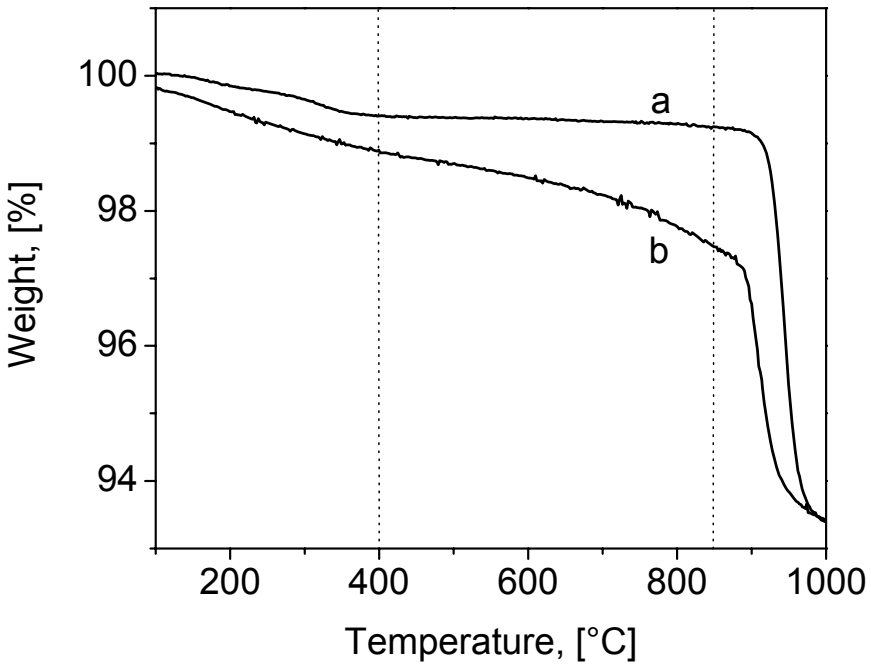

Figure 11. TG traces of an unetched oxalic PAOX membrane (a) and the same PAOX membrane after the barrier layer removal in the etching mixture (b). The weight loss due to the decomposition of oxalate anions constitutes 5.7 and 4 % respectively.

Still, the etched templates show a more significant weight loss due to the dehydration and dehydroxilation, which points to the conclusion that they are covered with more surface OH-groups and sorb moisture more readily than unetched species.

The reasonable explanation of this difference in electrolyte impurities content is based on concept that the cell in porous PAOX consists of two regions: the outer region, which is composed of relatively pure alumina, and the rich anion contaminated inner region directly at the interior of a pore (Fig. 12).[170, 171] The amount of oxalate anion impurities is reduced due to the predominant dissolution of the electrolyte-rich inner area of the individual PAOX cells.

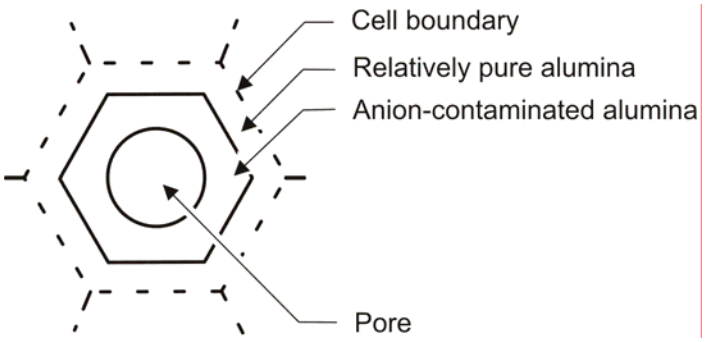

Figure 12. Schematic sketch of the PAOX cell morphology, clarifying the decrease of anion impurities content after the wet etching (Modified from [170]).

As mentioned in the experimental part, the acidic etching mixture is prepared from concentrated H_3PO_4 (59 ml, 85 wt.-%), potassium dichromate ($K_2Cr_2O_7$, 24 g), and diluted with distilled water (filled up to 500 ml). The following reaction obviously takes place between dichromate anions from the etching mixture and oxalate anions from PAOX in the acid medium (small bubbles of released CO_2 are visible in practice during the ething procedure):

$$Cr_2O_7^{2-}(aq) + 14H^+(aq) + 3C_2O_4^{2-}(aq) \rightarrow 2Cr^{3+}(aq) + 7H_2O(l) + 6\ CO_2(g)$$

This reaction is also the reason for decreased oxalate content after barrier layer removal.

4.1.3.2 XRD analysis of oxalic and sulphuric PAOX

Structural characteristics of the initially amorphous templates after the thermal treatment of a precursor within the pores have a critical importance for the following dissolution of alumina, e.g. in concentrated HF, KOH, or H_3PO_4, and the subsequent liberation of the Q1D-structures therefrom.

The typical XRD-patterns of PAOX templates after the pyrolysis conditions, normally applied to pre-ceramic silicon-based polymers involved in further replication experiments (1000°C, 2 h) is shown in Fig. 13, and presents a low crystallinity compound of *γ* and *θ* modifications. To determine the difference in thermal evolution of the PAOX templates made in oxalic and sulfuric acid, two template samples were calcined at 1200°C for 5 hours and then characterized by XRD. It is evident, that the calcination of oxalic membranes results in high-crystalline corundum, whereas sulfuric membranes transformed into γ-Al_2O_3.

Table 3 outlines the results of XRD examination of PAOX templates.

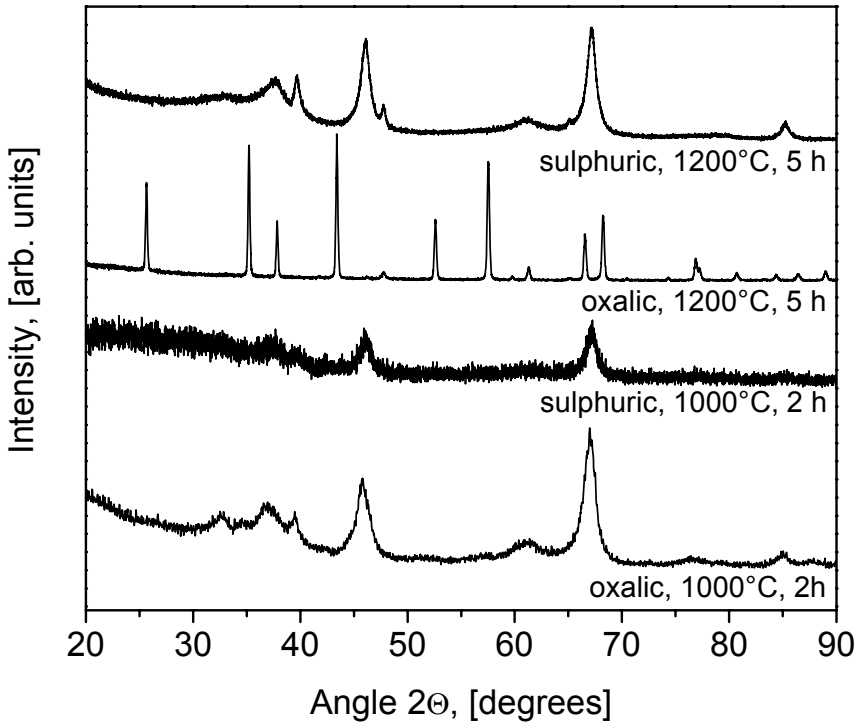

Figure 13. XRD patterns of thermally cured PAOX templates from different electrolytes.

Tab. 3 Summary of Al_2O_3 modifications in PAOX templates calcined at different temperatures.

Type of the alumina (according to the electrolyte)	Temperature of treatment [°C]	Alumina phase composition (from XRD)
sulfuric	1000 °C	$\gamma + \theta$
	1200 °C	γ
oxalic	1000 °C	$\gamma + \theta$
	1200 °C	α

4.1.4 Anodic oxidation of aluminium under pulse current conditions

One of the issues in nanocomposite production is the fabrication of Q1D nanostructures with alternating diameter. For instance, dumbbell-shaped nanochannels in PAOX templates were reported for the subsequent nanocasting formation of reinforcing carbon fibers,[172] which are supposed to have an enhanced mechanical interlocking with the composite matrix.

In the present experiment, pulse current anodization of aluminium, where the voltage changed in 0-20 V diapason with variable frequencies (1 Hz – 1 MHz, practically achieved in the laboratory with a TOELLNER TOE 7711 functional generator), was performed with the expectation of a 'beads-shaped' nanochannel morphology with variable periods. An unexpected effect has been observed instead.

Fig. 14 schematically demonstrates the voltage-time curve of the experiment, and SEM images of the surface of resulting PAOX membranes, obtained at different frequencies.

The material combined a small pore size (about 10 nm), characteristic for the average potential value (10 V, the linear dependence of the pore size from the voltage is assumed), and a pore ordering typical for optimal 20 V conditions. It is seen from the illustration that the best pore ordering is at 1 Hz frequency, and is getting worse as the frequency increases. On the basis of this observation, it would be also interesting to investigate the frequencies between 0 and 1 Hz, as it may lead to the perfect hexagonal pore arrangement, keeping the pore size near to 10 nm, which is not achievable under constant potential conditions.

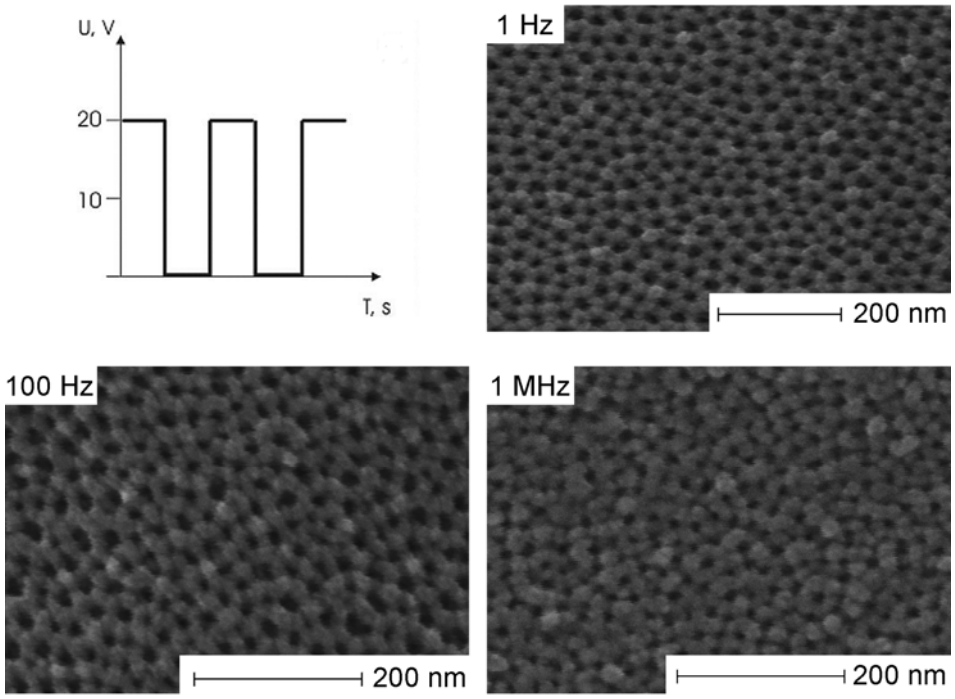

Figure 14. Pulsed anodization of aluminium foils.

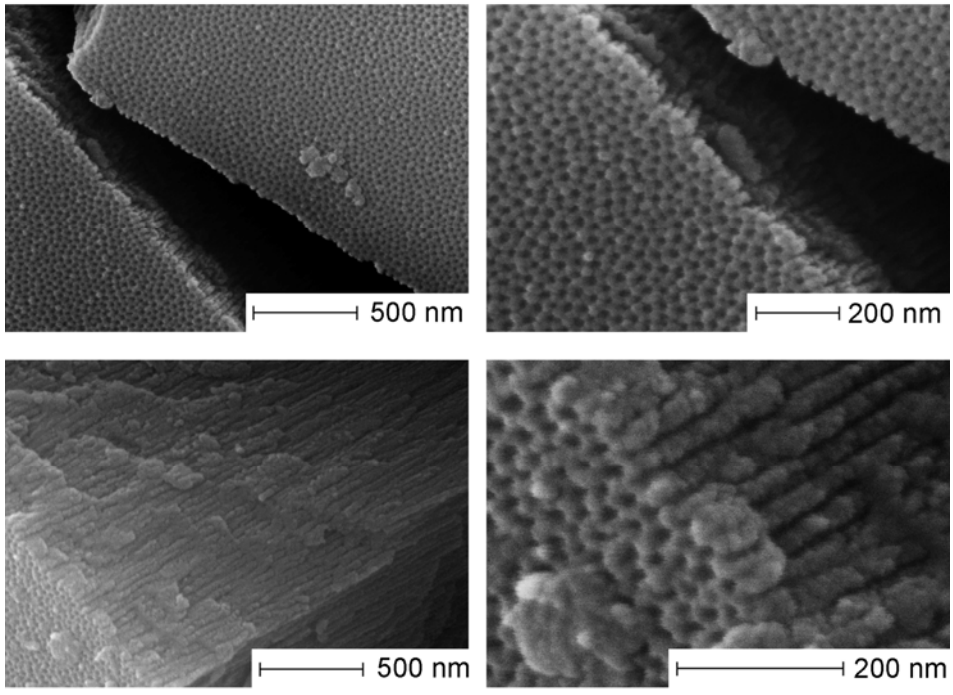

Figure 15. High resolution SEM images, demonstrating the morphology of nanochannels, obtained at 1 Hz and 20 V pulsed anodization.

However, the desired 'beads-shaped' morphology of the nanochannels in PAOX was not reached. Fig. 15 presents detailed SEM images of the broken edges of a

membrane made at the frequency of 1 Hz. As far as the resolution of the scanning microscope allows seeing it, the nanochannels are not perfectly uniform, but straight and without any obvious evidences of a 'beads-shaped' structure.

All in all, this experiment showed that pulse current oxidation of aluminium at frequencies between 1 Hz and 1 MHz do not lead to a morphology with a non-uniform pore thickness, but opens up new possibilities to make PAOX templates combining the ordered pore organisation, produced only at a number of known discrete constant voltages, but a smaller pore size (approximately by a factor of 2). The 10 nm size of the nanochannels opens up the possibility in the future to synthesize nanowires, in which the quantum confinement effect can be very likely observed.

4.2 Polymer-Derived SiOC Nanotubes and Nanorods

In this section, the detailed study of template assisted formation of aligned ceramic nanowires starting from commercially available silicon-based polymers (KiON Ceraset and Starfire Systems SP Matrix) is discussed. The template-based synthesis was carried out in PAOX membranes with pore diameters of 23-26 and 52-70 nm.

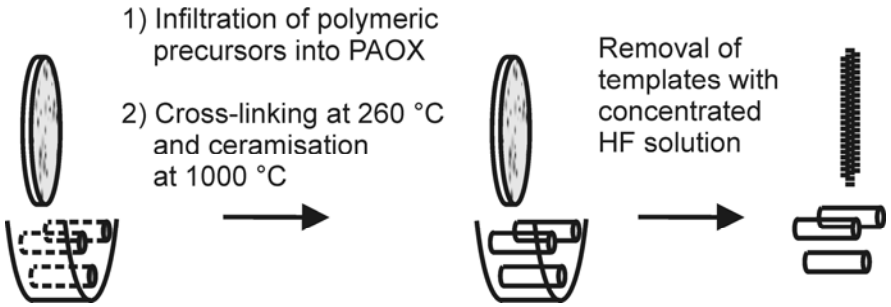

4.2.1 Ceramic Nanowires Derived from 40 V PAOX Templates

4.2.1.1 Microscopic study of polymer-derived SiOC nanowires

The diameter of the KiON Ceraset-derived ceramic wires after dissolution of the PAOX template was about 70 nm (see Figures 16 (SEM) and 17 (TEM)), which is

approximately 20% smaller, than the nominal pore diameter of the templates used for this series of experiments.

This decrease in volume obviously results from polymer shrinkage during the thermal processing step. The length of the wires was about 45 µm after dissolving the template with a concentrated $H_3PO_4/K_2Cr_2O_7$ solution, but only 13 µm after treatment with HF. This observation suggests that concentrated hydrofluoric acid destroys the resulting Q1D-ceramic wires formed during the ceramisation process.

In this context it is also important to note, that silicon nitride is etchable at room temperature in concentrated or buffered HF and in a boiling H_3PO_4 solution.[173]

This behaviour would certainly affect a possible product formed via pyrolysis of the nitrogen-containing organosilicon polymer. Indeed and according to the Energy Dispersive X-ray analysis (EDX) data, no presence of nitrogen could be detected in the resulting material.

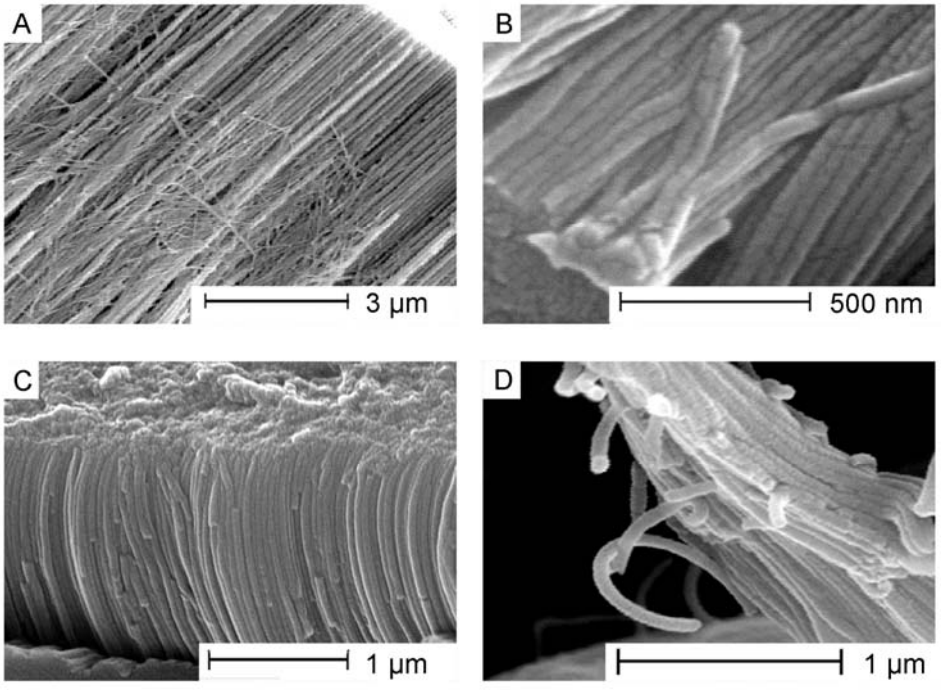

Figure 16. SEM micrograph alongside the template pores after infiltration and pyrolysis step, but before dissolution of the template (A). Resulting KiON Ceraset-derived wires (B, C, D) after dissolution of the template.

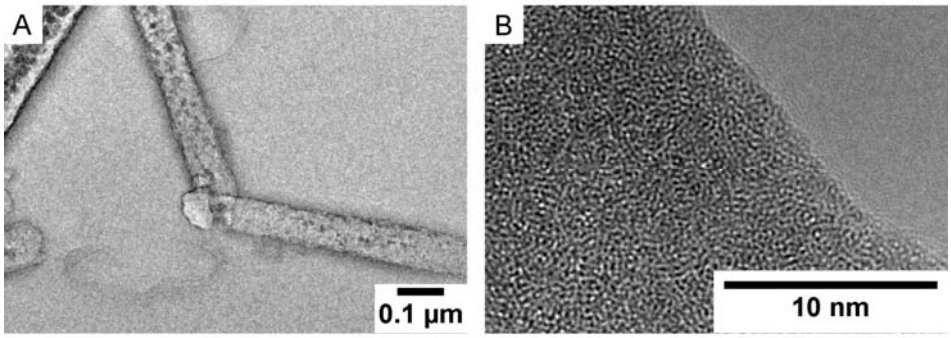

Figure 17. TEM micrographs of KION Ceraset-derived nanowires. The high resolution TEM micrograph B shows the amorphous nature of the wire composition.

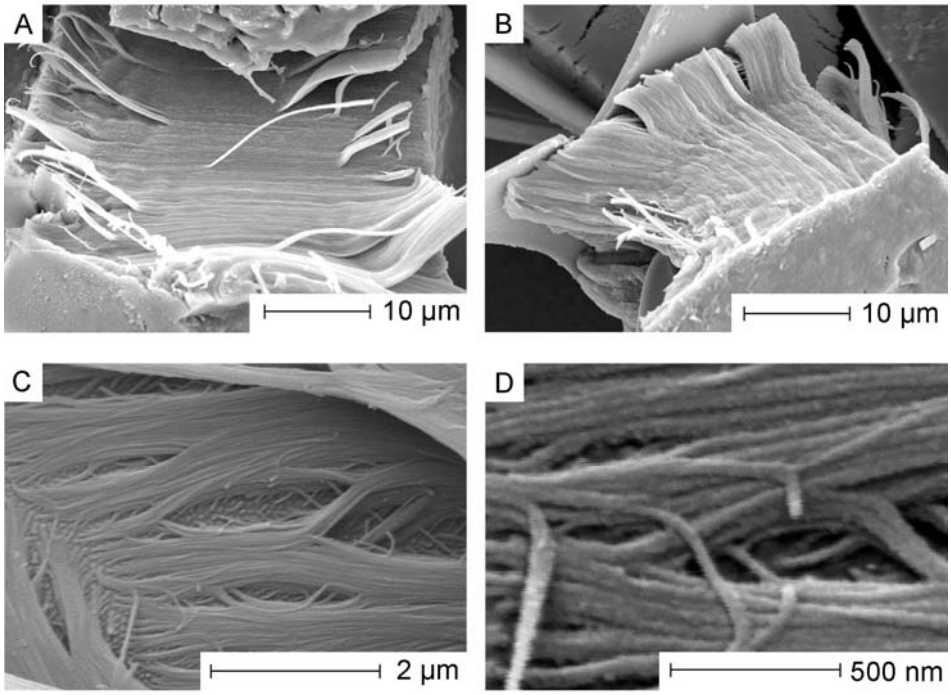

Figure 18. SEM micrographs (A, B) and close-up SEM micrographs (C, D) of the SP matrix polymer-derived wires after dissolution of the template.

The resulting dimensions of the SP Matrix polymer-derived wires can be estimated from the SEM micrographs (Figures 18 and 19) to be 25–40 µm (etched in HF). They exhibit a wire diameter of about 43 nm, which is also smaller than the pore diameter of the templates used for these experiments (52-55 nm).

Attempts to obtain TEM micrographs of the ceramic wires obtained from the SP matrix polymer were hampered due to the structure of the rods. Sample preparation by dispersing the nanorods under vigorous stirring in ethanol or ultrasonic agitation in

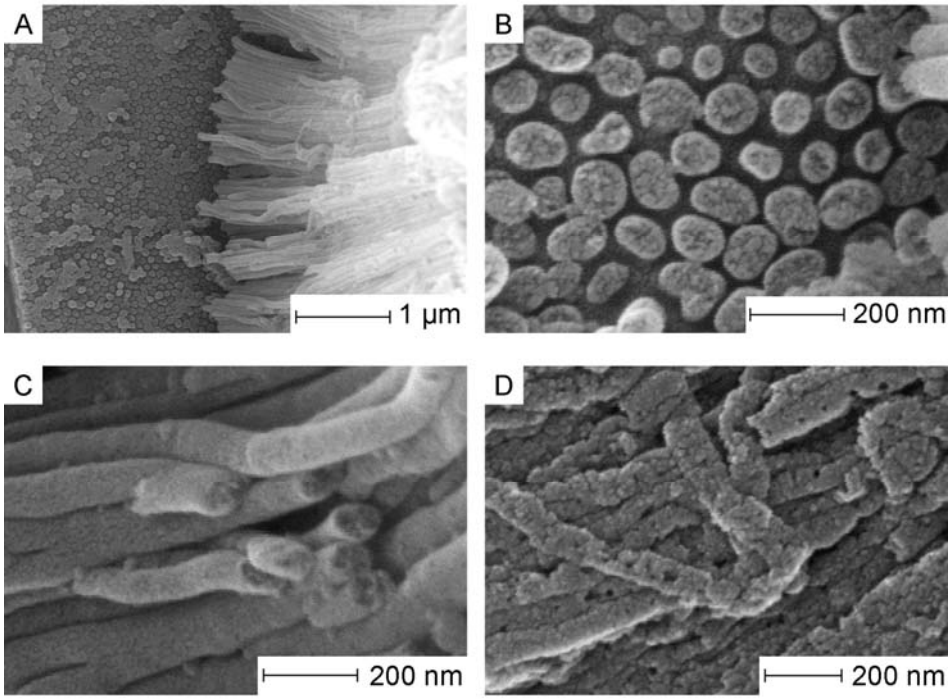

Figure 19. SEM micrographs (A-D) with close up views of the nanorods of the SP matrix polymer-derived wires after dissolution of the template. (A) aligned rods together with rod stubs [left side of (A)] from which the rods have been broken off. (B) Rod stubs and outer rod surface with higher magnification (C) showing the particulate nature of the rods. (D) particulate nature of the rods with higher magnification.

different solvents often destroys the rods completely. This finding was attributed to the particulate nature of the nanorods being composed of particle agglomerates rather than having a compact homogeneous structure as can be seen from Figure 20.

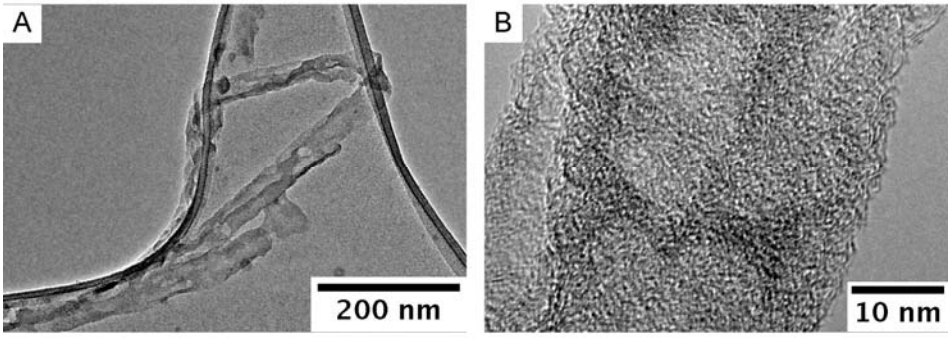

Figure 20. TEM micrographs of isolated nanorods of the SP matrix polymer at different magnifications obtained by ultrasonification of a suspension of calcined ceramic material after dissolution of the alumina template.

The good wetability of the pore walls of the PAOX templates could be predicted from earlier studies on nanotubes prepared from polycarbosilanes. If adhesion between the pore walls and the filling material is very strong, or the solidification of the preceramic precursor starts at the interface pore wall/precursor and proceeds to the inside of the pores, the formation of hollow nanotubes is preferred over formation of solid rod like material when taking a massive shrinkage of the material due to the ceramication process into account.[1]

4.2.1.2 FTIR study of SiOC nanowires derived from two commercial polymers

To follow the chemical changes during the formation of the polymer-derived nanomaterials, their composition was studied by means of FTIR spectroscopy. The infrared spectra of (i) the liquid KiON Ceraset polyureasilazane precursor, (ii) the polymer cured within the PAOX template at 700 °C (the temperature below the transition of the bulk cross-linked product into ceramic components) and (iii) cured within the template at 1000 °C are compared in Figure 21.

The intense band at 3450–3200 cm^{-1} in the liquid polymer spectra can be attributed to N–H stretching vibrations. The signal at 3045 cm^{-1} corresponds to C–H stretching vibrations of the vinyl groups, methyl and methylene vibrations are presented at 2965 cm^{-1} (CH_3 asymmetric, 2975–2950 cm^{-1}), 2920 cm^{-1} (CH_2 asymmetric, 2940–2915 cm^{-1}) and 2850 cm^{-1} (CH_2 symmetrical, visible only at high resolution around 2870 cm^{-1}). The broad intense band at 2127 cm^{-1} is characteristic of Si–H (2140 cm^{-1}). The strong band at 1260 cm^{-1} corresponds to the absorption of Si–CH_3 (1280–1255 cm^{-1}) and is assisted by the deformation vibration at 760–790 cm^{-1}. Possibly Si–N vibrations are presented at 1170–1175 cm^{-1} and around 900 cm^{-1} which are, however, significantly weakened at the higher curing temperature of 1000 °C compared to 700 °C. The appearance of the spectra of the KiON Ceraset polyureasilazane polymer precursor (Figure 21) cured within the PAOX template at 700 °C shows significant similarities with the appearance of the spectrum of bulk ceramic samples obtained from the precursor under no confinement conditions in the characteristic fingerprint region (temperature range 450–600 °C).[174]

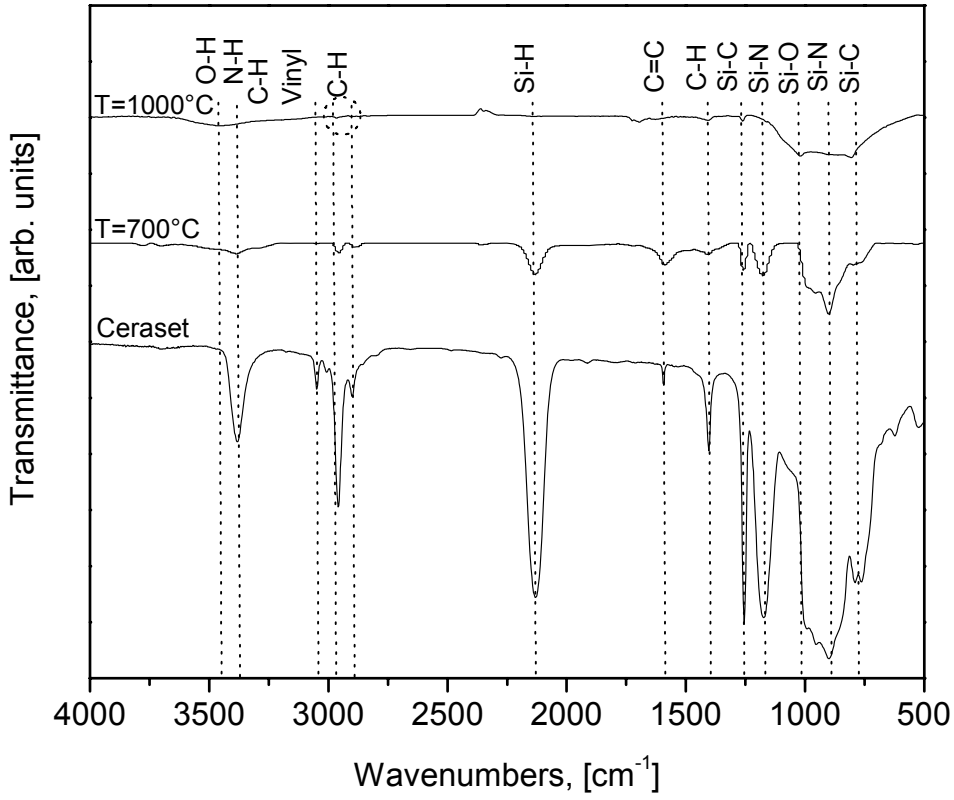

Figure 21. FTIR spectra of the KiON Ceraset polyureasilazane (ceramic polmer pecursor) as received (below), and cured within the PAOX template at 700 °C (middle) and at 1000 °C (above) together with reasonable band assignment.

The broad but intense absorption at 3700–3100 cm^{-1} with the maximal absorption at 3450–3440 cm^{-1} can be attributed to an O–H (3650–3200 cm^{-1}) stretch. However, in-plane deformation absorption of the hydroxyl at 1450–1250 cm^{-1} and 750–650 cm^{-1} is either absent or too weak to be considered as significant. The intensity of vibrations in the C–H region is low possibly due to the vinyl cross-linking. The appearance of a free carbon phase could be confirmed in the spectra at that temperature. The band envelope at 1650–1580 cm^{-1} can be assigned to the stretching mode of the conjugated C=C framework of graphite. Furthermore, the aromatic C_{sp2} stretching vibrations are present at 1630 cm^{-1}.

Ceramic material synthesized at 1000 °C in not dehydrated PAOX templates showed two additional intense bands at 1100 and 1030 cm^{-1}, which are characteristic of Si–O–Si (1125–1010 cm^{-1}) and Si–O–R (1100–1000 cm^{-1}) bending modes, respectively (Fig. 22).[175]

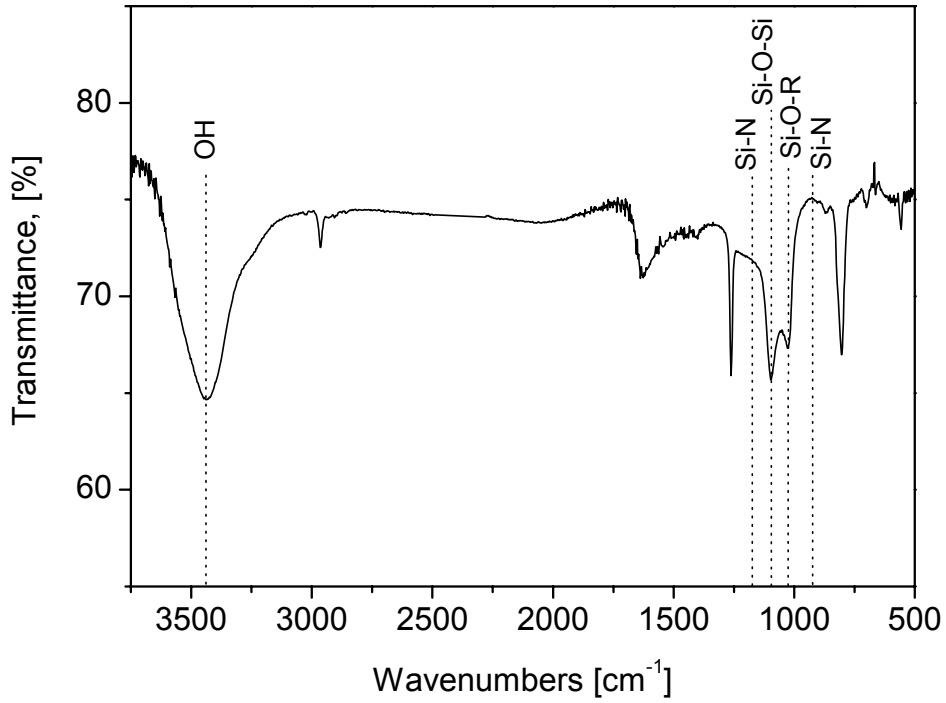

Figure 22. FTIR spectrum of KiON Ceraset derived nanowires from a not dehydrated PAOX template at 1000 °C. Intense bands corresponding to Si-O-Si, Si-O-R, and OH groups and absence of Si-N vibrations are visible.

This finding can be attributed to a hydrolysis reaction of the KiON Ceraset precursor with adsorbed hydroxy groups still present on the template's pore surface. When the alumina films were thus first calcinated at 700 °C to remove this hydroxy layer, the intensity of those two bands decreased significantly (see Figure 21, middle).

The spectra of the liquid SP Matrix Polymer precursor, of its bulk thermolysis product (at 1000 °C) and of the nanowires derived from the SP Matrix Polymer are depicted in Figure 23. The most intensive bands are: sp^2 C-H stretching vibrations mode around 3070–3080 cm^{-1} and C=C stretching modes at 1630 cm^{-1}, the band system between 2860–2975 cm^{-1} is due to the sp^3 C–H stretching modes, a characteristic absorption Si–H absorption is centred around 2100–2170 cm^{-1}.

Absorptions with maximal intensities at 1360, 1059 and 955 cm^{-1} are present due to the Si–CH_2–Si fragments, the peaks at 255, 865 and 780 cm^{-1} are due to Si–C stretching vibrations of the Si–CH_3 groups. The PAOX template-based nanowire species cured at 1000 °C exhibit a significant absorption around 1700 cm^{-1}.

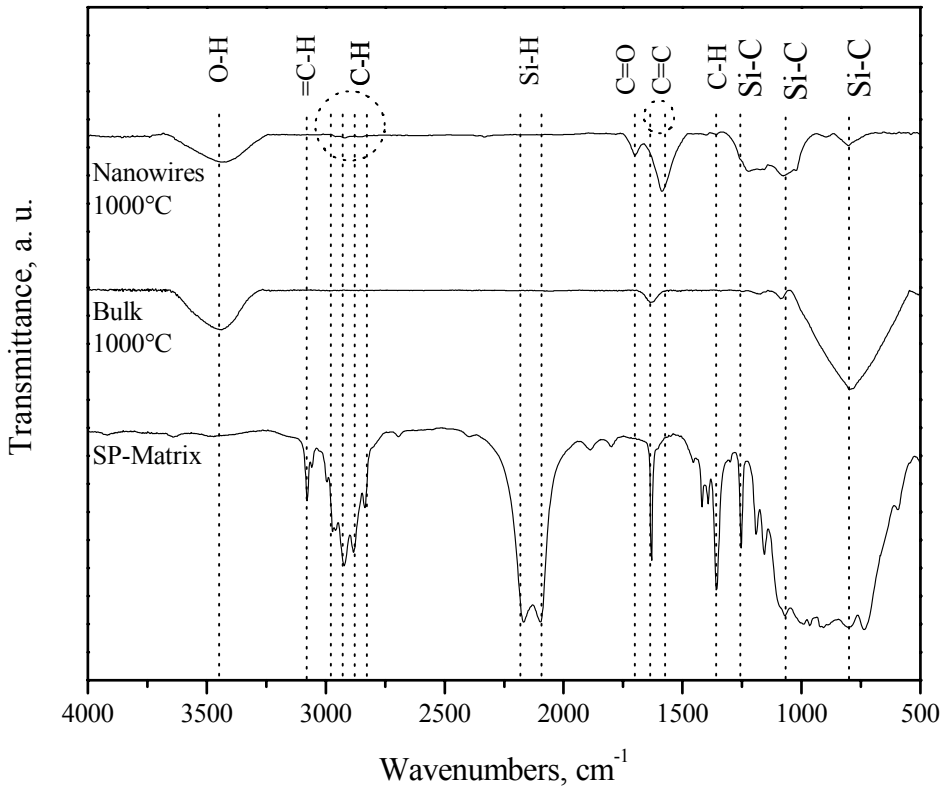

Figure 23. FTIR spectra of the SP matrix polymer as received (below), bulk pyrolysis product at 1000 °C (middle) and cured within the PAOX template at 1000 °C (above) together with reasonable signal assignments.

The appearance of this band might be due to the release of decomposition products derived from oxalate anions which are incorporated into the PAOX template due to the anodic oxidation process which is performed in oxalic acid. The thermal behaviour of PAOX templates derived from sulphuric and oxalic acid solution is clearly different to that obtained from phosphoric acid solution.[169] The thermal analysis displayed a unique mass-loss event around 800–1150 °C for oxalic and sulfuric alumina-derived PAOX templates due to the decomposition of anion impurities (oxalate or sulfate, respectively).

4.2.1.3 Raman spectra of SiOC nanowires

Depending on pyrolysis conditions and a precursor used, the amorphous polymer-derived ceramic material usually contains silicon, carbon and other minor doping atoms in variable nonstoichiometric proportions (excess carbon, see Figure 24), however phonon modes corresponding to SiC at around 800 and 973 cm^{-1} were not observed.

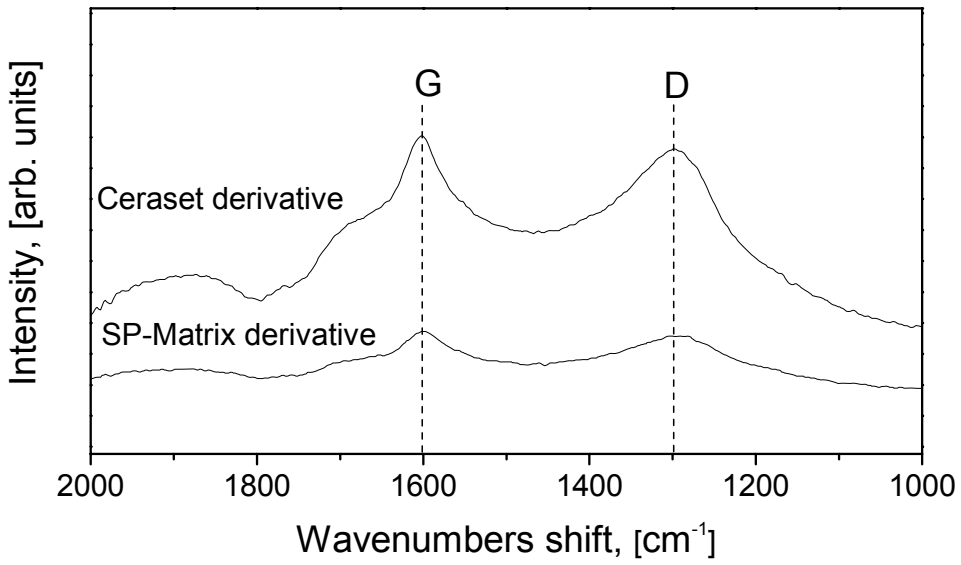

Figure 24. Raman spectra of the KiON Ceraset polyureasilazane derived template-based nanowires (above) and SP matrix polymer derived wires (below).

In entirely amorphous carbon specimens, G and D bands merge into one broad signal with the maximal intensity value around 1500 cm^{-1}. The observation of two separated, however broad phonon bands which correspond to the D and G modes (signals at around 1300 and 1600 cm^{-1}) denote the partial ordering of the carbon phase present in the ceramic into a graphitic layered structure. Comparison of the spectra suggests that the KiON Ceraset polyureasilazane-derived ceramics has a more developed graphite framework than the SP Matrix polymer derivative.

The broad D band resonance at 1290–1300 cm^{-1} results from Raman scattering at the crystallite edges of graphitic structures and is a disorder-induced mode. Its intensity is inversely proportional to the crystallite size of the graphitic structures.[176, 177] The G band signal at 1600 cm^{-1} is caused by the E_{2g} optical mode of ordered

graphite forms.[177] Its appearance is always around 1580 cm^{-1}, and a slight shift toward higher wavenumbers is found only in some samples with extremely small crystallite sizes. The high-energy shoulder of this band normally appears in the presence of disordered phase which are in the focus of the laser beam.

4.2.1.4 X-ray diffraction patterns of SiOC nanowires

The X-ray diffraction experiments fully correspond with the results from Raman spectroscopy. XRD patterns of the nanowires confirmed a difference in phase composition (Figure 25). Both materials are entirely amorphous, but the prominent signals corresponding to the carbon phases are clearly presented in the case of the KiON Ceraset polyureasilazane-derived ceramics whereas they are not seen in the SP Matrix polymer derived product. The growth of the graphite phase in bulk polymer-derived ceramics occurs already at 800 °C, but the size of the domains is normally too small to be detected as a separate phase up to 1100 °C.[178] The phase separation and formation of turbostratic graphite takes place at approximately 1200 °C, whereas formation of nanocrystalline SiC is observed only at temperatures from 1300 °C onwards.

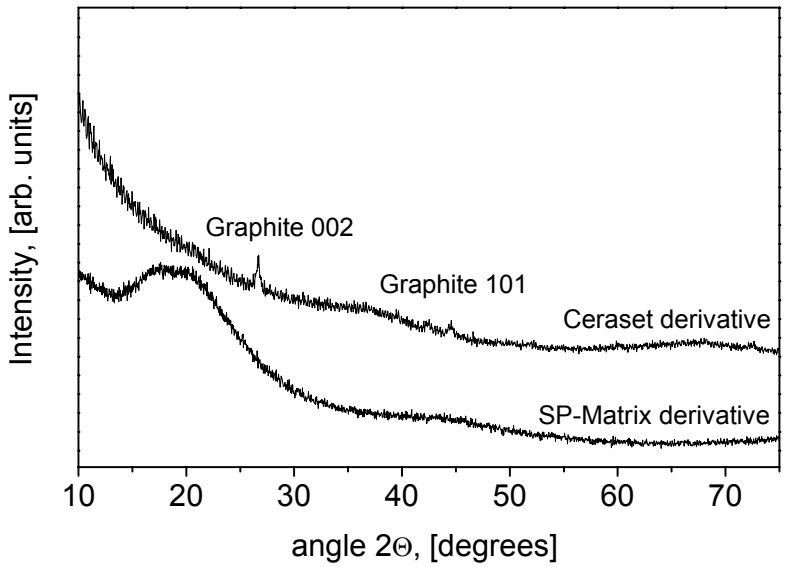

Figure 25. XRD-patterns of the KiON Ceraset polyureasilazane derived template-based nanowires (above) and SP matrix polymer derived wires (below). The broad ‘halo’ signal below 30° can be ascribed to the amorphous nature of the samples.

4.2.1.5 EDX study of SP-Matrix derived SiOC composition

Convincing results suggesting the formation of a nearly stoichiometric SiOC composition were obtained with the help of semi-quantitative standardless EDX analysis of nanowires made from the SP-Matrix polymer, which is the less hydrolytically sensitive from the two precursors used for this study.
Fig. 26 shows an SEM image of the SiOC nanowires derived from SP-Matrix polymer, where the EDX spectrum was taken. Fig. 27 demonstrates the EDX spectrum itself.

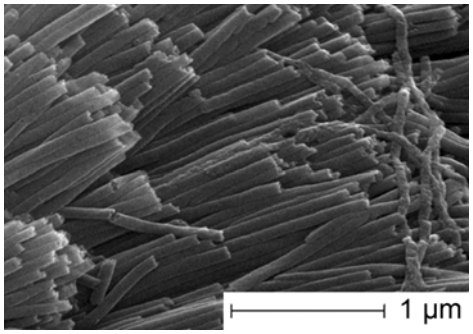

Figure 26. Area of SiOC nanowires, used for the semi-quantitative EDX investigation of their chemical composition.

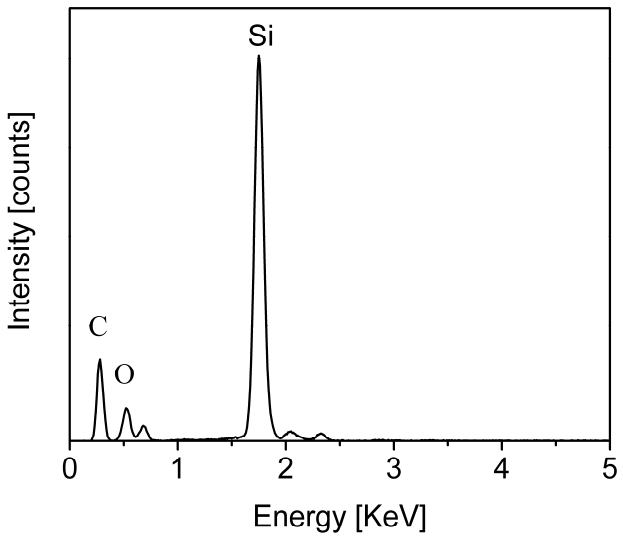

Figure 27. EDX spectrum of SP-Matrix derived SiOC nanowires

The quantitative interpretation of the EDX spectrum shows that the sample contains 11.4 at.-% of silicon, 11.8 at.-% of oxygen, and 73.7 at.-% of carbon. The carbon content can not be estimated from this data because of the contribution of carbon-rich conductive polymer film, which is necessary for SEM samples preparation.

However, polymer-derived SiOC and SiCN ceramics is normally characterised by a significant amount of carbon (up to 40 wt.-%). The model of possible distribution of free carbon phase was developed from viscoelastic properties measurements and represents a system of interconnected domains of approximately 1.5 nm size.[179]
The atomic ratio of Si and O is nearly 1:1, thus the composition of the nanowires may correspond to the stoichiometric SiOC, and the concentration of oxygen has probably no accidental character and is not only due to other phase inclusions (like SiO_2).

4.2.2 Ceramic Nanowires Derived from 20 V PAOX Templates

4.2.2.1 Microscopic study

The SP Matrix polymer was chosen for studying the influence of smaller pore diameters (23 ± 3 nm) of PAOX templates with respect to formation of Q1D ceramic structures. When switching to a template obtained from a sulphuric acid solution, like the one with 23 nm pores one should expect a greater reactivity of the pore walls during the pyrolysis step. In comparison to PAOX prepared from oxalic acid sulfuric acid-derived PAOX templates are known to incorporate a significantly higher concentration of dopant species derived from the electrolyte during their formation process and thus the surface of the pore walls show a higher hydrophilic character due to more surface hydroxy groups as well as adsorbed water.[169] The synthesis of ceramic wires of a smaller diameter was performed in the same way as described in the experimental part for 40 V templates, except longer infiltration times (membranes were fully immersed in the precursor for three days) and the use of a 90 wt. % mixture of the ceramic precursor in n-hexane (to decrease its viscosity). After pyrolysis of the precursor the template was removed in 48% HF solution. As deduced from SEM micrographs a dense arrangement of ceramic wires was obtained (Figure 28). The diameter of the wires was uniform and averaged 26 nm. As with the larger sized template pores there were difficulties to obtain free Q1D structures with 23 nm alumina templates for TEM analysis of the ceramic nanowires derived from the SP matrix precursor (i.e. to disperse them by ultrasonication).

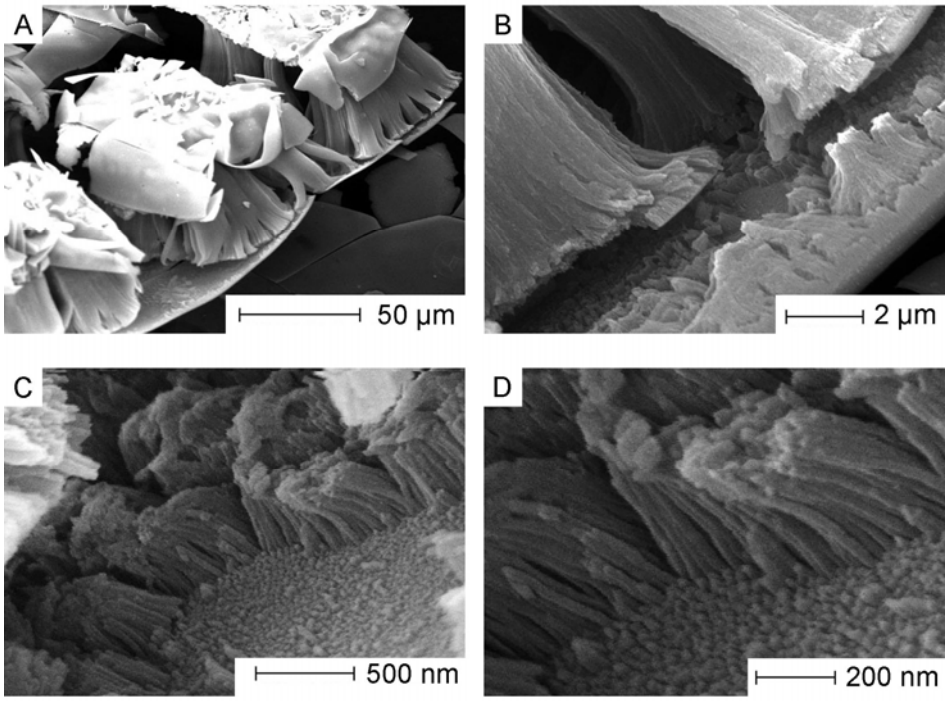

Figure 28. SEM micrographs (A, B) (C and D are higher magnifications of A and B) of the SP matrix polymer-derived wires after complete dissolution of the from PAOX templates.

4.2.2.2 XPS study of ceramic nanowires of a smaller diameter

Based on X-ray photoelectron studies (XPS) the ceramic wires contain some sulphur contamination due to pyrolysis of sulfate anion content present in the PAOX template because of the usage of sulphuric acid as electrolyte (Figure 29).

When comparing the XPS data with pure Si, the measured Si *2s* and Si *2p* binding energies (150.9 and 99.9 eV respectively) of the ceramic nanowires are slightly shifted towards higher values. This effect results from the electrons charge displacement from silicon atoms to the neighbouring more electronegative oxygen and suggests the existence of covalent Si–O bonds in the material. For the accurate quantitative analysis the photoelectron emission from the sample has to be isotropic. This implies a high flatness, homogeneity and purity of the sample surface. In addition to that, XPS is a surface analysis method, and the electrons output depth is only a couple of nanometers (from 100 Å to 6 nm from different literature sources). At the same time, there is always a naturally occurring oxide layer on the ceramic samples, and the composition in the bulk may significantly differ from that on the surface. The calculated atomic percentage of the elements (65.9% C, 7.11% Si, and

26.9% O) shows a large excess of carbon and oxygen. This suggests the prevailing dissolution of surface silica fragments in HF during the PAOX template removal, whereas the carbon phase remains intact.

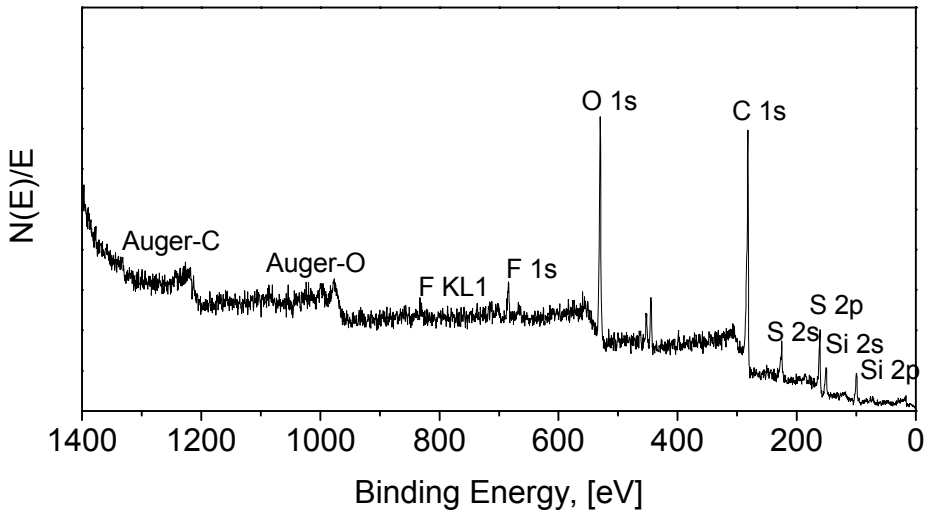

Figure 29. XPS of the SP matrix polymer-derived wires, derived from PAOX templates.

4.2.3 Results, achieved in parallel with the SiOC nanowires synthesis

4.2.3.1 Chemical functionalization of the interior of the alumina pores

Within the framework of the project concerned with the synthesis of silicon-based 2D-arranged Q1D ceramic nanomaterials, the chemical functionalization of alumina pore interior for organosilicon molecular precursor anchoring was performed. This procedure has two purposes:

- To increase the affinity of the pore walls to the polymer, and, thus, to optimise the wettability and pore filling degree due to the capillary actions
- Hydrophobization of the alumina surface should prevent the reaction of hydrolytically sensitive precursors with surface acidic OH-groups and adsorbed water on alumina.

Similar processes of alkylation of hydroxylated surfaces are widely used, for example, in absorbents preparation. The nature of the interaction between adsorbed molecules and hydroxyl groups which exist on the surfaces of all oxides was extensively studied by means of infrared spectroscopy.

As it follows from literature,[180] water and hydroxyl groups can be eliminated according to the Scheme 3 under laboratory vacuum conditions. However, even at 650 °C, 10 % of the alumina surface are still covered with OH-groups.[65]

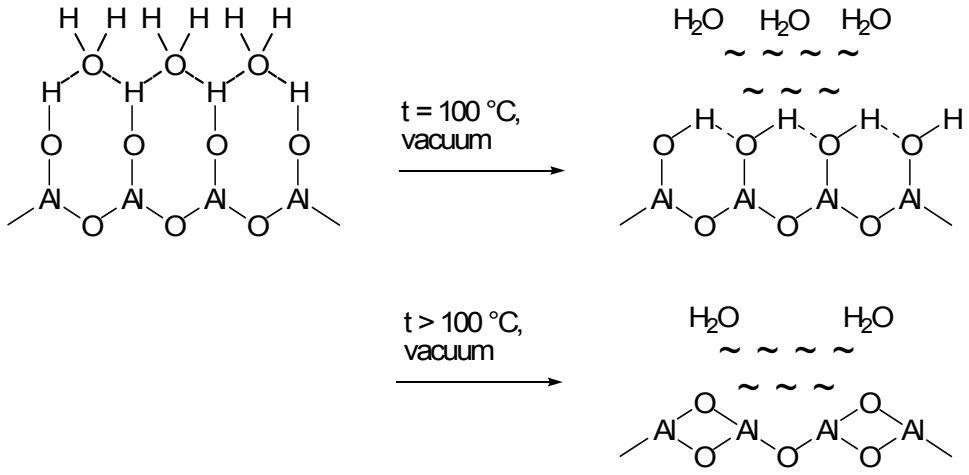

Scheme 3. Elimination of water and hydroxyls from alumina

In the present work, trimethylethoxysilane, dimethyldiethoxysilane, as well as dimethyldichlorsilane were used for chemical modification. Chlorsilanes were not extensively studied because of undesired chlorine impurities incorporation into the final nanostructures.

Chemical modification was performed by immersing of PAOX templates into the liquid reagent in a Shlenk flask under argon atmosphere and reflux for different periods of time. The following reaction undergoes by the example of $(CH_3)_3SiOEt$:

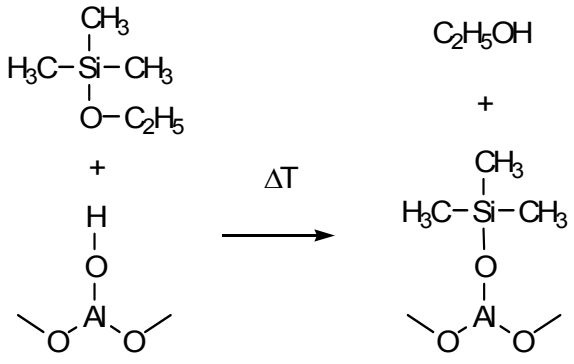

Or, in the case with diethoxy- or dichlorsilanes, the following mechanism is also possible:

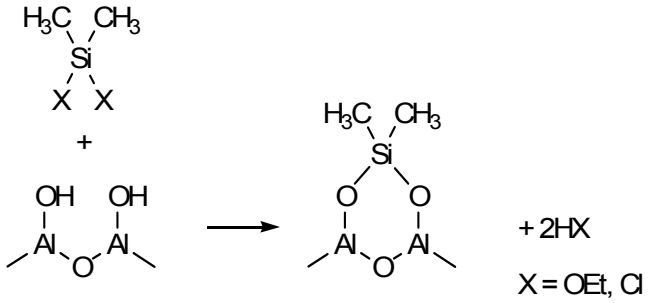

After that, the template was dried in vacuum for half an hour (not chemisorbed volatile silane is removed) and stored in a sealed Schlenk flask under argon.

The even distribution of the modifying reagent along the pores was confirmed by EDX mapping (Si signal at the broken edge of a template) and FTIR. The IR spectrum of an initial 40 V template (not grounded with KBr), made in oxalic acid solution, and templates, refluxed with $(CH_3)_3SiOEt$ for 30 minutes and for 5 hours, as well as the IR-spectrum of individual $(CH_3)_3SiOEt$ are presented in Fig. 30. Fragments of a membrane with the same thickness were analysed directly without diluting with KBr to compare the intensities and the degree of chemisorption. Surface modification is evident from the C-H signals at 2963 cm^{-1} and Si-CH_3 deformation vibration at 1112 cm^{-1} appearing in the IR-spectrum of templates. The wavy spectrum line is very likely the result of the interference of IR-light and the periodic structure of porous ordered templates (unfortunately, no similar investigations were found in the literature to compare the results). Other most intense characteristic IR-bands of the silane fragment on the alumina surface in the region between 1500 and 700 cm^{-1} can not be used for detection, as they are masked by very strong signals from oxalate impurities in the template (the assignment follows from the comparison of the IR-spectra of templates and of self-made aluminium oxalate). There is no large difference in silane-related signals intensities on the templates after 30 min and 5 hr of the reaction, thus, the reasonable coverage of pores interior very likely occurs within a short period of time.

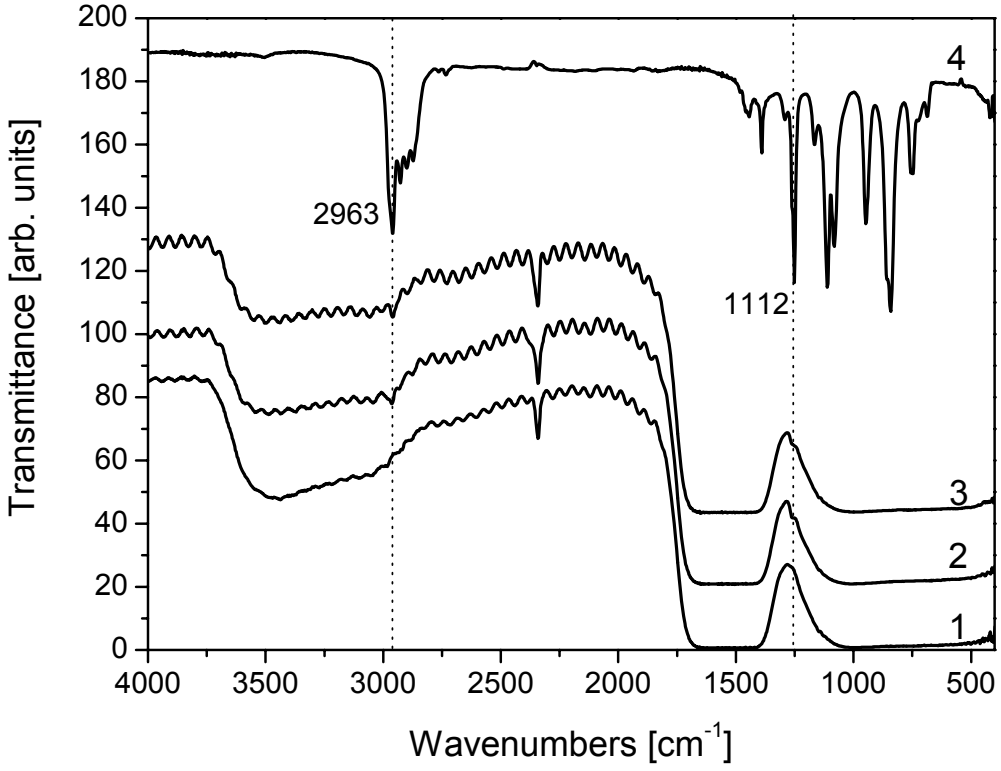

Figure 30. FTIR spectra of a 40 V 'oxalic' membrane without surface modification (1), refluxed with trimethylethoxysilane for 30 min (2) and for 5 hr (3), and of pure trimethylethoxysilane (4).

After the functionalization, the pore filling experiments with organosilanes and template removal with concentrated HF solution were performed in the usual fashion. The SEM images of the resulting material is presented in Fig. 31.

The pores of the template were completely filled in all cases. However, it is evident from the micrographs, that the surface of the nanowires is uneven and looks seriously damaged. The reason for that is very likely the formation of silica fragments on the nanowire surface (Si-O groups from functionalization agents) and following dissolution of those silica grains with HF during the liberation of nanostructures from a template. The surface damage is more noticeable in the case with chlorsilane functionalization than with ethoxysilanes.

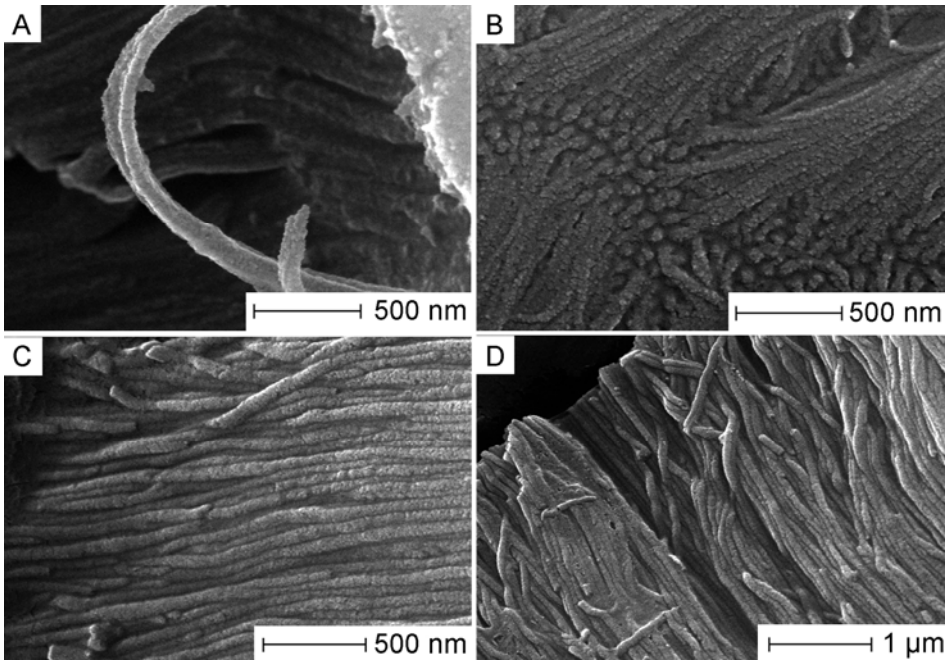

Figure 31. SEM images of SP-Matrix® derived ceramic nanowires from 40 V templates, modified with dimethyldichlorsilane (A, B) and dimethyldiethoxysilane (C, D).

This experimental investigation shows that, along with the possible increase of the affinity of the pore interior to the liquid precursors, and pore filling degree, surface modification accounts for the damage of the nanostructures during the template wet etching procedure. Thus, due to the undesired side effects, no further detailed study of this approach was carried out.

4.2.3.2 SiC/C core-shell composite Q1D nanostructures

In the recent years, Q1D heterogeneous nanostructures with well defined interfaces, called heterojunctions, have attracted a great attention.[4] Different types of heterojunctions are possible: 'segmented' (end-to-end, called also 'superlattices'), 'branched' (brush-like), or 'core-shell' (core and sheath, coaxial structure). The advantage of these structures is that they can combine useful properties of components, and sometimes also gain new properties. As regards the SiC/C structures, SiC is valuable for its electrical properties and offers new possibilities for nanoscale high-temperature, high-frequency and high-power devices,[181, 182] amorphous carbon provides the system with its special chemical properties, inertness towards polar agents and highly developed surface, which opens up

possibility to use the structures for sensor applications. In the case with template-based synthesis using porous alumina, a carbon layer can protect the liquid pre-ceramic precursor from the reactive PAOX, and, after the synthesis and isolation of nanostructures, can play a role of excess carbon source during the high-temperature conversion of amorphous products into crystalline. Additionally, the samples can be annealed in the air to remove carbon and get SiC, not damaged by There is a number of SiC/C heterostructures reported: carbon nanotubes covered with SiC by a solid-solid reaction ,[183] SiC nanoparticles encapsulated in carbon nanotubes,[184] SiC/C core-shell nanowires prepared by extracting of carbon from outer SiC region with Cl_2/H_2.[185]

In the present experiment, 27 or 40 V PAOX templates were open from both sides and covered with a thin carbon layer (several nm) by CVD process using ethylene flow at 600 °C in an induction furnace. After that, the SiC-precursor was infiltrated and converted in Ar by the usual method. The template was removed in concentrated HF. The whole process is shown in Scheme 4.

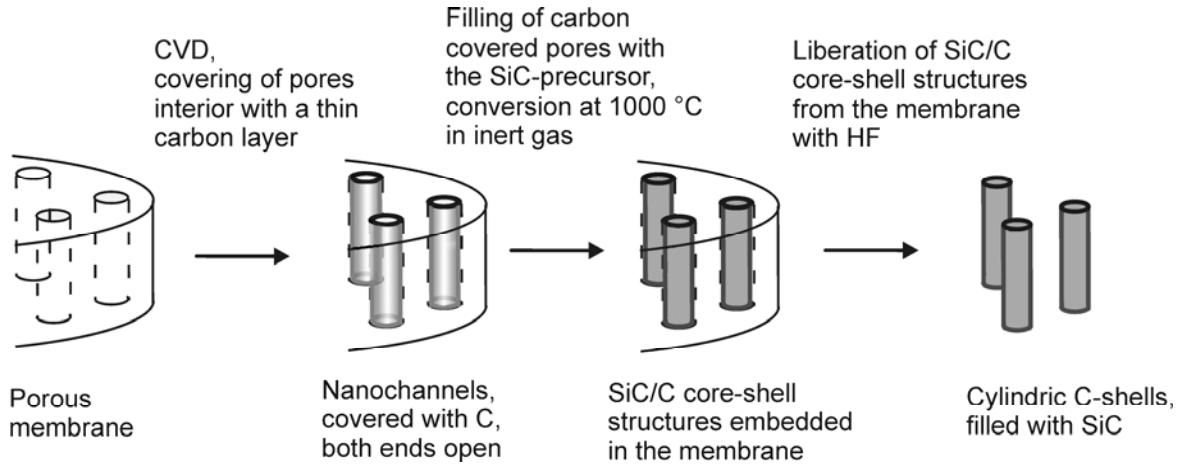

Scheme 4. The process, leading to the C/SiC core-shell Q1D nanostructures from PAOX membranes.

Results of the experiments are presented in SEM images in Fig. 32. SiC filling can not be seen through the C shell, but the EDX spectrum shows a very intense signal of silicon, which indicates the presence of desired material in the carbon nanotubes.

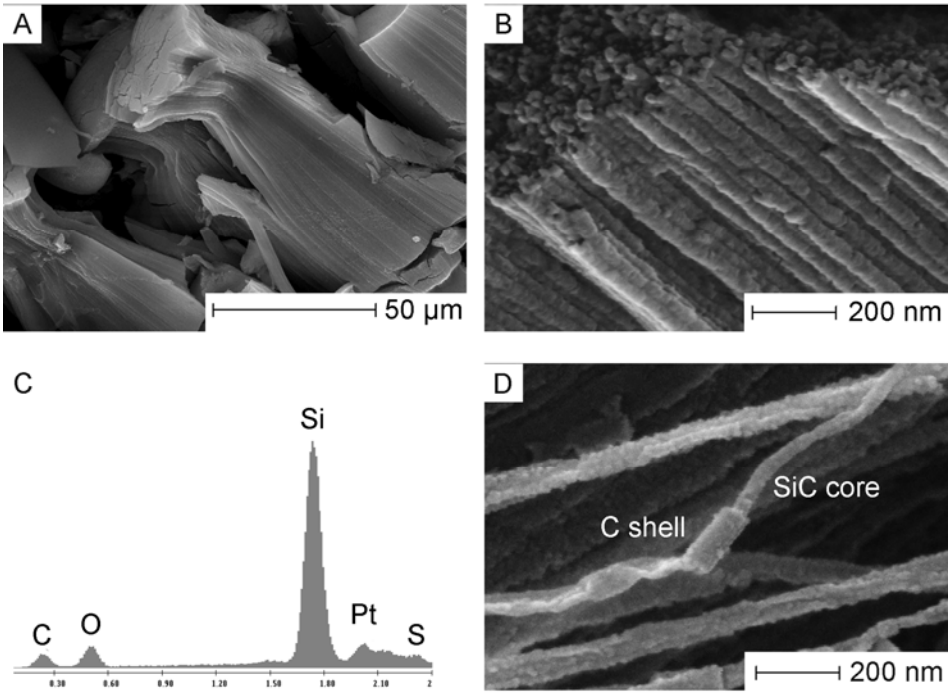

Figure 32. Core-shell SiC/C nanowire arrays, obtained from 27 V templates with pore diameter around 30 nm (A, B); EDX spectra of 30 nm nanowires (C); part of a broken C-shell around SiC wire from 40 V template, showing the two-layer morphology of the obtained heterojunctions (D).

The EDX analysis penetrates into the sample at a depth of approximately 1 µm, thus, it allows to investigate the volume of the core-shell nanowires as well. The small sulphur signal is due to the impurities in PAOX template obtained from sulphuric acid solution, and release of SO_2 during the pyrolysis step. A fragment of the broken carbon shell around the wire from a 40 V template is shown in Fig. 78 D and demonstrates the achieved morphology: a wire is surrounded by the shell of a uniform thickness.

The morphology is also confirmed in TEM micrographs (Fig. 33). It is seen that the material is encapsulated in a shell composed from small graphitic layers. The lighter inner region does not show any ordered structure and may correspond to fragments of a totally amorphous phase. The inner region consists of partitions, more and less dense regions, which can result from the polymer shrinkage during pyrolysis or capillary instability effects during the filling procedure. However, the obtained TEM images do not give a definite answer about the filling degree. In this regard, more valuable information is provided by EDX analysis, because the experimental

procedure excludes any possibilities for silicon to be on the surface of nanotubes, but not inside them.

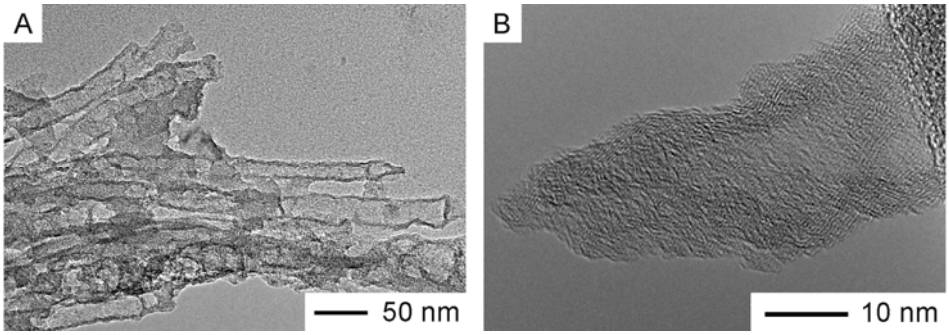

Figure 33. TEM images of SiC/C core-shell nanowire arrays (A) and a close-up of a single nanowire tip (B)

To liberate the SiC nanowires, the core-shell structures were kept at 750 °C in the air in a muffle furnace for 2 hours. This experiment was performed to remove the carbon layer and to achieve the free ceramic nanowires made from the hydrolytically sensitive precursor, which never had direct contact with alumina template, thus, it should have less silica in the composition than usually.

The resulting material was monitored with SEM only. Fig. 34 presents the images after two identical experiments with the material from 27 V and 40 V alumina templates. It is seen that there is a fibrous residue after the carbon burning-off, but the expected nanowires have a spongy structure and tend to unite into a thicker objects. Unfortunately, it could not be concluded from the SEM images, whether the spongy texture results from the carbon residues or from the damaged surface of amorphous silicon carbide.

The future plans along this line of investigation are to vary the conditions of the carbon shell removal and to explore the morphology with microscopic methods, as well as to convert the silicon carbide into the crystalline form at temperatures exceeding 1600 °C under vacuum conditions. The preliminary experiments show that carbon nanotubes remain intact after such treatment, but their crystallinity is improved substantially.

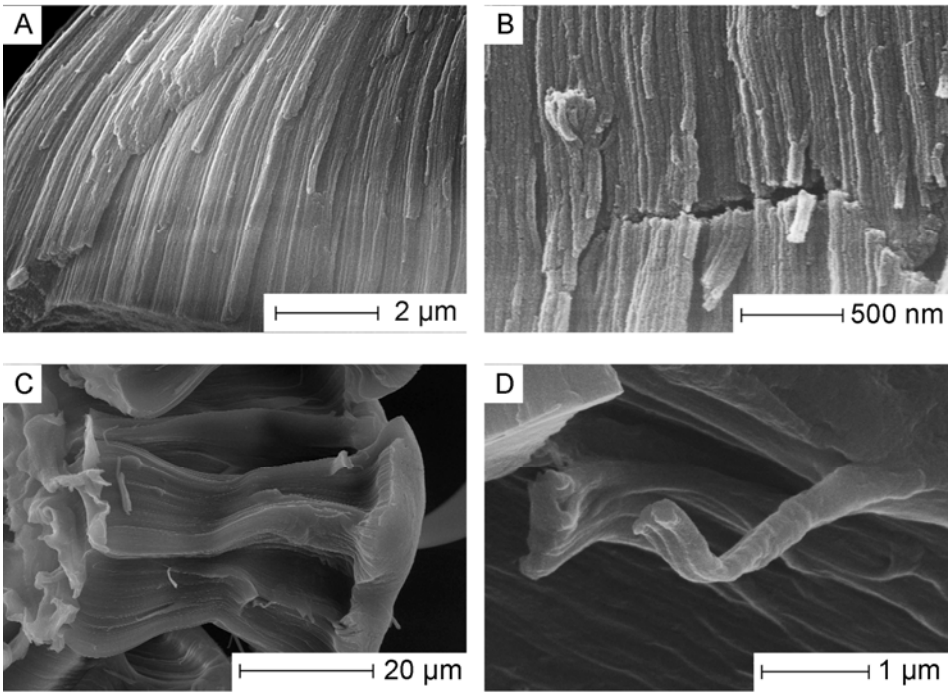

Figure 34. Results of the carbon shell burning-off at 750 °C in the air for SiC/C core-shell structures from 27 V templates (A, B) and from 40 V templates (C, D).

4.2.4 Brief summary of the results obtained for SiOC nanowires

A successful attempt to alter the geometry of silicon-based ceramic nanowires by means of PAOX pore size tailoring has been made. However, diverse optical, spectral and structural characterization methods confirm the active participation of the PAOX matrix in reactions with the Si ceramic precursors within the nano channels and the influence on the chemical composition of the nanostructures synthesized therein. Since anodic alumina is not inert at elevated temperatures, templated Si-based inorganic materials typically have a certain amount of oxygen in the composition.

Aluminium oxide obtained from electrolytic anodic oxidation of aluminium metal usually display a complex composition formulated as $AlO(OH)•(H_2O)_n$. Water-free surfaces are accessible via calcination at 300 – 400 °C, but still this process leaves up to 10% of the porous surface covered with hydroxyl groups. At the same time, many organosilicon polymers are hydrolytically sensitive substances. Our results show that alumina templates composed of such a nonstoichiometric composition $AlO(OH)•(H_2O)_n$ do react at higher temperatures with all three precursors employed

in this study (KiON Ceraset polyureasilazane and polycarbosilane SP Matrix Polymer) to form one dimensional SiOC materials. Under high temperature conditions (in the case of our experiments the ceramization of the precursor occurs at 1000 °C and in the common temperature range up to 1000 °C the precursor is oxidation sensitive) PAOX templates are even further reactive towards these Si based ceramic precursors.

4.3 Characterisation of Track-Etched Polycarbonate Templates

Due to the lower thermal resistance in comparison with PAOX membranes, track-etched polycarbonate templates are normally used for low-temperature replication methods only (e.g. electrochemical deposition of metals from aqueous solutions). Thus, the compatibility of these templates with the employed metal oximato precursors, which need a thermal conversion step towards expected oxides, is not clear. In this section, the porous morphology and the thermal properties of the Whatman Nuclepore™ membranes are studied to find the optimal conditions for replication experiments.

4.3.1 SEM study

Commercial nuclear track-etched polycarbonate membranes with 0.1 µm nominal channel diameter were investigated by means of SEM. The actual visible pore size estimated from micrographs varied in the range between 70 and 200 nm (Figure 35). The thickness of the templates was around 5-6 µm.

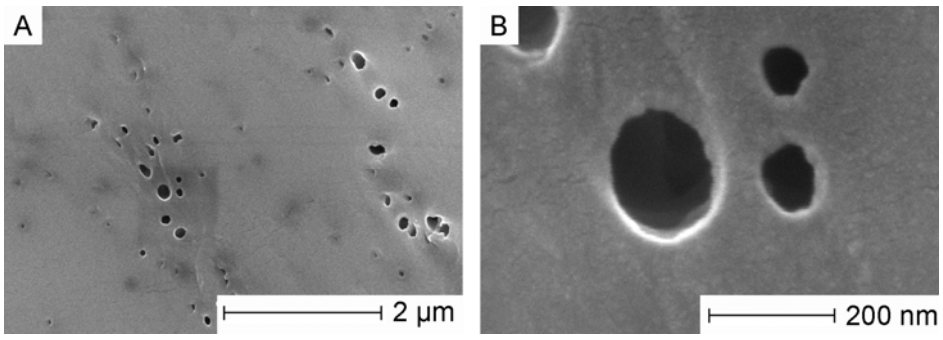

Figure 35. SEM pictures of the surface of Whatman Nuclepore® membranes, nominal size of randomly scattered pores is 0.1 µm.

4.3.2 TG-MS study

TGA analysis of polymeric membranes with MS-coupling suggests stability in oxygen atmosphere up to approximately 340 °C and full combustion up to 600 °C (Figure 36). Thus, it is possible to treat the polycarbonate filters at temperatures around 200 °C for the purpose of metal oxide precursors modification for a short period of time, where no visible signs of polymer destruction were observed.

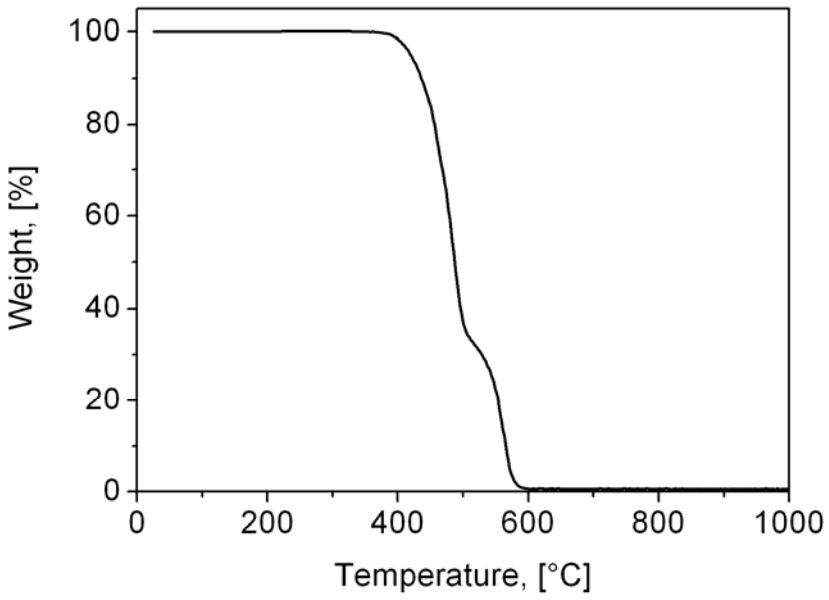

Figure 36. TG curve of the commercial polymeric porous membranes analysed in oxidizing atmosphere.

A complete MS-analysis of the released gases is presented in Fig. 37. The release of gaseous decomposition products from Whatman Nuclepore™ templates and the corresponding sharp increase of ionic currents was detected in the temperature interval between 400 and 600 °C First, water (H_2O, m/z^+ 18) and carbon dioxide (CO_2, m/z^+ 44) is released, presumably, not only from decomposed polymer but also including gas and moisture adsorbed in the pores. Some decrease of the ionic current corresponding to oxygen (O_2, m/z^+ 32) is observed, as it is consumed during oxidative processes. Further decomposition reaction is accompanied by the significant release of carbon monoxide (CO, m/z^+ 28), and detectable amounts of benzene (C_6H_6, m/z^+ 78) and phenol (C_6H_5OH, m/z^+ 94).[44, 46]:

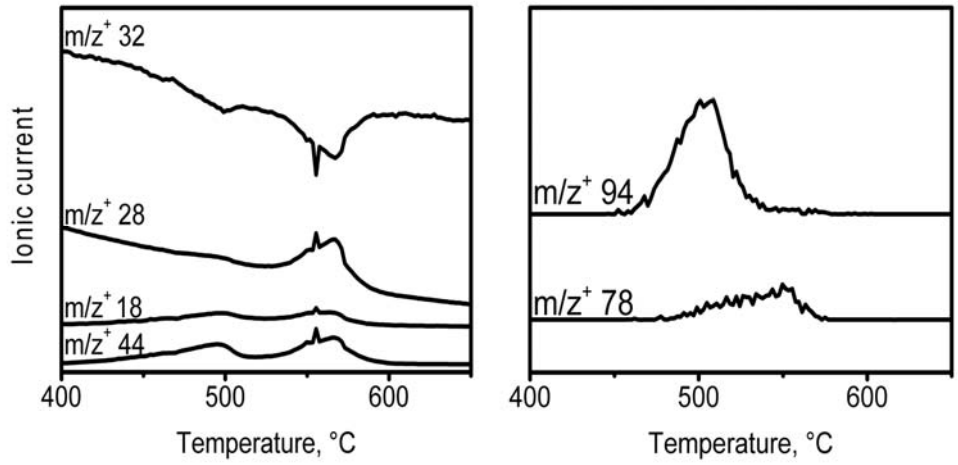

Figure 37. Qualitative MS curves of the commercial polymeric porous membranes analysed in oxidizing atmosphere.

Scheme 5 shows the decomposition reaction as suggested by experimental data:

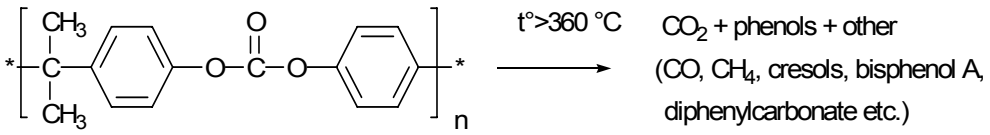

Scheme 5. Thermal decomposition of polycarbonate.

Obtained TG curves reveal that the commercial Whatman Nuclepore™ membranes are essentially polycarbonate. No signs for copolymerisation, blending or other modifications were evident.

The thermal behaviour of the porous track-etched polycarbonate templates in inert gas atmosphere (helium) was carried out to explore the possibilities of the synthesis of doped Q1D systems (e.g. with manganese II) within nanopores in non-oxidizing environment.

The result of TG study in helium atmosphere is presented in Fig. 38. As seen from the image, the template is stable up to approximately 410 °C, and then a steep thermogravimetric event takes place. This rapid process is finished at a temperature around 550 °C, and then the weight gradually decreased up to the final analysis

temperature. The remaining carbonized residue at 1000 °C is 10.5 % of the initial sample weight.

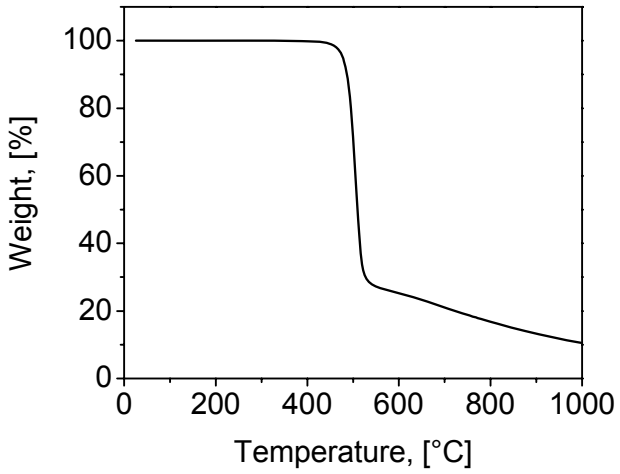

Figure 38. TG curve of the commercial polymeric porous membranes analysed in inert gas (He) atmosphere.

The changes in ionic currents detected via mass-spectrometry are demonstrated in Fig. 39. The character of the ionic currents curves is almost identical to that one of the samples analysed in oxygen, but the intensity of the signals is very low, as the only oxygen source for oxidation is the polycarbonate itself and the gases possibly adsorbed on the membranes' surface from the air during the storage.

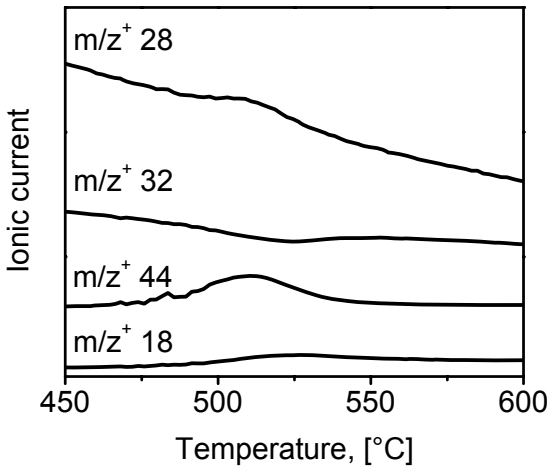

Figure 39. Qualitative MS curves of the commercial polymeric porous membranes analysed in inert gas atmosphere.

4.4 Q1D MgO nanostructures from the precursor Tris(aqua)-Bis[2-(methoxyimino)-propanoato]magnesium

In this section, the synthesis of polycrystalline magnesium oxide nanorods using track-etched polycarbonate films as templates and a soluble Mg precursor complex was studied. This approach gave the possibility to achieve the formation of Q1D MgO nanofilaments in template pores, which can be freed from the template afterwards with the help of an organic solvent under mild conditions.

4.4.1 Thermal decomposition of the precursor

4.4.1.1 TGA study

The thermal decomposition of the molecular MgO precursor Tris(aqua)-Bis[2-(methoxyimino)-propanoato]magnesium was studied under oxygen as well as under helium atmosphere (Figure 40).

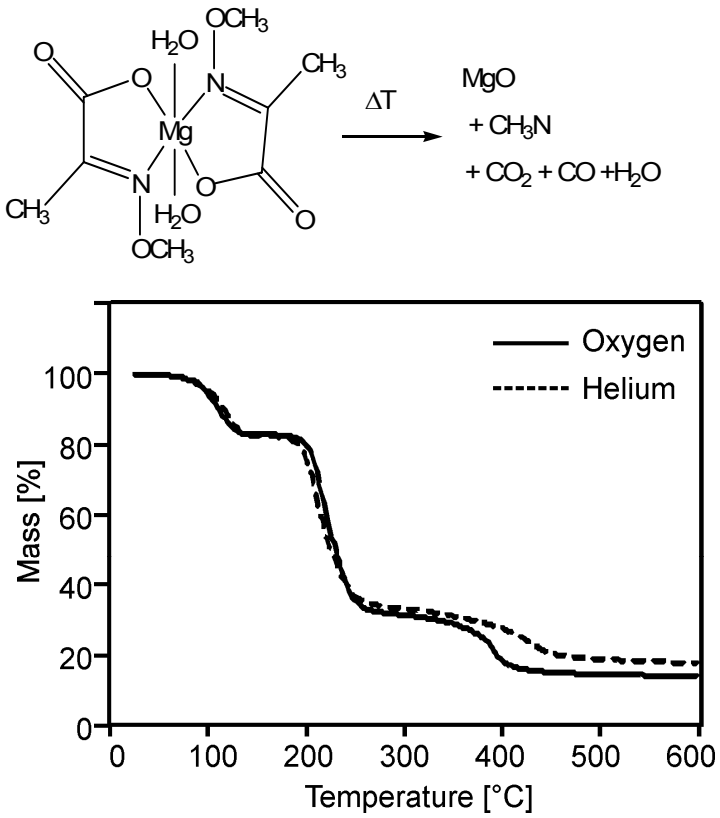

Figure 40. TG curves for decomposition of MgO precursor in oxygen (solid line) and helium (dashed line).

In a first step at about 90 °C the coordinated water molecules are removed. In the next step the decomposition of the ligand framework starts at about 190 °C. The gaseous decomposition products, according to mass-spectrometry, resemble those of the decomposition of the corresponding zinc oximato complex.[11, 186]

At higher temperatures, however, an additional decomposition step is detected. The temperature, at which this final step occurs, depends on the reaction atmosphere employed; 380 °C in oxygen and about 425 °C in helium. The theoretical ceramic yield (12.97 %) is only obtained in oxygen, whereas in the case with helium it is always visibly higher, indicating variable remainder in the resulting ceramics.

4.4.1.2 XRD study of the products, obtained from MgO precursor at different decomposition temperatures

For the identification of the ceramic products obtained from calcination experiments at various temperatures in air, X-Ray diffraction measurements of powders were carried out (Figure 41).

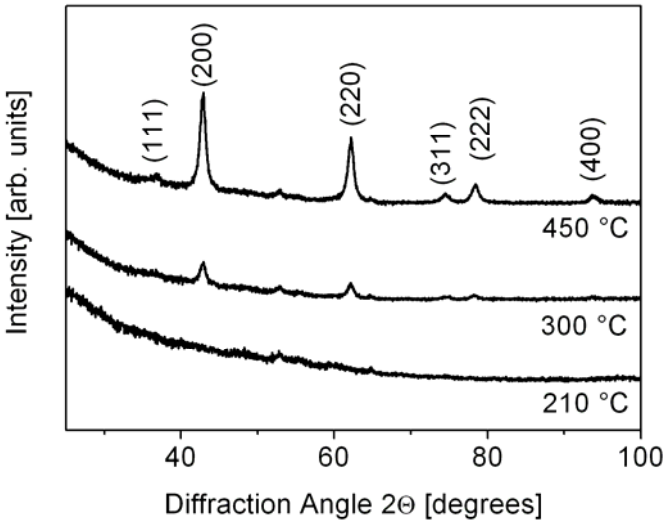

Figure 41. XRD patterns of the precursor decomposed at various temperatures for 1h.

Whereas powders calcined at 210°C appeared to be amorphous, after raise of the temperature to 300°C, cubic MgO[187] was observed as the single product. This is below the last decomposition step in the TG and also below the decomposition temperature of known magnesium carbonates to magnesium oxide.[188, 189] It can

therefore be assumed, that the decomposition of the precursor leads to magnesium oxide and organic residues, whereby the latter can be burned out completely at higher temperatures. This is also in accordance with the dependance of the temperature of the last reaction step on the atmosphere in TG.
The width of (200) diffraction peak at its half-height at 450 °C is 0.84° and corresponds to the crystallite size of 10.8 nm, as derived from the Scherrer formula.

4.4.2 Preparation of polycrystalline MgO nanorods within track-etched polymer template

4.4.2.1 Microscopic study of 'green body' and MgO Q1D structures

Nanorods were obtained by a two-step replication procedure described in experimental part.The molded rod-like structures were monitored with SEM after each synthetic step. The diameter of the 'green body' rods after infiltration, dehydration and solidification at 160 °C, and removal of the polymeric template with CH_2Cl_2 was about 95-140 nm (Figure 42). This spread in values is caused by the irregularity or pore sizes in the initial polycarbonate template, but the molded rods have a slightly narrower diameter distribution. The length of the rods was 5-6 μm and exactly replicated the template channels. A very thin flat layer connecting the rods, originating from the precursor outside the template (on the top surface), is observed as well.

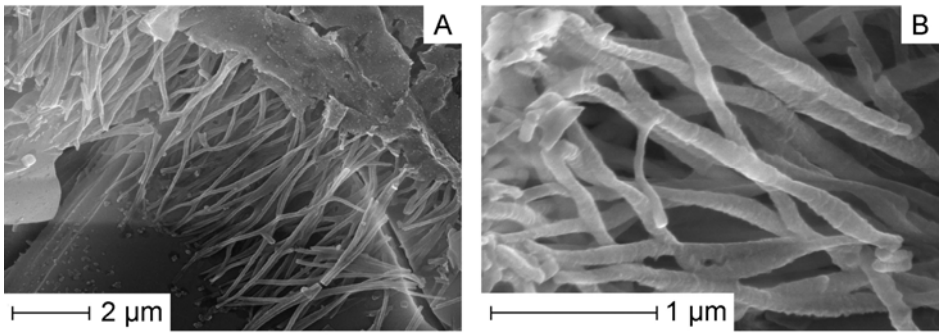

Figure 42. SEM image of the molded precursor array dehydrated at 160 °C and isolated from the polymeric template.

The following dimensions of the MgO rods after calcination in the air at 450 °C can be estimated from SEM images obtained (Figure 43): length about 2-4 μm, the diameter averaged 80 nm. It is evident from the cross-sections where the rods were broken that there is no tubes formation, only filled rods are seen. The reason for this might be that the precursor undergoes densification and shrinkage during the thermal treatment.

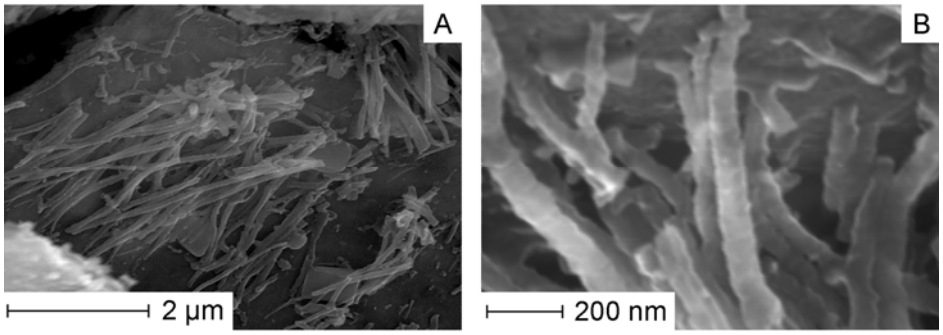

Figure 43. Separate polycrystalline MgO rods after calcination at 450 °C.

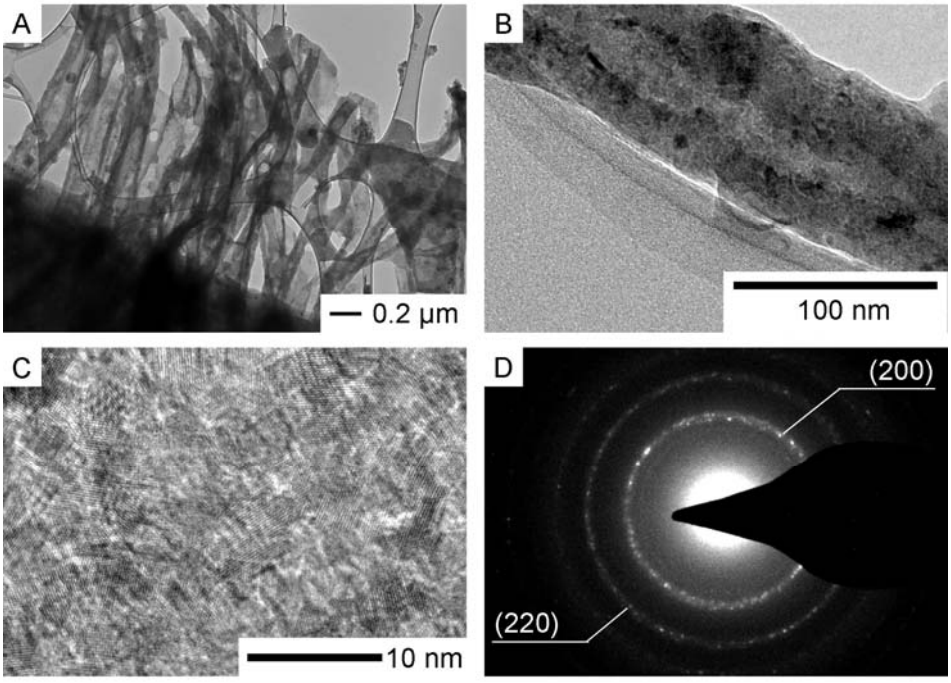

Figure 44. TEM images of MgO nanorods bundle (A); a single rod with diameter around 90 nm (B); the polycrystalline nature of the obtained material is confirmed in TEM (C) and SAED (D).

According to TEM images (Fig. 44 A), the rods are arranged in bundles parallel to each other. The diameter of a single rod averages 90 nm (Fig. 44 B). At a higher magnification, the polycrystalline nature of the material is visible (Fig. 44 C). A rod is composed of smaller randomly oriented irregular particles, and this morphology is confirmed by diffuse rings in SAED pattern (Fig. 44 D).

4.4.2.2 EDX Study

The result of EDX analysis of MgO rods is presented in Fig. 45. As follows from the standardless quantification method, the compound contains 39.4 wt % of magnesium, 50.6 wt % of oxygen, and 7.6 wt % of carbon. According to the stoichiometric composition of magnesium oxide, the weight content of Mg and O has to be 60 % and 40 % respectively, and there is definite excess of oxygen in the sample under consideration. The disagreement in magnesium to oxygen stoichiometric ratio in the final product is very likely due to the slow reaction of MgO rod surface under ambient conditions with CO_2 and H_2O yielding magnesium hydroxide and magnesium carbonate:

$$2MgO + CO_2 + H_2O \rightarrow MgCO_3 + Mg(OH)_2.$$

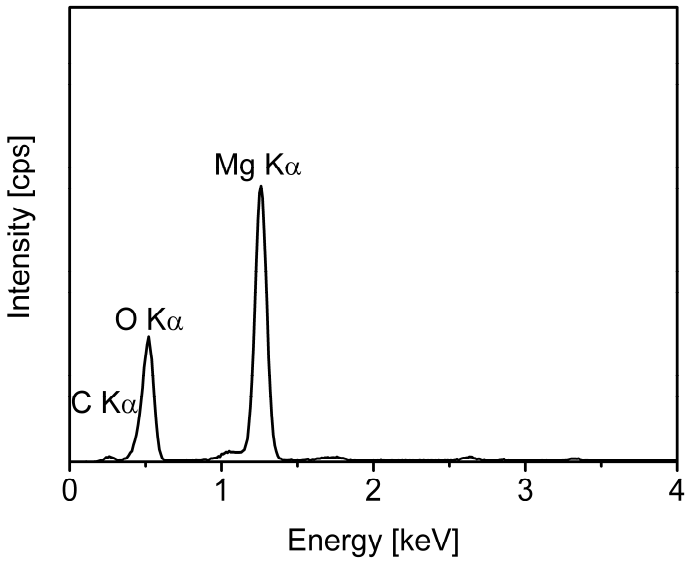

Figure 45. EDX spectrum of the rods calcined at 450 °C.

The atomic Mg:O ratio of the analysed product (1:1.93) is close to such in $Mg(OH)_2$. A high content of carbon, which can exist on the surface in form of $MgCO_3$, has to be taken into account as well.

4.4.2.3 XRD study of the MgO nanorods

The XRD pattern of the MgO rods after calcination at 450 °C is demonstrated in Fig. 46. The width of the most intensive (200) diffraction peak at its half-height is the same as such for the unstructured samples. This means, that the molding of the rods did not change the size of composing crystallites.

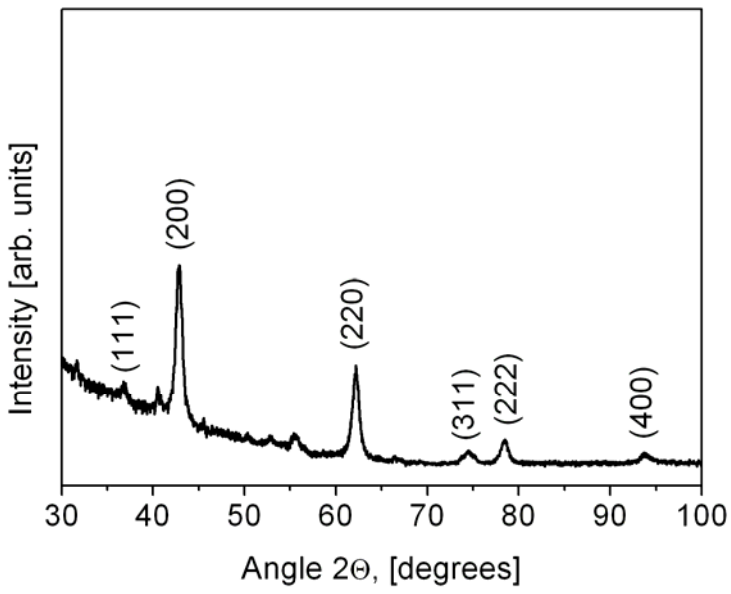

Figure 46. XRD pattern of MgO rods.

4.4.2.4 PL study of the MgO nanorods

To characterize the optical properties of the rods obtained, the material was studied by means of PL spectroscopy. This method is useful to examine the coordination of ions in the lattice and to describe structural defects in crystalline material.[190] The spectra of a powder specimen produced without template and a sample of the

nanorods are compared in Figure 47. Since both samples showed only weak luminescence, a lower excitation wavelength from known from literature (240 and 280 nm) was chosen in order to increase the signal intensities.

When excited with 240 nm ultraviolet radiation, both samples exhibit a broad band centred at 394 nm (3.15 eV). This result can be attributed to oxygen vacancies.[191]

A similar signal at 380 nm is found in PL studies of MgO sol-gel particles and is associated with low coordination surface O^{2-} ions that are surrounded by four counterions.[190] The appearance of luminescence in the region between 340 and 450 nm (excitation wavelength 240 ± 10 nm) is supposed to originate from surface OH groups and is strongly dependent on the amount of adsorbed gases, primarily H_2O and CO_2.[192-194] This fact suggests a less hydroxylated surface of the templated nanorods than of the unstructured sample.

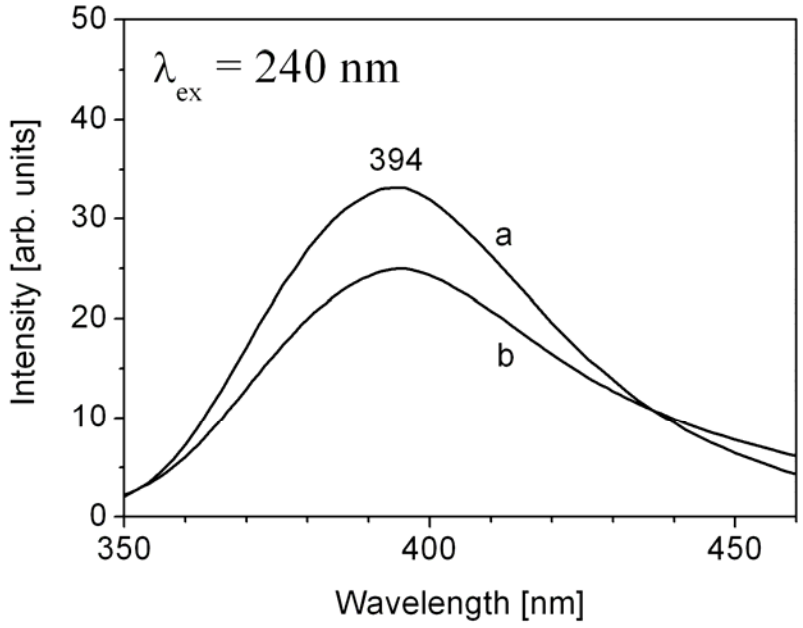

Figure 47. PL spectra of (a) powders from synthesis without template and (b) nanorods from template-directed synthesis.

4.5 Indium oxide nanotubes from oximato precursor

In this chapter, the template based approach to the synthesis of polycrystalline indium oxide nanotubes using track-etched polycarbonate films and a novel indium oximato complex solution as starting materials is described. Sensor tests were performed to study gas sensors based on identical material (In_2O_3 derived from the same precursor) but with different morphology, in forms of nanotubes and unformed Q0D particles, to evaluate the role of an increased accessible surface area.

4.5.1 Properties of the precursor

The precusor (decomposition scheme is shown below) is soluble in a broad range of polar protic (e.g. methanol or methoxyethanol) and aprotic (e.g. tetrahydrofuran, dichloromethane) solvents, but decomposes in water. However, the precursor and its solutions are reasonable stable under ambient conditions.

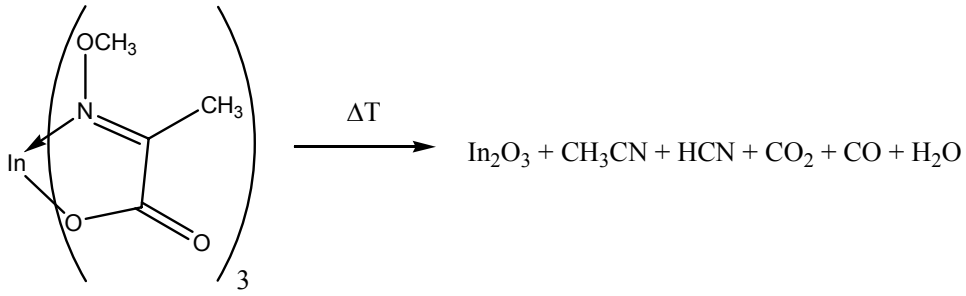

The decomposition (Figure 48) was studied in oxygen and as well as helium by means of thermogravimetry. Under oxygen atmosphere the first decomposition is already observed at about 40 °C. This is followed by a rather broad step between 150 and 240 °C, and continuous mass loss thereafter. A last decomposition step is observed at about 850°C, after which a residual mass of 30.14 % (calculated 29.97 % for complete conversion to In_2O_3) remained.

The reaction in helium was also measured to obtain a complete picture. The curve shows a different characteristic than the corresponding curve in oxygen. Especially the residual mass is lower with 19.97 %. Since no obvious sublimation could be observed, it can be assumed, that reduction reactions occur between In(III) and

residual organic, i.e. near stoichiometric In_2O_3 cannot be obtained in helium. This reaction was therefore not studied further.

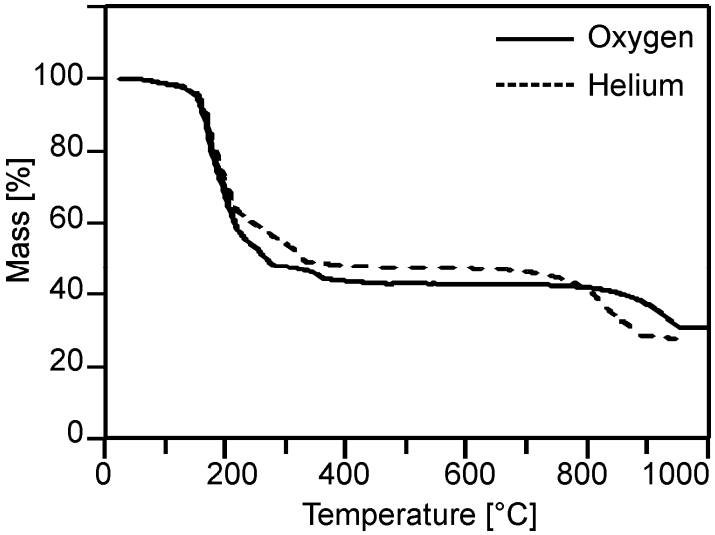

Figure 48. TG curves for decomposition of In_2O_3 precursor in oxygen (solid line) and helium (dashed line).

The results of ex-situ XRD studies of decomposition products at different temperatures are shown in Fig. 49. It is seen that the crystalline indium oxide is formed already at 350 °C, and then the growth of crystals takes place at higher temperatures (narrow reflexes at 450 °C).

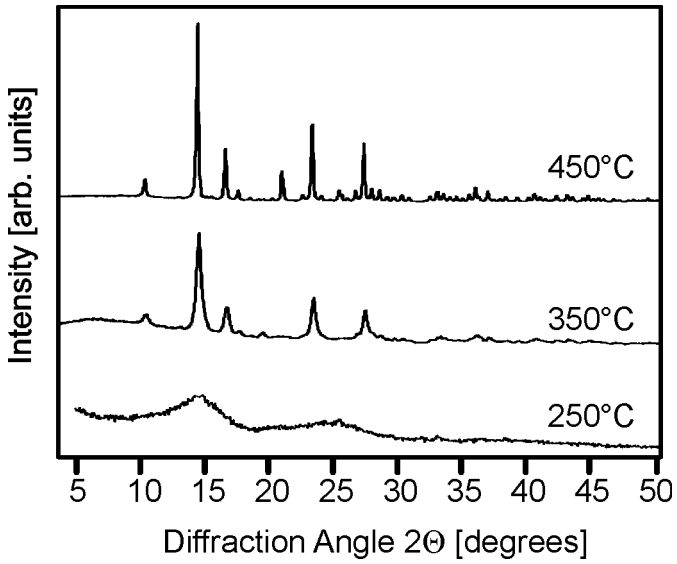

Figure 49. XRD patterns of the precursor decomposed at various temperatures for 1h.

4.5.2 Preparation of polycrystalline In_2O_3 nanotubes from molecular Tris[2-(methoxyimino)propanoato]indium precursor with polymer templates

4.5.2.1 Microscopic study of 'green body' and In_2O_3 Q1D nanostructures

Nanotubes were obtained by the same two-step replication procedure as previous MgO nanorods. The templated material was monitored with SEM after each preparation stage. The images taken after infiltration of the precursor, drying, solidification at 160 °C and removal of the polymeric template with CH_2Cl_2 are shown in Figure 50 (A, B).

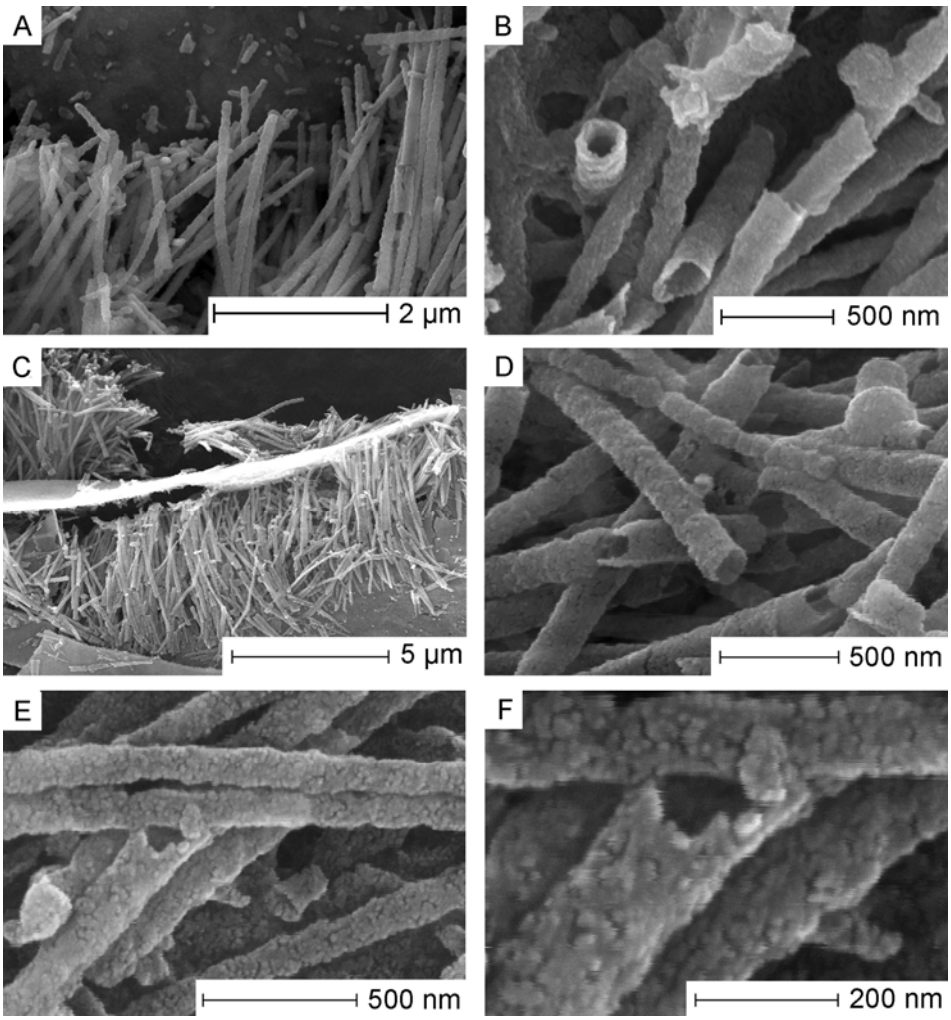

Figure 50. SEM image of the 'green body' nanotubes dehydrated at 160 °C and isolated from the polymeric template (A, B), polycrystalline In_2O_3 tubes after calcination at 350 °C (C, D), and the particulate structure of the nanotube walls at high resolution (E, F).

It is evident from the cross-sections where the structures were broken, or from the ends view, that there is only tubes formation. The outer diameter of 'green body' nanotubes was about 120-200 nm and the tube walls were about 35-40 nm. This spread in values is due to the irregularity or pore sizes in the initial template. The length of the tubes was around 4-5 μm and repeated the template channels in this regard. A thin flat film (maximal thickness up to 200 nm) uniting the tubes, which originates from the dry precursor deposit on the template surface, is observed in some cases as well. The following dimensions of the In_2O_3 tubes after thermal treament in the air at 350 °C can be estimated from SEM images obtained (Fig. 50 C, D): length about 5 μm and the diameter in the range between 100 and 170 nm. A smaller diameter of the tubes, as well as some thinner tube walls, resulted from the shrinkage of the precursor during the conversion into indium oxide. The occasional decrease in length does not have any regular character and results only from the cracking of the material during the thermal cure. The thin flat uniting layer was also occasionally present at one side of nanotubes arrays. At a higher magnification, the particulate porous morphology of the nanotube walls is noticeable (Fig. 50 E, F). The roughly estimated from high resolution SEM images size of the grains is about 15-35 nm.

A TEM micrograph of a single tube with 120 nm diameter is demonstrated in Figure 51 A.

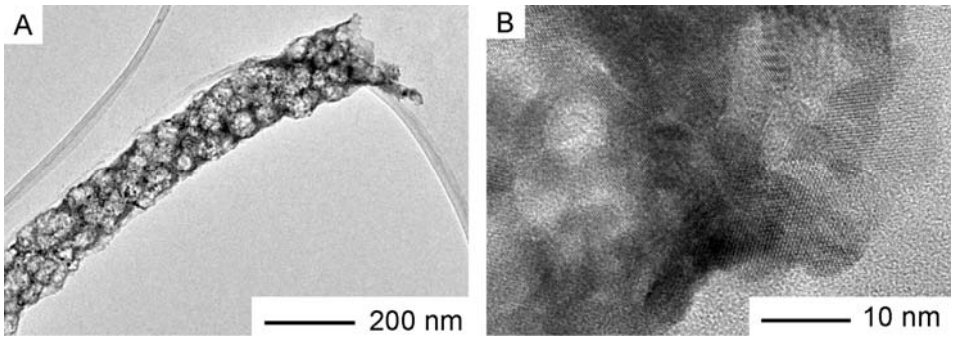

Figure 51. TEM image of a single nanotube (A), and composing crystalline nanoparticles (B).

As seen from more and less dense (light and dark) regions of the image, a tube is not solid and has a porous morphology. A slightly increased porosity in comparison with that seen in SEM pictures is due to the ultrasonication of the material in ethanol, which is necessary for disintegration of tubes bundles into single tubes for the

following investigation with TEM. As the samples for transmission microscopy were prepared in the same way as for sensor tests, TEM micrographs represent the morphology of sensing layers studied later on. At a higher magnification, the polycrystalline nature of the material is visible (Fig. 51 B). A tube is composed of smaller randomly oriented irregular particles, the size of particles varied in the range 10-26 nm.

4.5.2.2 EDX Study of In_2O_3 Q1D nanostructures

The result of EDX analysis of final polycrystalline tubes is presented in Figure 52.

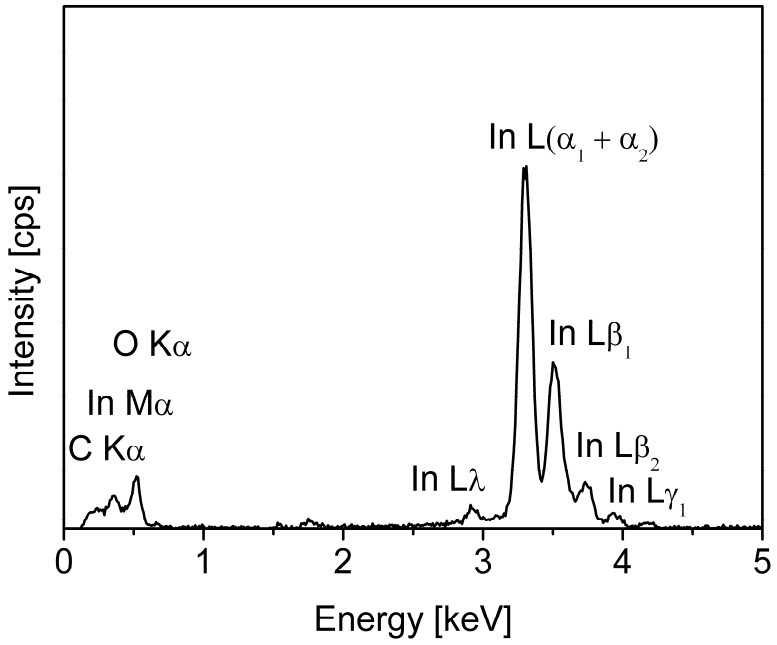

Figure 52. EDX spectrum of the polycrystalline In_2O_3 nanotubes.

Signals only from indium, oxygen and carbon are present. Carbon was detected, but the signal from the conductive carbon-rich film on the sample holder has to be taken into account. The rest of the detected material (without carbon) has 81.4 wt % of indium and 18.6 wt % of oxygen. These values are in complete agreement with the stoichiometric composition of indium oxide, where the weight contents of the elements are 82.7 % and 17.3 % respectively (error of the EDX analysis method is around 1 wt %).

4.5.2.3 XRD Study of In_2O_3 Q1D nanostructures and comparison with In_2O_3 Q0D nanoparticles

The X-ray diffraction pattern of the calcined at 350 °C nanotubes is demonstrated in Figure 53 a. All the reflexes corresponding to cubic indium oxide (JCPDS 06-0416) are present, and no other impurity phase was detected. The width of the most intense (222) diffraction peak at its half-height is 0.38°, and the corresponding average crystallite size calculated by Scherrer formula is ≈ 20 nm, which is in agreement with the values estimated from SEM and TEM micrographs. Patterns of unmolded Q0D particles (Fig. 53 b) show identical composition to that one of nanotubes, but exhibit slightly more noticeable reflexes broadening (up to 0.60°).

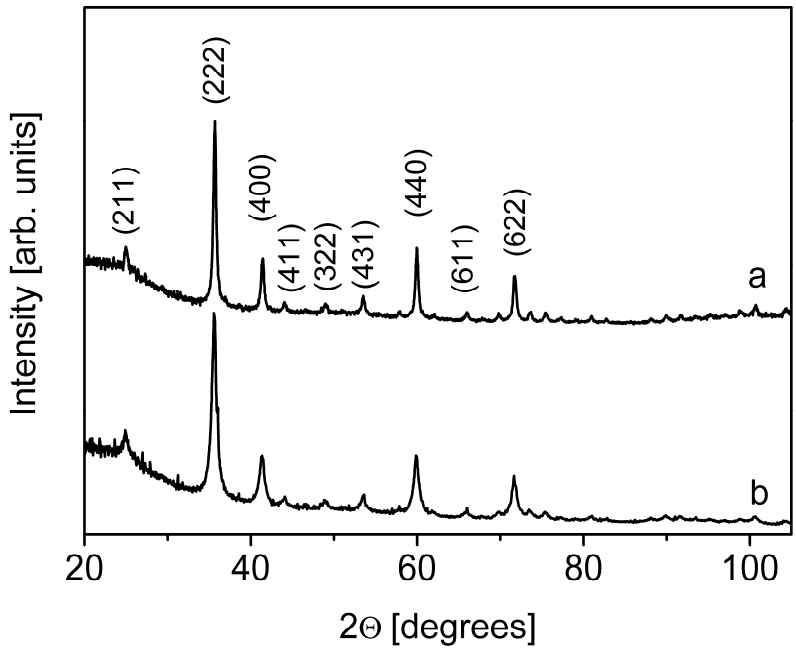

Figure 53. The XRD pattern of polycrystalline In_2O_3 nanotubes (a) and Q0D nanoparticles (b).

4.5.2.4 FTIR Study of In_2O_3 Q1D nanostructures and comparison with unmolded Q0D nanoparticles

The composition of nanotubes was also examined by means of infrared spectroscopy (Figure 54 a). The intense band around 419 cm^{-1} and three well resolved bands in

the range between 630 and 520 cm^{-1} have been attributed to the phonon vibrations of In_2O_3.[195, 196] The broad structureless absorption at 3600-3100 cm^{-1} corresponds to the O-H stretching vibration of crystal water, this band is assisted by small signals of in-plane deformation vibrations around 1350 cm^{-1} and around 1630 cm^{-1}.[197] This can be explained, as the surfaces of all oxides are covered by hydroxyl groups to variable degrees. Alternatively, the weak bands at 1630 and 1520 cm^{-1} can be assigned to the stretching mode of the conjugated double carbon-carbon bonds and indicate a minor content of underdecomposed organic fragments (e.g. ligands of the precursor or undissolved traces of polycarbonate templates). When compared to the spectrum of unformed In_2O_3 Q0D particles (Figure 54 b), nanotubes have noticeably higher content of hydroxyl groups. This suggests a more developed hydroxylated surface of the tubes. The intensity of the band at 1630 cm^{-1} in the Q0D particles sample is decreased along with the signal at 3600-3100 cm^{-1}, thus, the assignment of this absorption to crystal water seems to be more reliable than to carbonic residues.

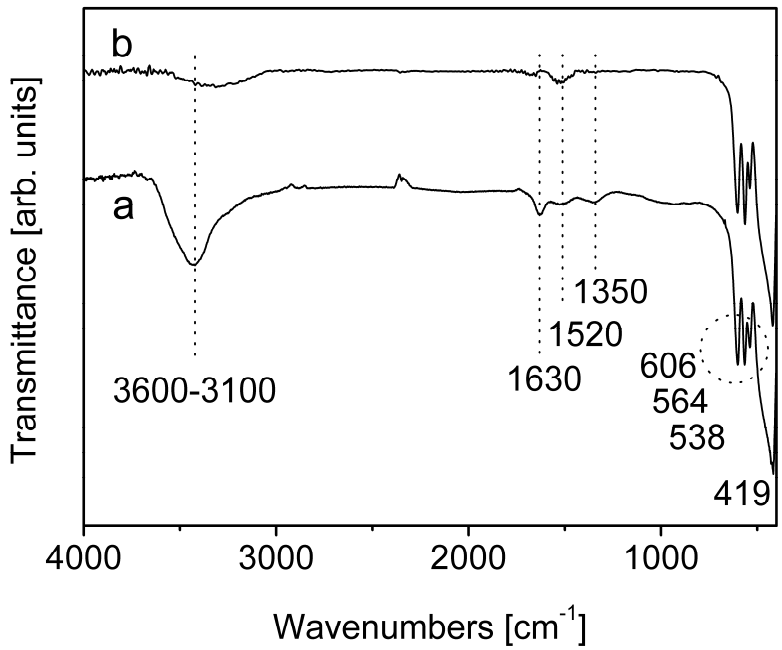

Figure 54. Infrared spectrum of indium oxide nanotubes (a) and unmolded indium oxide Q0D nanoparticles (b) derived from the same precursor at 350 °C.

4.5.3 Sensor tests

The sensing layers were fabricated by dropping suspensions of as-synthesized materials onto the alumina substrates provided by parallel Pt-electrodes on the front side and Pt-heater on the back side (see Fig. 55).

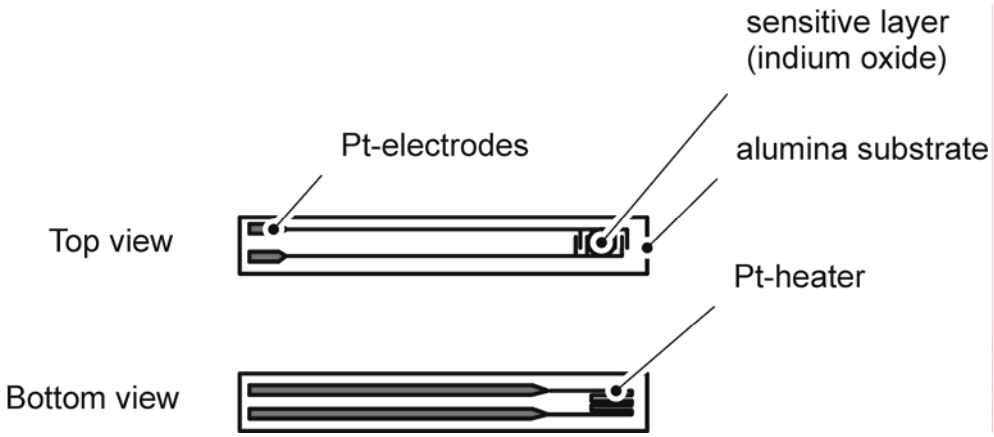

Figure 55. Layout of the planar alumina substrate with platinum electrodes and heater for sensor tests (modified from [111])

Figure 56 represents SEM visualisations of studied sensing layers obtained by ultrasonic disintegration of nanotube bundles (A) and unmolded Q0D particles (B) in ethanol and deposited on substrates for dc measurements.

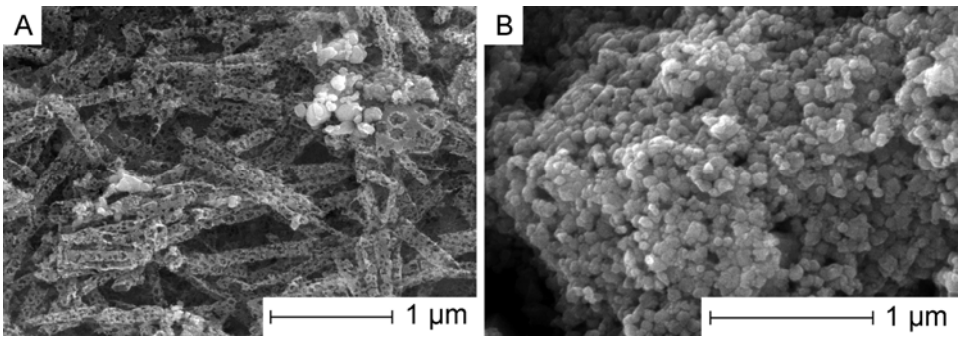

Figure 56. Comparison of sensing layers composed of highly porous nanotubes (A) and ultrasonicated Q0D In_2O_3 powder (B).

The morphology of highly porous divided nanotubes fully agrees with TEM images, as the sample preparation was identical. Unmolded In_2O_3 powders consisted of

agglomerates of spherical or polygonal Q0D nanoparticles of 40-150 nm size (can be defined as quasi zero dimensional, or Q0D particles). Polycrystalline nature of Q0D particles follows from significant broadening of maximal reflexes in powder XRD, and, therefore, a smaller crystallite size than observed in SEM.

It can be concluded from the sensor tests (Figure 57) that the templated nanotubes have significantly higher responses to small concentrations of gases than unmolded indium oxide in Q0D particles form derived from the same precursor.

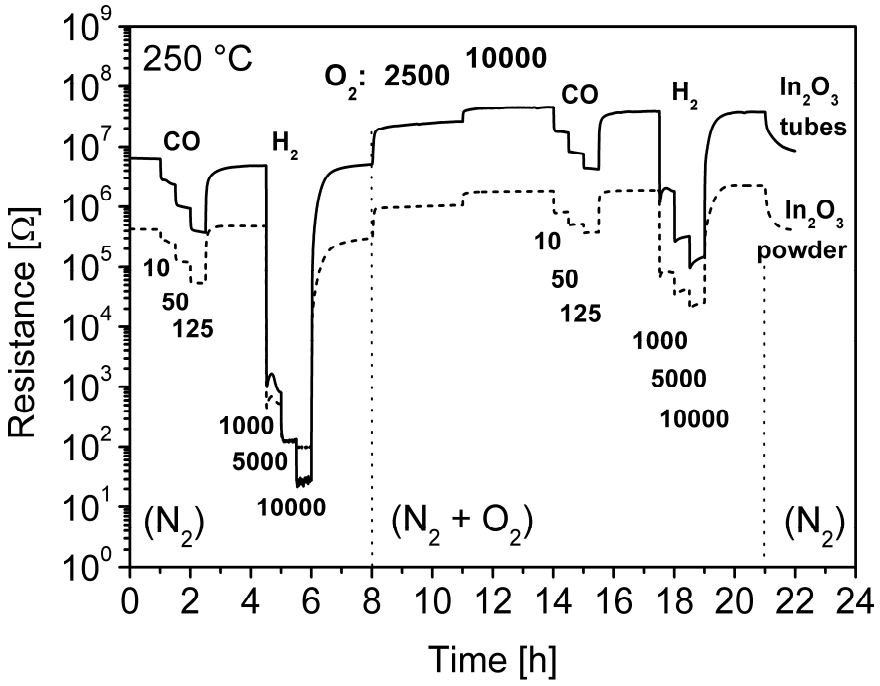

Figure 57. Transient response of unmolded In_2O_3 powder, composed of Q0D nanoparticles (dashed line) and In_2O_3 nanotubes (solid line) at 250 °C; concentrations of tests gases are given in ppm.

As pronounced n-type semiconductor, the material shows decrease in resistance upon exposure to electron donors, like CO or H_2, and increase in resistance in the presence of O_2. The resistance of the nanotubes sample before passing of hydrogen was around $5 \cdot 10^6$ Ohm, and dropped to ≈ 30 Ohm at 10000 ppm H_2. It decreases by factor of order of 10^5, whereas the resistance of unmolded In_2O_3 in Q0D particles form becomes ~10^3 times smaller under the same conditions. The second noticeable feature of the nanotubes is their shorter recovery time if compared to that of unmolded indium oxide. For example, for the H_2 detection in N_2 atmosphere, the baseline resistance of the nanotubes reached the initial value quicker than for one

hour, whereas the unformed counterpart did not fully recover during two hours. The comparison of the initial sample resistance and the final resistance after all sensor tests shows that all the interactions between the sensing layer and target gases are fully reversible, even in the absence of oxygen. The recovery of the baseline resistance is of crucial importance for any prospective gas sensing material.

Figures 58 and 59 present the resistances and the sensor signals to low CO (in the range from 10 to 125 ppm) and H_2 (from 1000 to 10000 ppm) concentrations at 250 °C in dry nitrogen and in the O_2 + N_2 mixture, as well as the response to oxygen during the stepwise switch from dry nitrogen to O_2 + N_2 (2500 ppm, 10000 ppm).

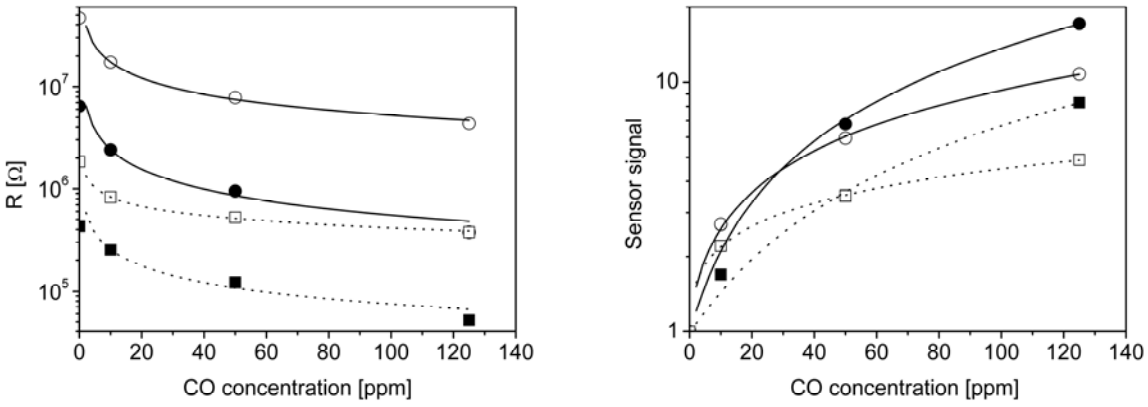

Figure 58. Resistances (left) and sensor signals (right) to CO in N_2 (● - nanotubes, ■ - Q0D particles) and in N_2 + O_2 mixture (○ – nanotubes, □ - Q0D particles). Solid fitting curves correspond to nanotubes and dotted - to powders.

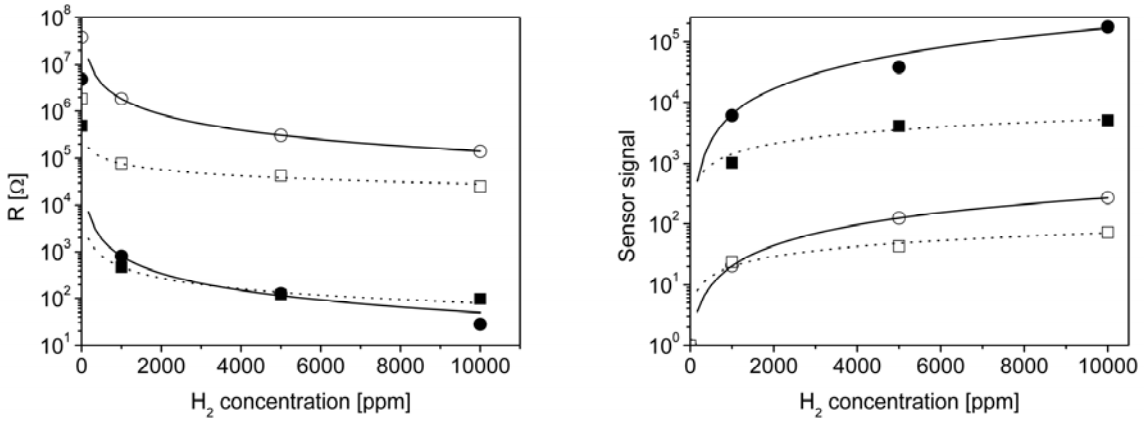

Figure 59. Resistances (left) and sensor signals (right) to H_2 in N_2 (● - nanotubes, ■ - Q0D particles) and in N_2 + O_2 mixture (○ – nanotubes, □ - Q0D particles). Solid fitting curves correspond to nanotubes and dotted - to powders.

The comparison of sensors based on the same material but with different morphology (nanotubes and umolded In_2O_3) clearly shows the better performance of templated tubular nanostructures. Nanotube sensors show high signal values at low CO concentrations (i.e. below 50 ppm), which is extremely important for many practical applications.

The resistance of sensors, *R*, is usually well correlated with the partial pressures of target gases *p* by empirical equations (1) and (2).

$$R \sim ap^b \quad (1)$$

or

$$\log R \sim a' + b \log p \quad (2)$$

where, *a*, a', and *b* are empirically found parameters.

The empirically found exponents are shown in the Table 4 together with those resulted from theoretical modelling.[198, 199] The exponents *b* have been reported to be rather specific; they can inform to some extend about the detection and conduction mechanisms in the sensing layers.

In our case,

- for polycrystalline nanotubes, the exponents *b* for the H_2 detection as well as for CO detection are practically equal in the presence and in the absence of oxygen. This points out at the same sensing / conduction mechanism in the presence and in the absence of oxygen;
- for Q0D particles, exponents *b* for the H_2 detection as well as for CO detection are ~ two times larger in the absence of oxygen if compared with those in the presence of oxygen. This points out at different sensing / conduction mechanism in the presence and in the absence of oxygen;
- for the H_2 detection as well as for CO detection the exponents *b* are larger for nanotubes if compared with those for Q0D particles; this difference is larger for H_2 detection. This finding indicates different sensing / conduction mechanism of H_2 /CO for the In_2O_3 in form of for polycrystalline nanotubes and for Q0D particles.

Table 4. Power law exponents of In_2O_3 sensing layers in forms of nanotubes and Q0D particles for various target gases.

Target gas/ Atmosphere	Experiment, this work		Model, ref.[198]		Model, ref.[199]
	nanotubes	Q0D particles	Value / reactive species[a]		Value/ Reactive species
			Large grains,[b] $r > \lambda_D$	Small grains,[b] $r \leq \lambda_D$	Simple gases[c]
CO/N_2	- 0.64 ± 0.08	- 0.53 ± 0.09	1.2 ...0.66 / O^-	0.5 /O^-	-0.5 /O^-
CO/O_2+N_2	- 0.52 ± 0.03	- 0.30 ± 0.02	0.6...0.36//O^{2-}	0.33 /O^{2-}	
H_2/N_2	- 1.22 ± 0.12	- 0.78 ± 0.09	-		
H_2/O_2+N_2	- 1.11 ± 0.01	-0.43 ± 0.07	-		

[a] - calculated for the conductance (*G*); for resistance they have the same numerical value but opposite sign

[b] - depends on the ratio between particle radius (*r*) and Debye screening length (λ_D), for details see [198]

[c] - a simple reducing gas like H_2 or CO deprives the oxide surface of one O^- ion per molecule; a complex gas reacts with plural O^- ions simultaneously, for details see [199]

Accordingly, there have been two main points to be clarified: (i) what exactly do large values of exponents *b* mean and (ii) why nanotubes are better if compared with Q0D particles? Firstly, larger exponents *b* mean higher sensitivity which is of importance for practical applications. Secondly, on the first sight, the data presented in the Table 1 show relatively good agreement between experimentally observed and theoretical values. For example, exponents *b* are practically equal for polycrystalline nanotubes and Q0D particles for sensor signals towards CO in nitrogen atmosphere and are in range 1.2-0.66. These values should be observed in porous granular sensing layers with single charged O^- ions mainly acting as reactive adsorbed oxygen species.[198, 199] However, this is only seeming similarity because both models are based on the interaction of target gas molecules with adsorbed oxygen species. The latter are to some extent “virtual”, i.e. despite trying for a long time, there is no convincing

spectroscopic evidence for their existence till now. Firstly, neither superoxide ion O_2^-, nor charged atomic oxygen O^-, nor peroxide ions O_2^{2-}, have been observed under real working conditions of sensors.[200] Secondly, the neutral dipolar oxygen species have been neglected in the aforementioned mechanistic descriptions; they are, however, active on sensing materials at operating temperatures of about 200 °C.[201, 202] Moreover, the assumption about adsorbed oxygen species as main active species is not valid for the measurements in nitrogen because neither molecular oxygen nor adsorbed oxygen species are present there.

Accordingly, the higher exponents for nanotubes cannot be explained by any of the models presented in the literature. However, the higher effects for H_2 may most likely point toward an effect originating from pore size-dependent diffusion of the gas molecules through the pores. An indication for this may be the high sensitivity to H_2 observed also for other nanotubes, like TiO_2,[203] which is more likely caused by the highly porous structure and may indicate Knudsen diffusion regime. Nevertheless, this issue remains to be further clarified.

4.6 Polycrystalline pure ZnO and Mn-doped ZnO nanorod arrays from single source oximato precursors

This section describes synthesis and characterisation of polycrystalline plain and Mn-doped zinc oxide nanorods from single source molecular precursors using track-etch polycarbonate films as templates. Investigation of Mn-doped samples by spectroscopic (XPS) and resonance (ESR) methods suggested that Mn has only oxidation state +II and is distributed in the volume and on the surface of ZnO nanocrystals.

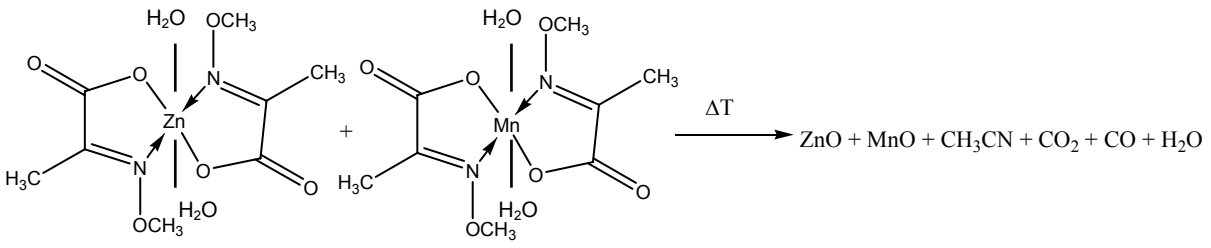

4.6.1 SEM study of ZnO nanorods

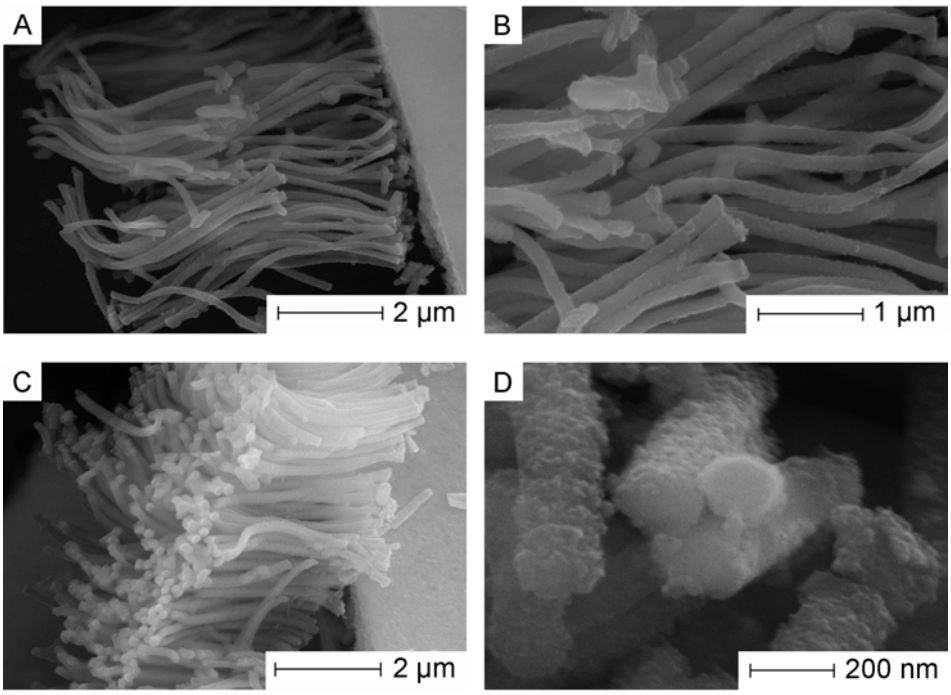

Figure 60. SEM images confirm the length of 5-6 µm and the uniform diameter of the nanorods (A, B), large blocks with parallel alignment (C); the diameter is around 170-180 nm.

The thickness of nanorods from polycarbonate membranes with 0.1 µm nominal channel diameter after thermal conversion and removal of the polymeric template with CH_2Cl_2 was about 170-180 nm. The length of the rods was 5-6 µm and corresponded to the length of template channels. It is evident from the cross-sections where the rods were broken that there is no hollow tubes formation. The rods are composed from smaller particles and obviously have a polycrystalline porous nature. A very thin flat layer uniting the rods, which originates from the precursor on the template surface, was sometimes observed as well.

Filling of smaller template pores (nominal size 0.03 µm) resulted in thinner nanowires of a diameter approximately 60-70 nm. However, a larger aspect ratio makes the nanowires extremely flexible, unstable and inclined to breaking into small pieces and to aggregation of single wires into tight webs. This instability made the study of such nanorods with TEM impossible because of complete destruction during the sample preparation in an ultrasonic bath.

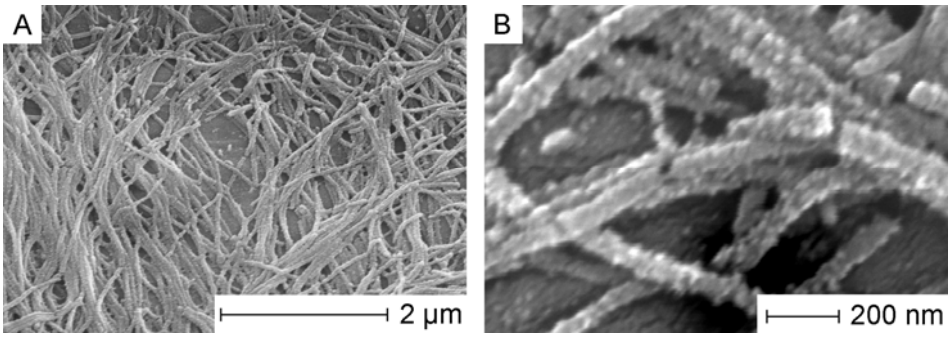

Figure 61. SEM images demonstrate the flexibility of nanorods with a decreased diameter and increased aspect ratio.

4.6.2 EDX analysis of ZnO nanorods

Fig. 62 presents the EDX spectrum of nanorods from templates with 0.1 µm nominal pore size.

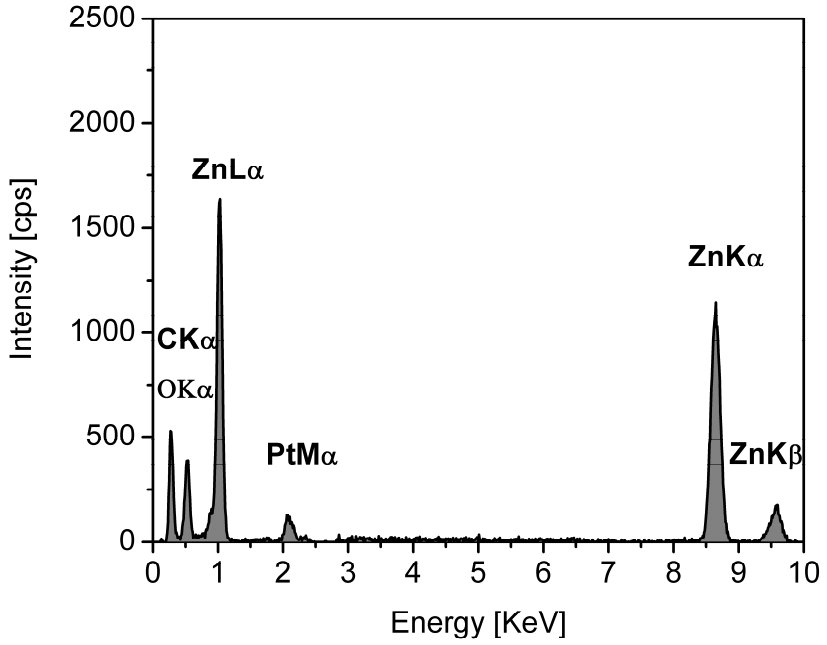

Figure 62. EDX spectrum of plain ZnO nanorods.

Only signals from zinc, oxygen, carbon (caused by adhesive carbon-reach conductive polymeric film on the sample holder), and platinum (4 nm thick sputter layer against sample charging) are found. According to the semi-quantitative analysis,

the atomic ratio of Zn to O varied in the range from 1:1 to 1:2 for different samples. The reason for this is very likely the slow reaction of ZnO with air moisture and formation of hydroxide layer on its surface. This reaction is very likely promoted by a high surface-to-volume ratio and, thus, a large accessible surface of the porous nanorods.

4.6.3 TEM and SAED investigation of ZnO nanorods

As seen from Fig. 63, polycrystalline rods from 0.1 µm templates tend to collapse in an ultrasonic bath during TEM samples preparation. The residual nanorods are clearly seen in the images and confirm compact agglomerated morphology without hollow tubes formation, but they are surrounded by flock-like aggregates of ZnO nanoparticles from destroyed Q1D structures. At a higher magnification, the polycrystalline nature of the material is visible (Fig. 63 C). A rod is composed of randomly oriented irregular particles of sub-5 nm size, and this composition is also confirmed by very diffuse rings in SAED pattern (Fig. 63 D).

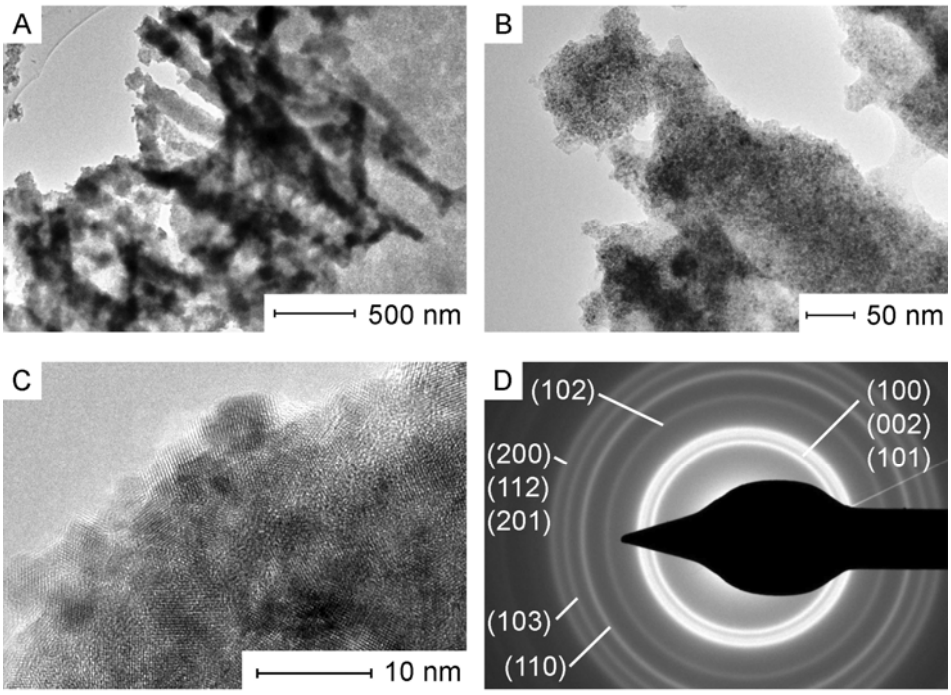

Figure 63. TEM images of the ZnO nanorods after the treatment in an ultrasonic bath, confirming the solid Q1D morphology (A, B) and a polycrystalline nature (C), the latter is also confirmed in SAED pattern (D).

This small size of the composing units is a very important fact during the investigation of optical properties of the material. ZnO nanocrystals with diameters smaller than 7 nm are already considered in the literature as affected by quantum confinement effects.[204] For instance, the variation of the band gap is size-dependent below a diameter of 7 nm.[205]

4.6.4 XRD study of ZnO nanorods of various diameters and powders derived from a single source oximato precursor

Comparison of XRD patterns of ZnO powder and two types of templated nanorods under study is shown in Fig. 64.

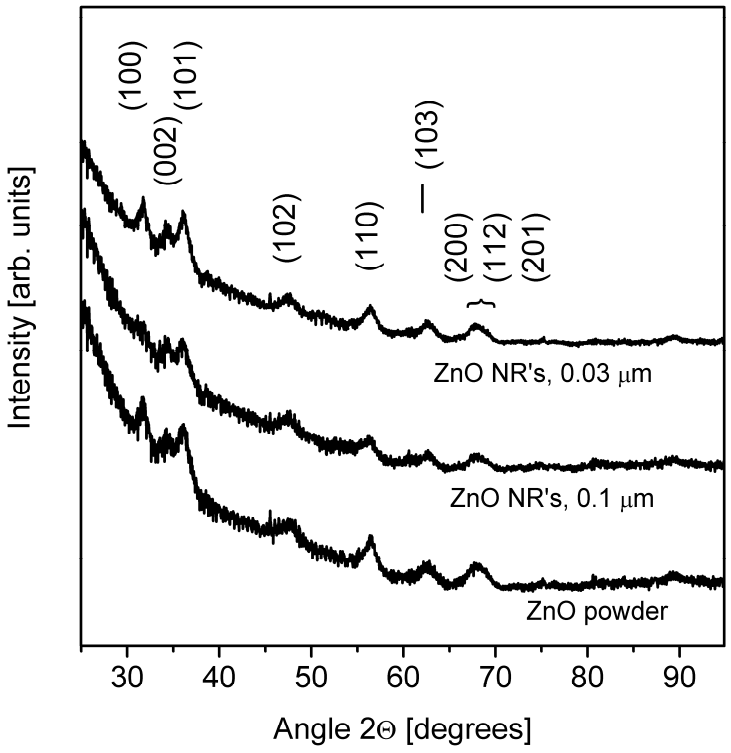

Figure 64. XRD patterns of unmolded ZnO powder and nanorods obtained from 0.1 and 0.03 μm pores.

The reflexes correspond to hexagonal wurtzite structure. All the diffractograms are characterised by a high level of noise and very broad illegible reflexes. These effects are due to the small sub-5 nm crystallite sizes and a strong influence of

inhomogeneous strains. On account of these inhomogeneous strains, as well as a strong diffractometer-generated baseline curvature under the most intensive (101) reflex, the application of Scherrer equation and correct estimation of the average crystallite size from reflexes broadening is difficult. However, it is important to note that the reflexes width in nanorods spectra is practically identical with that of unmolded powder spectra. This means that the size of composing ZnO nanocrystals did not change after the moulding procedure.

4.6.5 Raman spectroscopy of ZnO nanorods and powder derived from zinc oximato precursor

Raman spectra of ZnO powders and templated nanorods are shown in Fig. 65.

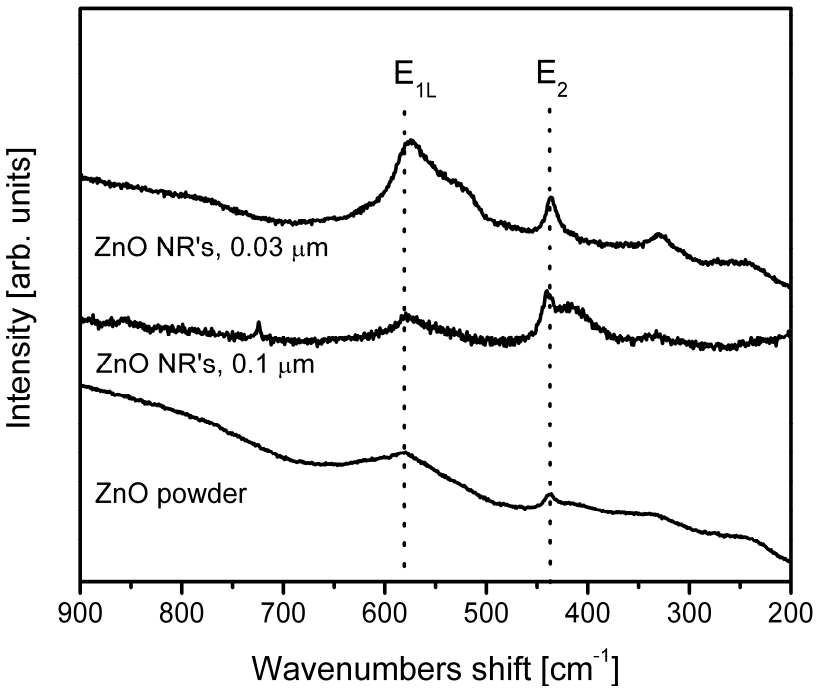

Figure 65. Raman spectra of ZnO powder from oximato precursor and templated nanorods.

All the spectra are characterised by two most intensive broad assymetric peaks at 437 and 580 cm^{-1}. The active Raman peak at 436 cm^{-1} (marked in the spectrum as E_2 mode of ZnO) is characteristic for wurtzite hexagonal phase, whereas the E_{1L} mode at 583 cm^{-1} corresponds to impurities and structural defects, oxygen vacancies

and Zn interstitials.[206] Another distinctive feature of all three spectra is the broadened assymetry of the peak at 436 cm^{-1}, this 'shoulder' is particularly prominent in the spectrum of nanorods from templates with 0.1 μm nominal pore size. This feature of the peak at 436 cm^{-1} is described in the previous works as typical for ZnO Raman active branches, which is also characteristic for nanoscale ZnO particles.[144] All three spectra also show a lower intensity mode located at around 330 cm^{-1}, which was previously observed at 332 cm^{-1} for pure ZnO nanorods made by diffusion method.[141]

4.6.6 PL spectroscopy of ZnO nanorods

PL spectra excited at 350 nm are demonstrated in Fig. 66. It is seen for nanorod samples that the near-band emission around 380-390 nm due to the recombination of bound excitons[147] is totally absent. This situation is commonly known for small (starting with 10 nm and smaller) ZnO nanocrystals[207] and confirms the agglomerated multiparticulate morphology of the rods. The broad intensive PL signal at 470-650 nm is the combination of green (around 520 nm) and orange (600 nm) emission generated from defects like oxygen vacancies, interstitial oxygen atoms, or other lattice imperfections related to zinc or oxygen vacancies.[206] In both the cases of the nanorods under study, green emission with the maximum at 500-520 nm prevails, which can suggest slightly oxygen deficient character of the samples.

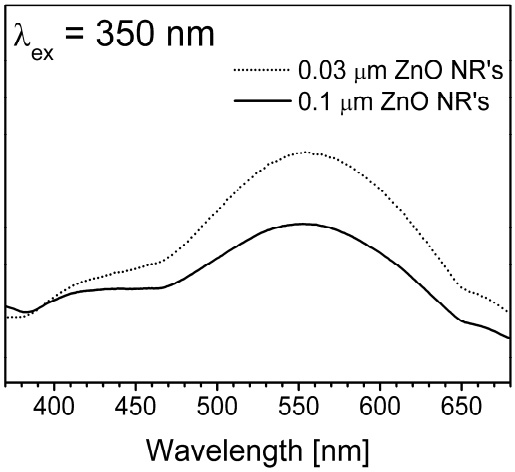

Figure 66. Photoluminescent spectra of nanorods from 0.1 and 0.03 μm pores.

4.6.7 ESR study of ZnO nanorods and Q0D nanoparticles from the precursor Di-aqua-bis[2-(methoxyimino)propanoato]zinc

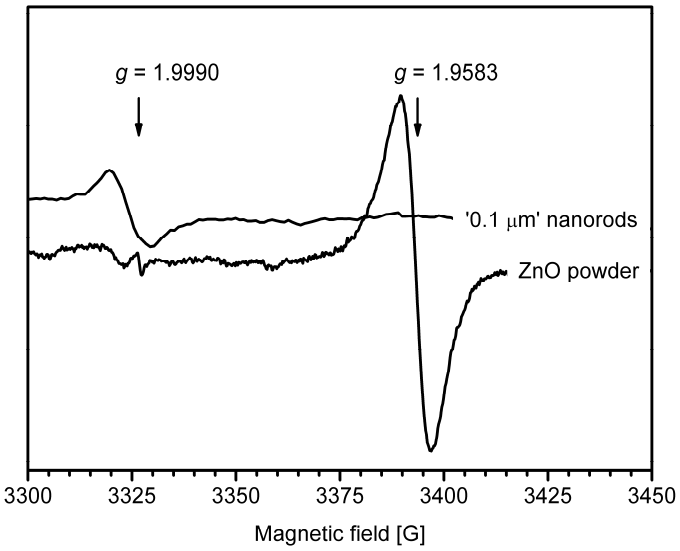

Figure 67. ESR spectra of ZnO powder and '0.1 μm' nanorods, both synthesised at 160 °C from the same oximato precursor, T = 293 K, X-band (9.3 GHz).

ESR spectra of ZnO powder (Q0D nanoparticles) and of moulded ZnO nanorods obtained from 0.1 μm nominal size pores are presented in Fig. 67. In the spectrum of powder, the broad line with $g \approx 1.96$ is predominant. This signal is common for ZnO ceramics and powders and is assigned to ionized oxygen vacancies in the bulk of crystallites.[208, 209] For the nanorod spectrum, this signal is diminished, but another one at the low-field side becomes prevailing. This line is ascribed to absorbed O^{2-} or CO_3^{2-} ions on the surface of ZnO particles, thus, this signal with characteristic *g* value around 2.0 suggests the increase of accessible surface when switching to Q1D structures. Previously, this signal with the *g*-factor value of 2.003 was reported for fine ZnO powders (grain size 50-80 nm).[210]

4.6.8 Analysis of Mn-doped ZnO nanorods

4.6.8.1 XPS study

To determine the oxidation state of implanted Mn ions, XPS spectra were taken from species with 0.1 and 5 wt.-% doping concentration. If Al *Kα* radiation is applied to the

samples, Zn *LMM* Auger-peaks appear in the spectrum exactly in the same energy region where the Mn 2*p* signal is (See Fig. 69, below). In this connection, Mg *Kα* radiation, which is free from this drawback, was used instead.

Fig. 68 presents survey spectra of the nanorod samples before and after Ar^+ ions sputtering. It is evident from the comparison (see also inset in Fig. 68), that the C 1*s* peak is completely removed after sputtering. This suggests that the species are free from any carbon-containing traces, *e.g.* incompletely decomposed precursors, and only negligible amounts of organic substances were absorbed on the surface. In other respects, only zinc and oxygen peaks are prominent, and no other undesirable impurities were found.

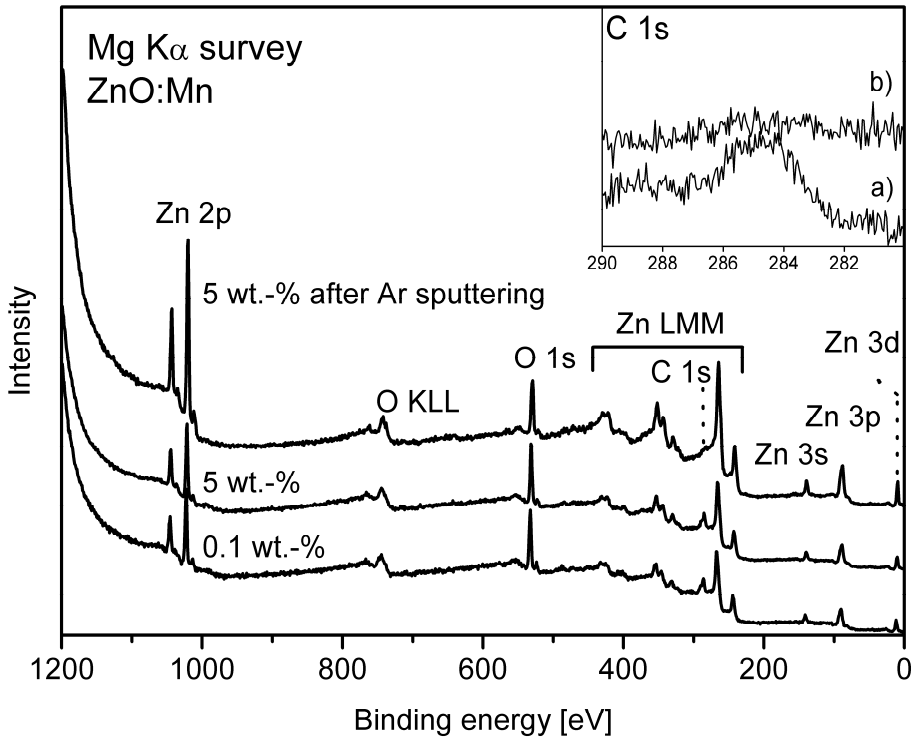

Figure 68. Survey XPS spectra of ZnO:Mn samples before (see also inset, a)) and after (inset, b)) Ar sputtering.

The slow scan of Mn 2*p* level of the sample with 5 wt.-% doping content is shown in Fig. 69 (above). It shows the typical for Mn(II) combination of Mn $2p_{1/2}$ and Mn $2p_{3/2}$ signals and two satellites at equal distances of less than 5.5 eV from the corresponding main peaks. It is known that the satellites of Mn^{2+} are located at

around 6 eV from the signals, while the satellites of Mn^{3+}/Mn^{4+} are approximately 10 eV away.

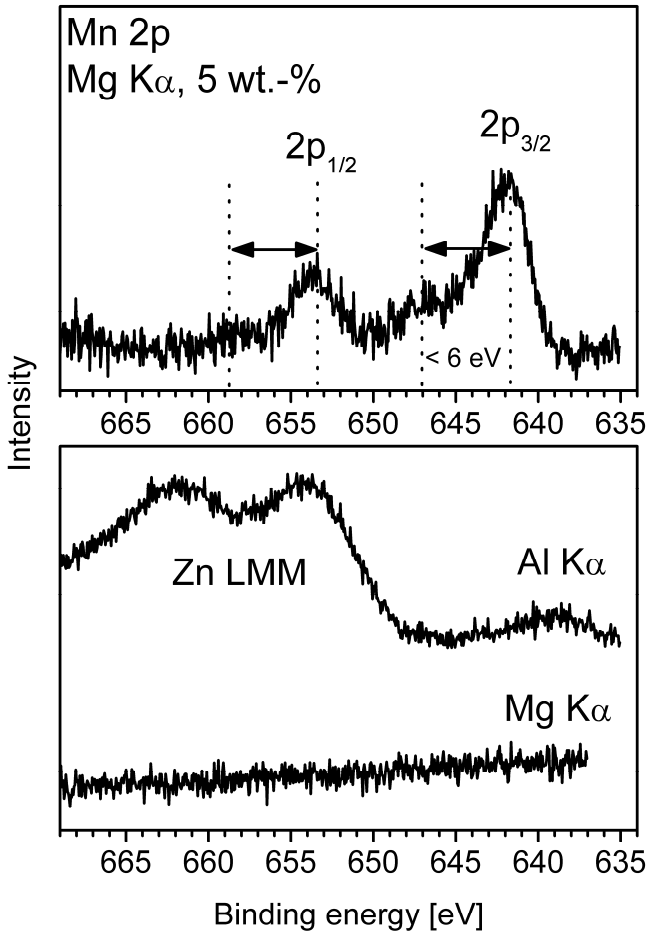

Figure 69. Slow scan of Mn 2*p* level of the 5 wt.-%ZnO:Mn sample and demonstration of Zn *LMM* Auger-peaks appearance when switching from Mg *Kα* to Al *Kα* radiation.

If oxidation states different to Mn(II) were found in the sample, the satellite of Mn $2p_{3/2}$ would be masked under the $2p_{1/2}$ peak, and the satellite of the Mn $2p_{1/2}$ signal would appear around 663-667 eV.[211] Instead of this, no satellite in this energy region is observed. Thus, only oxidation state (II) can be ascribed to Mn ions in the samples.

4.6.8.2 FTIR study

Doping of ZnO samples with manganese ions also resulted in some noticeable changes in FTIR spectra. As known from the literature sources, spherical ZnO

nanoparticles have a broad absorption at 460 cm^{-1}, and nanorods show two bands located at 377 and 506 cm^{-1} (the band is split when switching from spheres to cylindrical units).[140] In case with ZnO:Mn^{2+} doped systems, the ZnO absorption profile line is sharper. FTIR spectra of Mn_3O_4 show two bands at 609 and 495 cm^{-1} associated with the coupling between Mn-O stretching modes of tetrahedral and octahedral sites, thus, it is also possible to make conclusions about separate Mn^{2+} or Mn^{3+}-related phases formation.[212]

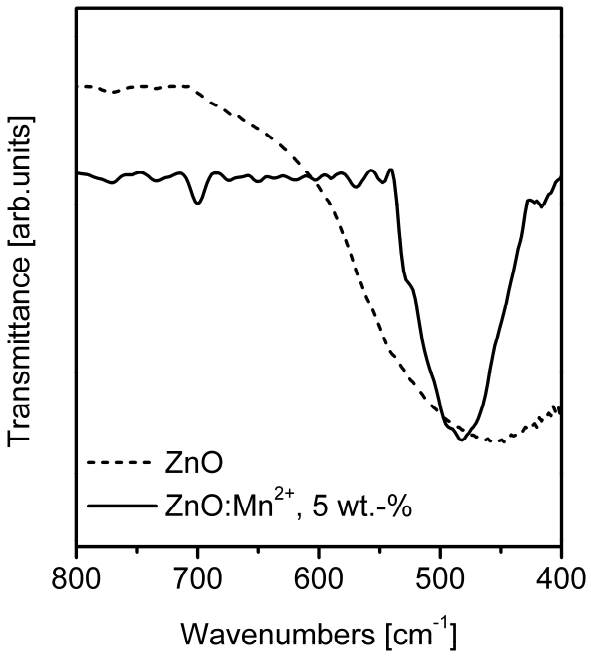

Figure 70. Comparison of FTIR spectra of plain ZnO and 5 wt.-% ZnO:Mn nanorods.

As seen from the spectrum in Fig. 70, a 5 wt.-% manganese doped sample has significantly narrower absorption in the region between 700 and 400 cm^{-1}, located at 486 cm^{-1} instead of 455 cm^{-1} for plain ZnO rods. The position of single broad zinc oxide band confirms that the rods are composed of spherical particles. The absorption profile sharpening in ZnO:Mn^{2+} spectrum is due to the Mn^{2+} ions implantation. At the same time, there are no additional signals at 609 cm^{-1}, which may be interpreted as a complete doping dissolution in ZnO matrix.

4.6.8.3 ESR study of ZnO:Mn

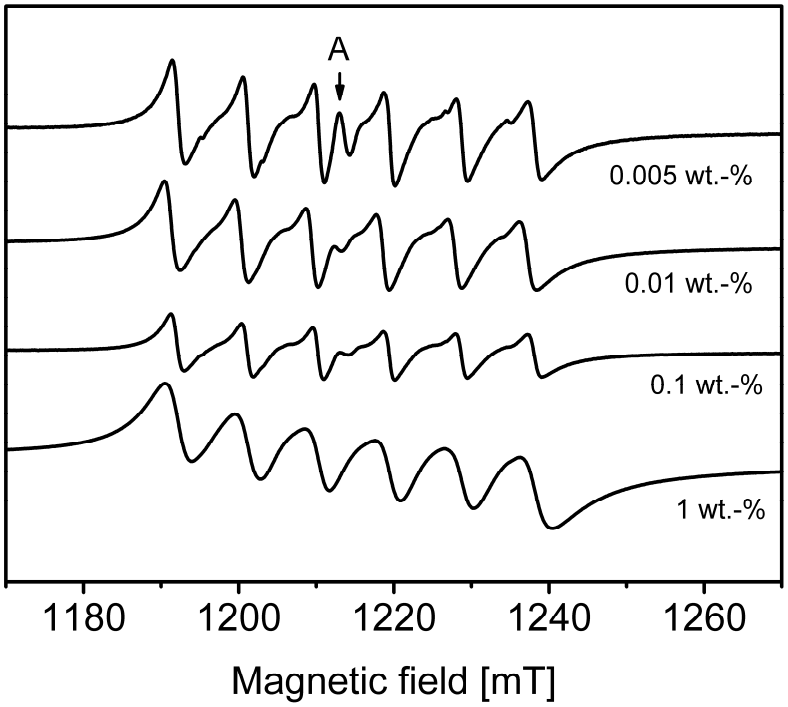

Figure 71. ESR spectra of ZnO samples doped with Mn in different proportions, T = 293 K, Q-band (34 GHz).

From the analysis of ESR spectra of the samples with 1 wt.-%, 0.1 wt.-%, 0.01 wt.-%, and 0.005 wt.-% doping levels, certain dependence between concentrations and structure can be noted. The 1 wt.-% spectra is characterised by a large baseline distortion, as well as a significant line broadening in the resolved hyperfine structure signal of Mn^{2+} ions. Analysing the line broadening character, it may be said that they are widened asymmetrically, which is typical for superposition of several signals. A strong baseline distortion can be related to the presence of a broad signal from Mn^{2+} ions with unresolved hyperfine structure in the spectrum. Thus, generation of several paramagnetic forms, which are the Mn^{2+} ions with different surroundings, may be claimed for the 1 wt.-% sample spectrum because of a high manganese concentration. Presumably, for this concentration, manganese ions are presented in the sample as both the adsorbed on ZnO surface cluster-like formations with strong

ion-ion interactions, leading to the line widening right up to the hyperfine structure disappearance, and the Mn^{2+} ions incorporated into the diamagnetic ZnO matrix. Besides that, the presence of Mn^{2+} ions bound up with the surface centres on the diamagnetic substrate (ZnO), which are distant from each other, is possible. The signal superposition of this ensemble of Mn^{2+} ions with non-equivalent surroundings can be suggested for the observed widened but still resolved hyperfine structure.

As the manganese concentration in studied samples decreases, the tendency to narrowing and individualization of ESR signals of manganese ions is visible. For example, at the 0.1 wt.-% concentration, the signal with unresolved hyperfine structure is practically absent and the bend of baseline also disappears. This is very likely due to the insufficient amount of manganese in the sample to build up associated cluster-like formations on the surface or in the pores of the diamagnetic substrate. At the same time, a series of lines of a weaker intensity starts to appear in the 0.1 wt.-% sample. The maximal narrowing and symmetrisation of hyperfine structure lines in the ESR spectrum, as well as more prominent development of weaker lines between the main components of the signal, is observed as the manganese concentration in the sample reaches 0.005 wt.-%. As known,[213] the presence of less intensive lines between the main components of a Mn^{2+} ESR spectrum is due to the possibility of forbidden transitions with simultaneous change of electron and nucleus spins by ±1. In high-spin systems with d^5 configuration (like Mn^{2+} ions), such transitions take place in case with a distorted tetrahedral field, i.e. by breaking of a cubic symmetry and decrease of the symmetry axis order value. Thus, the appearance of lines from forbidden transitions is the evidence of the incorporation of Mn^{2+} ions into the structure of diamagnetic ZnO matrix, whose symmetry strongly differs from cubic. The degree of distinction of the field from cubic can be evaluated only qualitatively, but, taking into account that the forbidden transition signals intensities are comparable with the basic spectrum lines, it is possible to say that the Mn^{2+} experiences the effect of a strongly distorted field of ligands with respect to that of tetrahedron. The degree of tetrahedral field distortion can be also evaluated from the g-factor value.[214] According to literature data, g-factor of Mn^{2+} ions in the distorted tetrahedral field of weak ligands, among which ZnO can be also considered, is 2.0016.[213, 215, 216] This g-factor value was obtained for samples synthesised by means of high-temperature diffusion of Mn^{2+} into zinc oxide. For a matrix that provides a non-distorted field with cubic symmetry, like MgO, g-factor of Mn^{2+} ions

2.008.[213, 217] In our case, the g-factor is 2.0012. Thus, incorporated into the diamagnetic zinc oxide matrix Mn^{2+} ions are in rather distorted tetrahedral field, which does not have a 4-fold symmetry axis. At the same time, the degree of distortion is slightly less than in samples obtained by means of high-temperature diffusion. Possibly, we are dealing with a tetrahedron, distorted up to trigonal symmetry, which is characterised by the 3-fold symmetry axis. The internal standard line A in the middle of the spectrum has g-factor close to 2.0036, which is typical for an electron stabilized on carbon in free radical compounds.

Similar results have been reported previously for ESR study of Mn doped ZnO nanostructures.[140] There were two contributions observed below 1.0 % Mn doping concentration: a broad resonance from antiferromagnetic Mn^{2+} interactions and sextuplet from isolated spins. Generally speaking, six hyperfine components with 90-110 G splitting are usually observed in case with isolated paramagnetic Mn^{2+} ions.[212]

4.7 Cu-doped ZnO nanorods from the single source oximato precursors Bis[2-(methoxyimino)propanoato]zinc and Bis[2-(methoxyimino)propanoato]copper

This section deals with the synthesis of polycrystalline nanorods aggregated of Cu-doped ZnO nanoparticles with the help of organic polymer templates. Familiar from literature and well studied zinc and copper ketoacidooximates have been employed as precursors.

4.7.1 Preliminary TGA study of the precursor composition

Individual Cu and Zn oximato complexes are known from previous publications to form pure crystalline metal oxides at temperatures not exceeding 160-180 °C.[205, 218] Preliminary thermogravimetric investigations were carried out to clarify the conversion temperature of the co-evaporated dry mixture of two oximates with the expectation of 5 wt.-% CuO-doped ZnO.

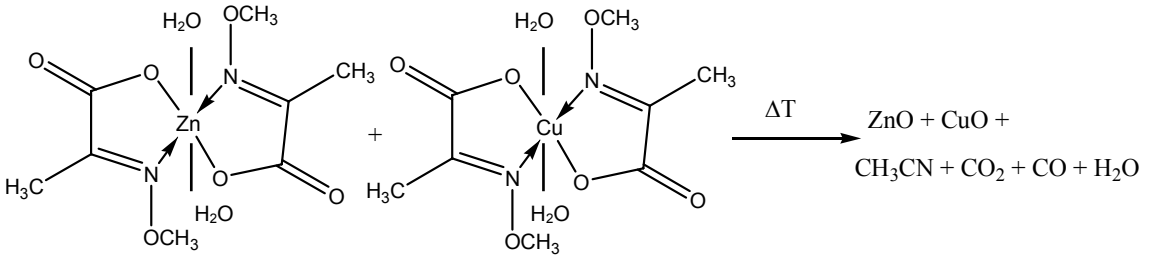

The thermogravimetric curve (Fig. 72) shows three events, which are over at approximately 270, 350 and 450 °C. This result suggests that the mixed system has to be sintered at elevated temperatures in comparison with pure oximato complexes to yield a final steady mass inorganic residue. In all further experiments, the 'green body' nanorods were converted at 450 °C. However, the evolution of the system at all three decomposition stages suggested by TGA was investigated by XRD and FTIR for a better understanding of the material's quality.

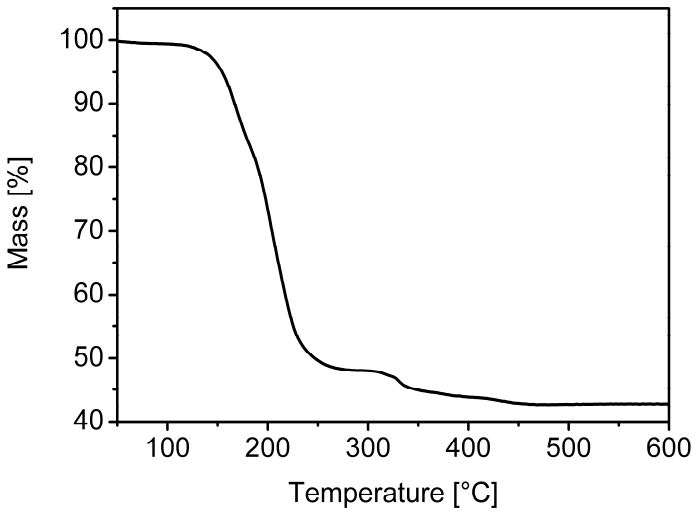

Figure 72. TGA analysis of co-precipitated zinc and copper containing precursors taken in ratio with the expectation of 5 wt.-% CuO-doped ZnO after complete thermal decomposition.

4.7.2 SEM study of 'green body' and Cu-doped ZnO Q1D structures

Fig. 73 demonstrates ‚green body' nanorods arrays after infiltration of a precursor solution, drying, solidification at 180 °C and following removal of the polymeric template with CH_2Cl_2. The diameter of these parent structures was around 100 nm. The length of the rods was around 5 µm and exactly replicated the template channels

in this respect. Nanorods were arranged in arrays (order of several hundreds square micrometers) parallel to each other. A thin flat layer uniting the rods from one side of the array, which originates from the precursor on the template surface, was also sometimes observed.

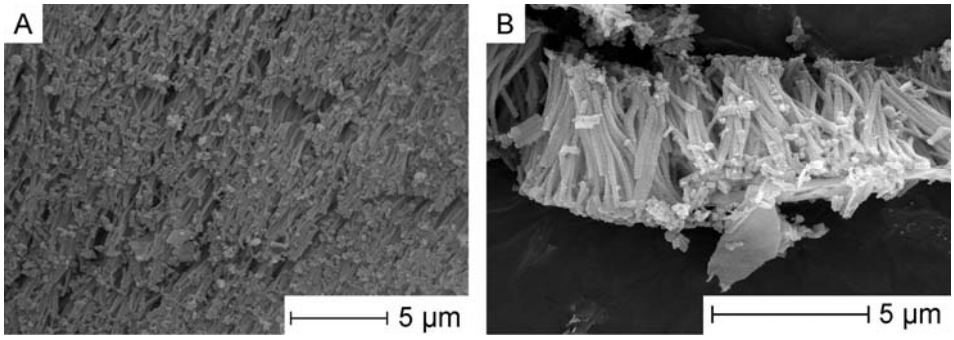

Figure 73. SEM images of the molded precursor array dehydrated at 180 °C and isolated from the polymeric template; image (A) shows a good yield of the nanorods of the uniform length; (B) 'green body' nanorods have the length of 5 µm and replicate the nanochannels in porous polycarbonate templates.

The length of the ZnO:Cu rods after calcination in the air at 450 °C can be estimated from SEM images obtained (Fig. 74) as approximately 3-5 µm, the diameter varied in the range 70-150 nm. The presented in Fig. 74 example images were taken from 5 wt.-% doped samples. Nanorods with lower dopant concentrations showed in SEM analogous morphology. The reason for slight length decrease might be deformation and shrinkage of the parent material during the thermal treatment.

At a higher magnification, the particulate morphology of the nanorod is clearly visible (Fig. 74 B). The roughly estimated from high resolution SEM images size of the grains is about 15-25 nm.

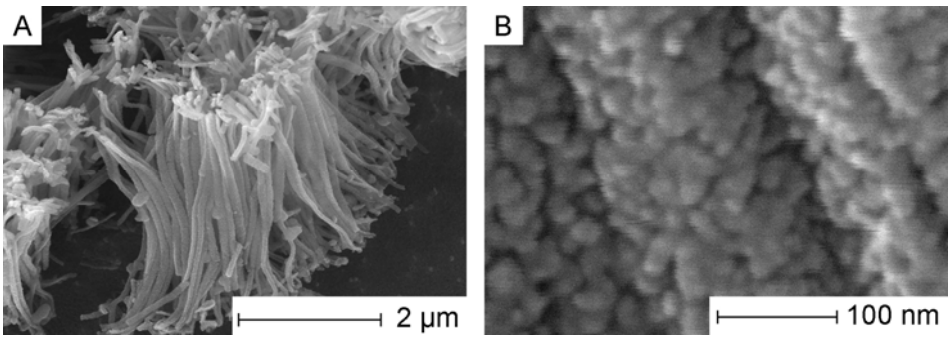

Figure 74. SEM images of the polycrystalline nanorods after calcination at 450 °C.

4.7.3 EDX analysis of Cu-doped ZnO nanorods

The result of the energy-dispersive X-ray analysis (EDX) of the rods with 5 wt.-% nominal doping level is presented in Fig. 75. The only signals present in the spectrum belong to Zn, O, Cu and C, but the contribution of carbon-reach conductive polymer film used for sample preparation has to be taken into account as well. According to the standardless quantification method, the compound contains 5.5 wt.-% of Cu (the instrumental error is around 1 wt.-%, the CuO doping level of 5 wt.-% corresponds to 4 wt.-% of Cu). This result indicates that the concentration of the implanted Cu dopant is reasonably good controlled with the used synthesis method.

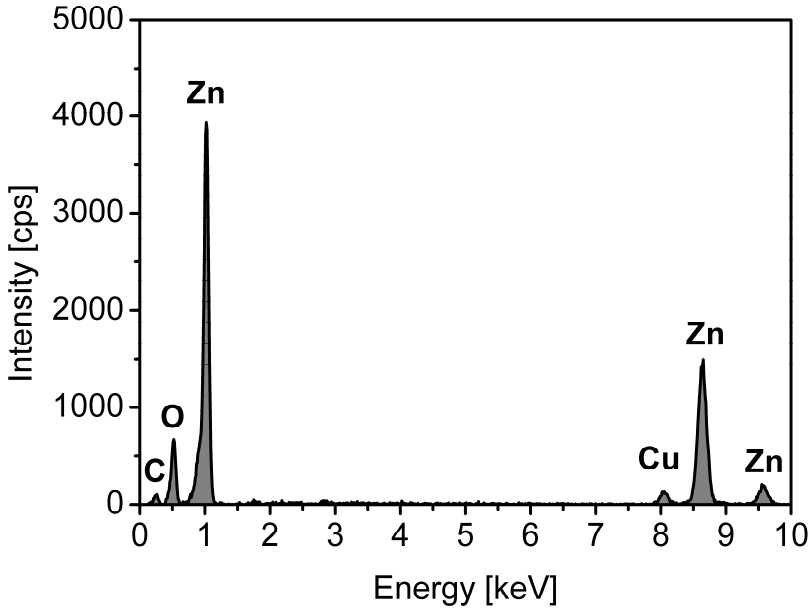

Figure 75. The EDX spectrum of the rods with 5 wt.-% nominal doping level.

4.7.4 TEM and SAED study of Cu-doped ZnO nanorods

High resolution TEM images (Fig. 76 A) confirm the parallel arrangement of the rods seen in SEM. The diameter of a single rod averages 90-95 nm.

At a higher magnification, the polycrystalline nature of the material is visible. A rod is composed of smaller randomly oriented irregular particles, the size of particles varied in the range around 8-21 nm. These values slightly deviate towards smaller grain sizes, but are still in a good agreement with those estimated from SEM micrographs.

The resolution of the obtained TEM images involves some difficulties for direct interplanar spacing estimation. However, the image enlargement effect of periodic structures with the help of so-called Moiré effect can be applied.

If two periodic structures with a period *d* overlap, the formation of Moiré fringes is observed. When one of two superposed identical crystal lattices is rotated relative to another at an angle *φ*, a rotation Moiré with the period

$$D_{rot} = d/\varphi$$

appears. The resulting period in the Moiré pattern can be several times larger as compared to the interplanar spacing of the lattice *d*. Thus, the lattice parameters can be found more precisely.

Fig. 76 C duplicates Fig. 76 B with artificially increased contrast and schematically clarifies the procedure of lattice period estimation.

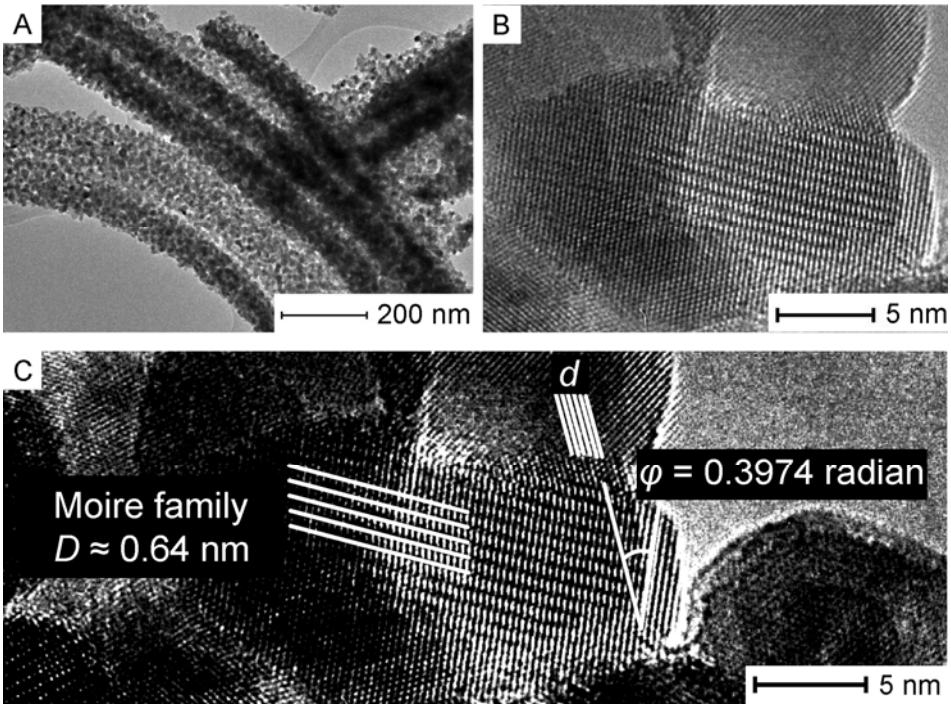

Figure 76. HRTEM images of the resulting polycrystalline nanorods confirm their parallel arrangement (A), show the composing nanocrystals size in the range approximately between 8 and 21 nm (B), and clarify the interplanar spacing calculation procedure (C).

As it is seen from Fig. 76 B and Fig. 76 C, two crystallites overlap with the formation of a Moiré pattern. The planes of one crystallite are seen well (on the right side of the demonstrated angle φ); the planes of another one are continued with white sketch lines (above the angle φ) to show their orientation more clearly in the picture. The angle between two plane families φ is 22.77° (the angle and distances were measured in the picture with *ImageJ* processing and analysis software), or 0.3974 radian. The average period of the Moiré pattern D_{rot} is within the limits of 0.64 nm. Now, if we use the found values in the equation, the interplanar spacing of the lattice gives 0.254 nm.

As is well known, the interplanar spacing of 0.258 nm corresponds to (002) plane of ZnO.[219] The experimentally found tendency to the uniform decrease of the lattice spacing by approximately 1.55 % is likely due to the difference in radii of octahedral coordinated Cu^{2+} (0.057 nm) and Zn^{2+} (0.060 nm) cations, and suggests existence of Cu_{Zn} in doped ZnO lattice, or, in other words, the formation of a substitutional solid solution.

The composition of nanorods from smaller randomly oriented irregular particles is also confirmed by diffuse rings in SAED pattern (Fig. 77). The image is fully consistent with the XRD results below in the text.

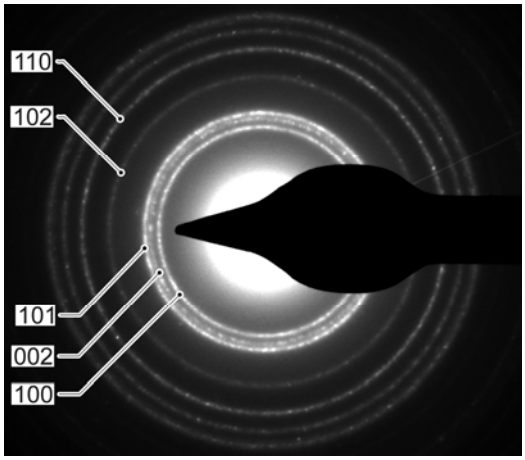

Figure 77. SAED pattern of the polycrystalline ZnO:CuO nanorods with 5 wt.-% doping level.

4.7.5 XRD study of ZnO:Cu with different doping levels calcined at various temperatures

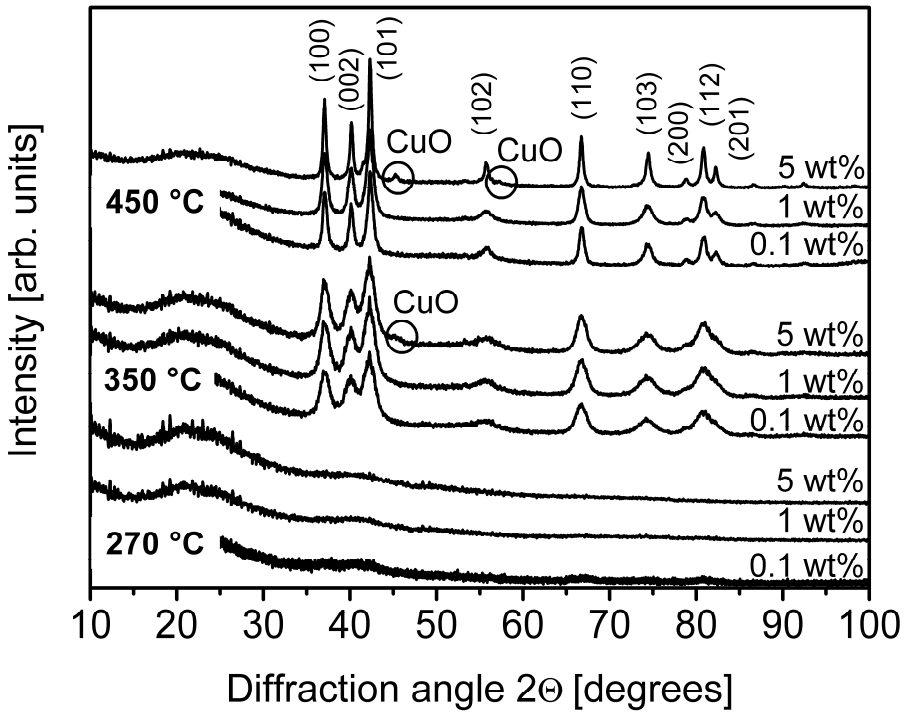

Figure 78. XRD spectra, following the structural changes in ZnO:CuO samples with various doping levels processed at different temperatures.

Structural properties of the samples doped with 0.1 wt.-%, 1 wt.-%, and 5 wt.-% CuO and calcined at temperatures in the range between 270 and 450 °C in air were also examined by means of powder X-Ray diffractometry (XRD) (Figure 78).

All three samples calcined at 270°C are amorphous, but very small features of ZnO crystals nucleation are visible. At 350°C, only hexagonal wurtzite structure pattern of ZnO (JCPDS file 36-1451) with a large reflex broadening was observed in samples with 0.1 wt.-% and 1 wt.-% CuO impurity content. A very low intensity signal corresponding to separate CuO phase can be also found in the 5 wt.-% sample. It is unfortunately not clear whether the appearance of this signal is concerned with the copper oxide solubility limit around 5 wt.-% or phase separation occurs already at lower doping levels, but is not visible because of the insufficient sensitivity of the measuring equipment.

Treatment at 450 °C resulted in reflexes narrowing, and, accordingly, in crystallites enlargement. For the samples cured at 350 °C, the width of the most intensive (101)

ZnO diffraction peak at its half-height is 1.43° and corresponds to 3 nm Scherrer crystallite size. At 450 °C this peak parameter decreases to 0.40°, and the average crystallite size increases to 21 nm. This value is consistent with grain sizes obtained from SEM and TEM study. Additionally, the comparison of XRD patterns showed no difference in reflexes width for samples with different dopant concentrations. All patterns have a significant reflexes broadening, thus, it was impossible to estimate the main phase (ZnO) peaks position change and to make any conclusions about solid solution formation. For such complex nanocrystalline systems, it is a frequently occurring situation due to inhomogeneous strains and variation of lattice parameters from crystallite to crystallite.

4.7.6 FTIR study of ZnO:Cu calcined at various temperatures

Thermal degradation of 5 wt.-% doped system is followed by means of FTIR in Fig. 79. Infrared spectra of individual ZnO and CuO is can be found elsewhere.[220] Both oxides are characterised by signals in the region 385–690 cm^{-1} which are assigned to metal-oxygen stretching vibrations. However, structure of the bands in ZnO and CuO is clearly different: zinc oxide shows one broad structureless band centred around 460-390 cm^{-1}, copper oxide shows two well resolved bands at 700 and 560 cm^{-1}.

After thermal treatment at 270 °C, the broad structureless absorption at 3650-3150 cm^{-1} corresponding to the O-H stretching vibration of crystal water and assisted by intense signals of in-plane deformation vibrations around 1390 cm^{-1} and around 1625 cm^{-1} is observed, little bands corresponding to underdecomposed organic fragments are seen as well.

However, a broad vibration of ZnO and a narrow intense band of CuO at 554 cm^{-1} are also visible. The second mode of CuO at approximately 690 cm^{-1} has a very low intensity and cannot be considered as significant. At the temperature of 350 °C, there are no more organic ligand fragments, OH-vibrations are significantly diminished, and the CuO band also shows a decreased intensity. The material can be characterised as completely inorganic with slightly hydroxylated surface. After calcination at 450 °C, the individual vibration of CuO is totally absent, and the rest of it looks like a shoulder of the wide ZnO band.

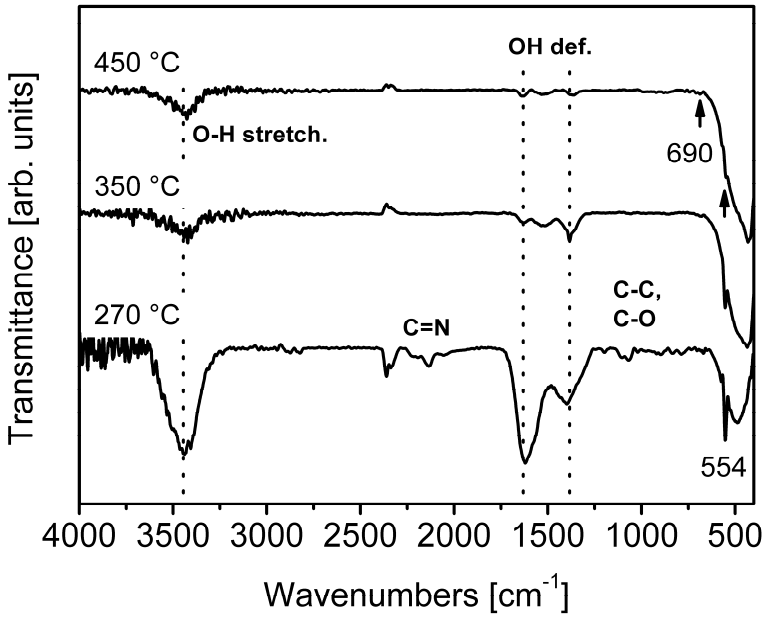

Figure 79. FTIR spectra of the sample with 5 wt.-% doping concentration, processed at different temperatures.

4.7.7 Photoluminescence spectra of Cu-doped ZnO nanorods

PL spectra of the nanorods taken at ambient temperature are compared in Fig. 80.

The sample containing 0.1 wt.-% CuO exhibits a broad band in the region between 370 and 600 nm with prominent two maxima at 415 and 418 nm. The large width of the UV band is associated with the broadening effect (towards longer wavelengths) in the presence of Cu, which was also reported for Cu-doped ZnO nanorods prepared by thermal diffusion.[141]

As the dopant concentration increases, a steady shift towards lower frequencies is observed, indicating reduction of the band gap. Similar dependence was observed previously for Cu-doped ZnO nanostructures grown by CVD method.[164] Parallel with this red shift, the band becomes strongly split, appearing at 431 and 439 nm for 5 wt.-% doped samples. The intensity of the signal at a larger wavelength systematically increases with respect to the signal at 415-431 nm. Additionally, the visible shoulder around 470 nm appears for 5 wt.-% doping. The UV emission signal in this system can be ascribed to the recombination of free excitons in ZnO, and the signal slightly shifted to the visible region is normally referred to as defect and

impurity-related, which explains the comparative intensity increase with the higher doping levels.

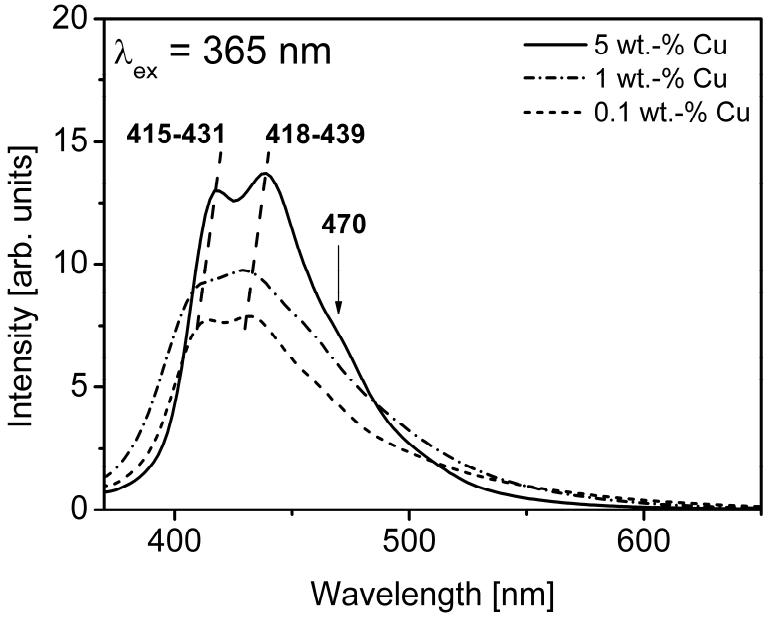

Figure 80. PL spectra of the nanorods calcined at 450 °C.

Analogous combination of the bands at 2.95 and 2.55 eV (420 and 484 nm respectively) has been reported for Cu-doped ZnO nanowires made by VLS process, the red shift of the signals in comparison with pure ZnO was attributed to the contraction of the optical band gap due to the implanted transition metal ions.[157] Thus, the obtained PL spectra are in accordance with a number of previously published works on nanoscale Cu-implanted ZnO systems.

4.7.8 XANES and HERFD spectra of ZnO:Cu nanorods

To understand the oxidation state of Cu in the nanorods, an X-ray absorption study was performed using high energy resolution fluorescence detected (HERFD) spectroscopy to plot the Cu K edge of the samples and Cu reference samples. The spectra can be understood by comparison with spectra of well characterised model compounds, to understand the origin of spectral features and how this relates to the nanorod sample structures. The position of the absorption edge depends on the oxidation state of the investigated atom and thus provides information about the Cu valency. Where it is difficult to directly compare the edge energy position (if the

edges have different shapes and slopes) then comparison with the spectral features of reference compounds is instructive. Fig. 81 shows the Cu *K*-edge XANES and Kα_1 HERFD spectra of the reference compounds with Cu in three possible formal oxidation states (Cu^{2+}, Cu^{1+} and Cu^0) compared to XANES/HERFD spectra of the Cu-doped ZnO nanorods.

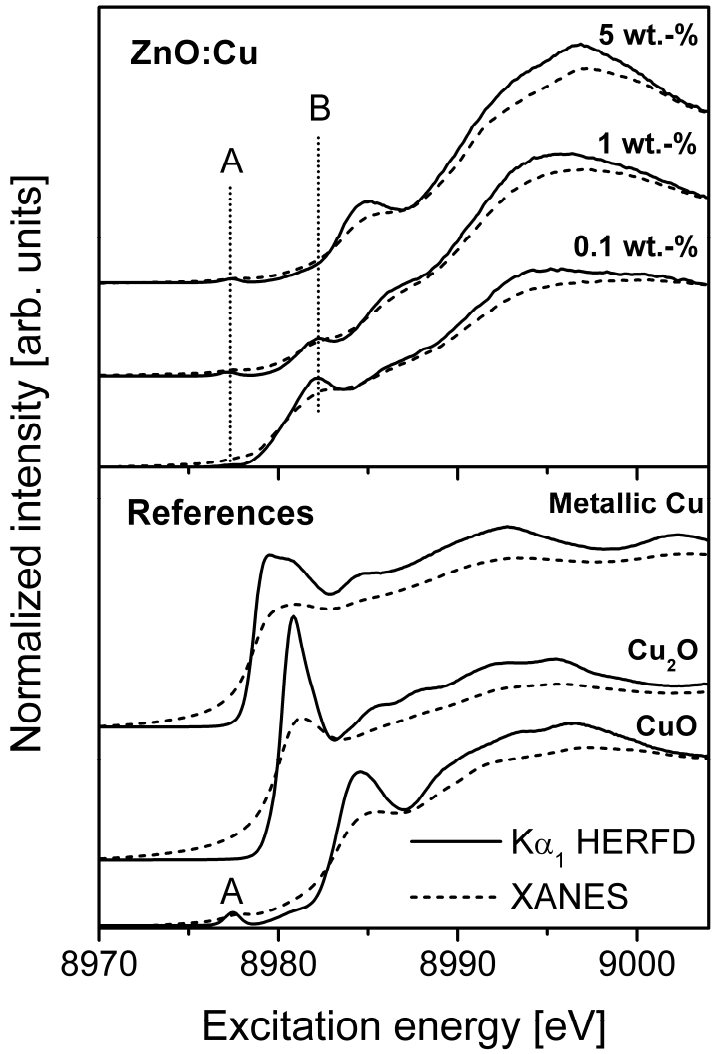

Figure 81. Cu *K*-edge XANES (dashed line) and Kα$_1$ HERFD (solid line) spectra of the Cu-doped ZnO nanorods with different doping concentrations (top panel) and Cu^{2+} (CuO), Cu^{1+} (Cu_2O) and Cu^0 (metallic Cu) reference sample spectra (bottom panel). The signal intensity of the 0.1 wt.-% ZnO:CuO sample was increased by a factor of 50 for comparison.

The spectrum for the 5 wt.-% nanorod samples resembles most closely the spectrum of the CuO reference sample. None of the nanorod sample spectra resemble the reference spectra for metallic Cu or Cu_2O. The spectrum of metallic Cu shows a

smooth edge jump with no pre-edge or edge states, due to the continuum of states at the absorption edge, characteristic for a metal. The nanorod samples all show some pre-edge and edge structure demonstrating that Cu in the nanorods has a valency higher than 0. However, the nanorod samples also do not have the strong white line intensity seen for Cu in Cu_2O at 8.981 keV, thus Cu in the nanorods does not appear to be of valency (I).

The small pre-edge feature marked 'A' observed in the 5 wt.-% and 1 wt.-% doped nanorod sample in Fig. 81. relates to the quadrupolar 1*s*-3*d* transition, which is only allowed for $3d^9$ Cu^{2+} ion in CuO and is not observed in $3d^{10}$ Cu^{1+} in the Cu_2O reference spectrum.[160] This pre-edge peak is not observed as clearly in the 0.1 wt.-% doping level samples but it is present. This feature can only be observed in the HERFD spectra and not in the standard XANES, which is due to a reduced spectral broadening and a lower background in the HERFD measurements, facilitating small pre-edge peak identification. The pre-edge peak position of the nanorod samples is consistent with that seen for the equivalent peak in the CuO reference spectrum, and suggests that the implanted copper exists as Cu^{2+} ions.

The 1 wt.-% and 0.1 wt.-% nanorod samples do not closely match any of the reference compounds due to the feature marked in Fig. 81 as 'B'. This peak becomes the prominent spectral feature in the edge region as the concentration of Cu in the nanorods is decreased. The position of this peak does not correspond to that of a peak seen in the model compounds containing Cu^{1+} or Cu^{2+} ions. This peak may be explained as a "shakedown feature" from the 1*s* → 4*p* transition in the Cu^{2+} ion, caused by charge transfer from the metal to surrounding ligands and subsequent screening of the Cu 1*s* core hole due to orbital mixing, as described previously by Ma *et al.* for PLD-grown ZnO:Cu films.[160]

4.7.9 XPS analysis of Cu-doped ZnO nanorods

The survey XPS spectrum of the 5 wt.-% sample is presented in Fig. 82, and the slow scans of Cu 2*p* level of the samples with 5 and 3 wt.-% are shown in Fig. 83 (3 wt.-% is not a typical concentration in this work, but lower concentrations could not be investigated due to the limitation of ESCA/XPS). The survey spectrum shows no organic or other contamination, which is consistent with EDX and FTIR studies. The Cu $2p_{1/2}$ and Cu $2p_{3/2}$ signals for both studied concentrations are broad asymmetric

peaks located around 952.1 and 932.4 eV respectively (referenced to C 1*s* core level of artificially introduced into the sample carbon at 284.6 eV), suggesting variations in copper ions environment. These binding energies agree with the data reported previously for ZnO:Cu nanowires synthesised via vapor-transport method.[219]

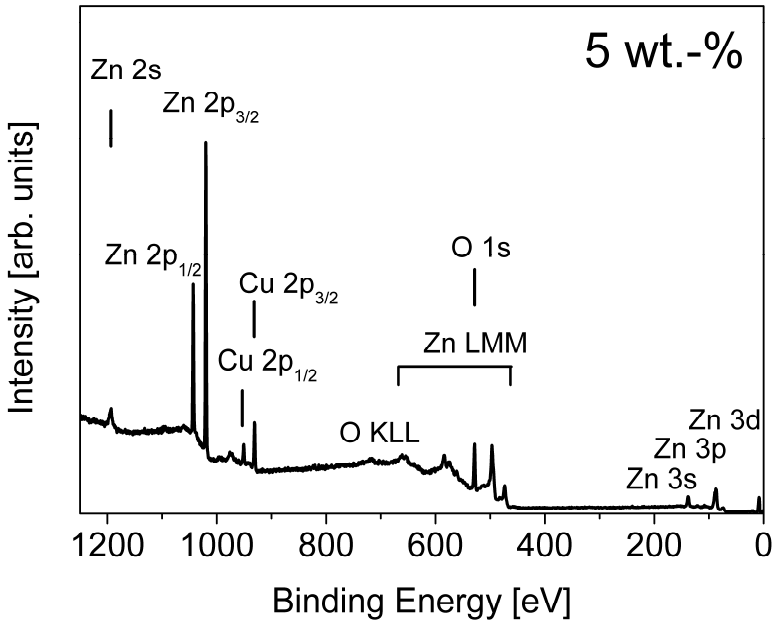

Figure 82. The survey XPS spectrum of the 5 wt.-% doped sample.

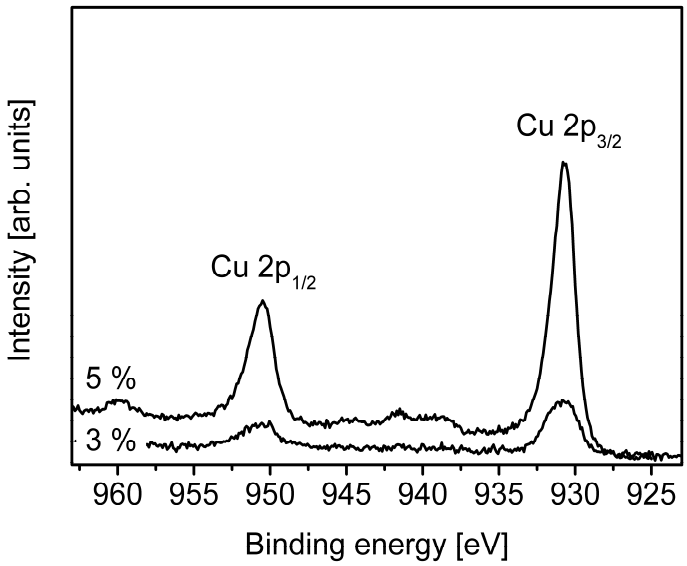

Figure 83. Slow XPS scans of Cu 2p level of the samples with 5 and 3 wt.-% doping concentrations.

As seen from Fig. 83, ratio of peak areas of 3 wt.-% and 5 wt.-% doped samples is not 3:5. The quantitative analysis shows that the doping concentration in the 5 wt.-% sample is in fact around 8 wt.-% and does not meet the EDX analysis results. Apart from the accuracy of XPS, there is one more possible explanation of this effect. The frequent problem during nanomaterials doping is that impurities and defects are readily repelled from the interior to the surface of nanostructures, especially during a synthesis at elevated temperatures. At the same time, XPS is a surface analysis method, which penetrates into the sample only a couple of nanometres deep. Combination of these two factors can result in a seeming concentration increase.

4.8 Metal oxide Q1D structures achieved by infiltration of precursors into PAOX templates

In the course of the present work, ZnO and In_2O_3 nanowires were made with the help of PAOX templates. The difficulty here is that both alumina and oxides of interest have amphoteric character, and, therefore, selective etching of the template (usually, in alkaline solution) is very difficult. Alumina membranes were etched with 1M or 6M aqueous KOH solutions. Etching could not be performed reproducibly by means of the same duration. In some samples, alumina template was dissolved quicker and before nanowires, but in other identical samples the nanowires were destroyed even before the full template dissolution (sees examples in Fig. 84). Thus, all the samples had to be controlled visually during the process and rinsed with distilled water after different etching times.

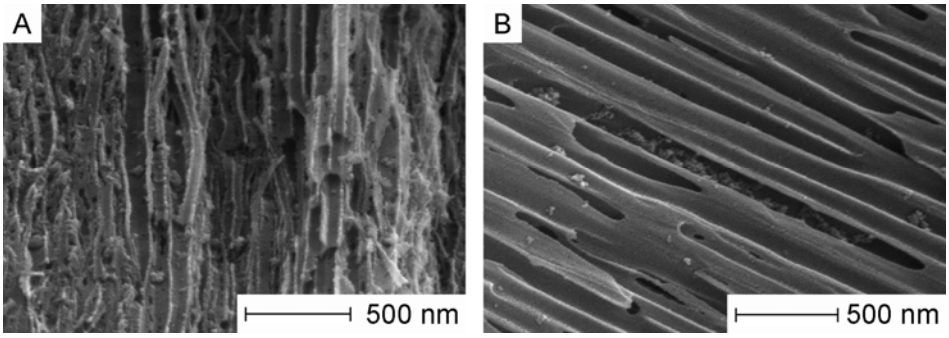

Figure 84. Result of the unsuccessful etching: ZnO nanowires are dissolved, but the rests of pore walls are still present. Image A shows 40 V templates, image B – 60 V templates.

4.8.1 ZnO nanowires from PAOX

ZnO nanowires from zinc oximato precursor are shown in Fig. 85 (40 V templates) and Fig. 86 (60 V templates from oxalic acid). A good yield of the nanowires is visible in SEM micrographs; however, all the synthesized at 250 °C samples were completely amorphous in XRD.

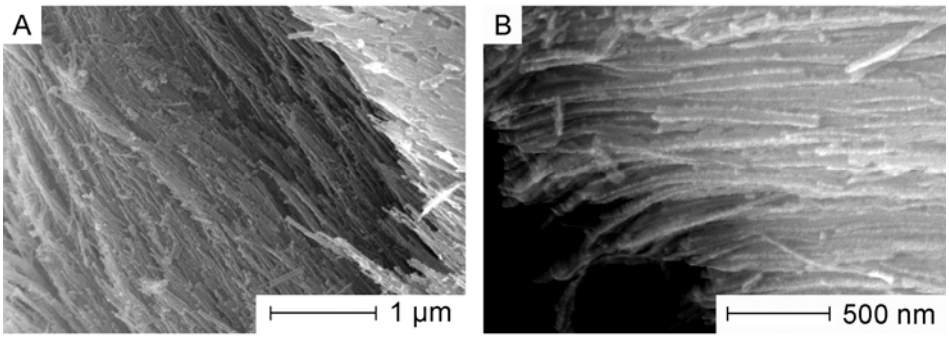

Figure 85. ZnO nanowires from 40 V PAOX templates (A). Fragments of PAOX pore walls are still observed as the evidence of poorly controllable etching (B).

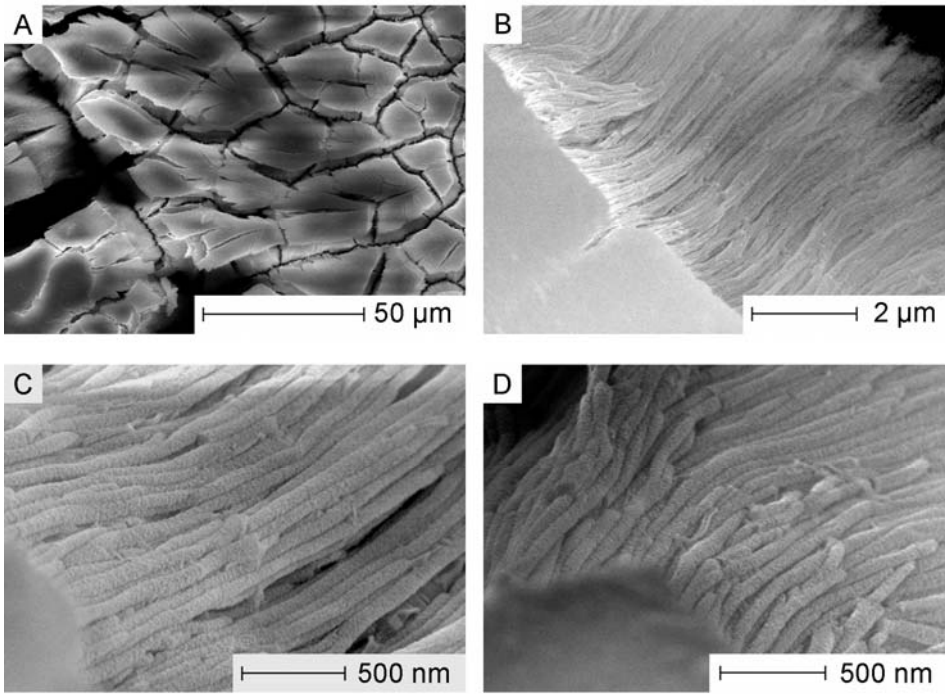

Figure 86. ZnO nanowires from 60 V PAOX templates. A high yield is observed (A, B), diameter of the nanorods was around 110 nm (C, D).

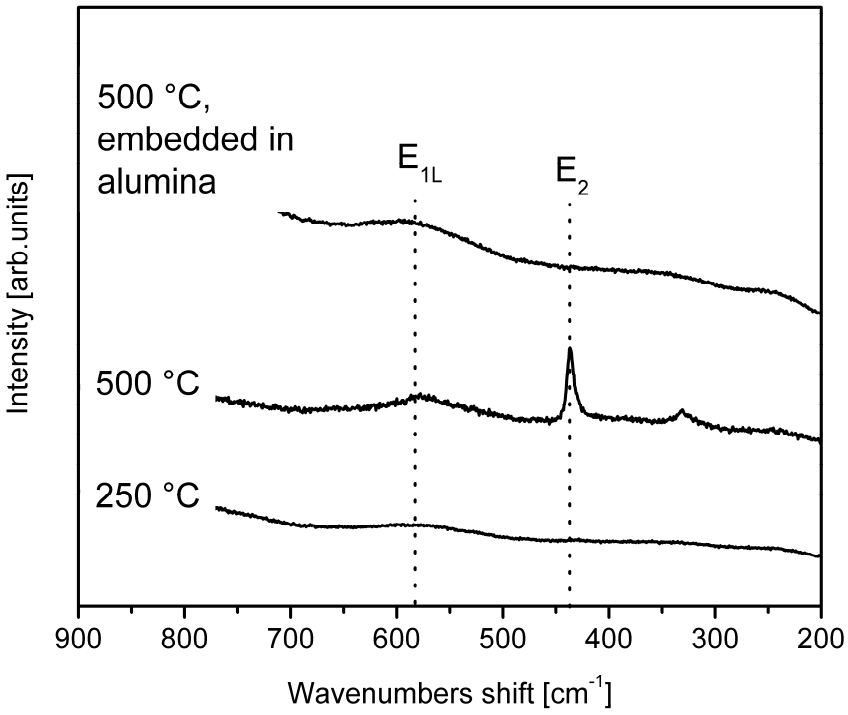

Figure 87. Raman spectra of ZnO nanowires from PAOX templates.

The Raman spectra (Fig. 87) show two features described above for ZnO nanorods from polycarbonate templates: the E_{1L} mode corresponding to impurities and structural defects, and the E_2 mode for hexagonal wurtzite phase. It is remarkable that no signals are developed after the conversion at 250 °C. If ZnO nanorods are first liberated from alumina and then processed at 500 °C, the prevailing wurtzite E_2 peak is seen, but the defects are also present. If the thermal processing at 500 °C is still carried out within the alumina pores, the broad signal corresponding to impurities and defects is seen, but no signs of crystalline structure formation can be detected.

4.8.2 In_2O_3 nanowires from PAOX

Indium oxide nanowires were made by infiltration of aqueous In_2O_3 colloid dispersion into PAOX and sintering of the PAOX/In_2O_3 system at 500 °C. For this experiment, a 40 V PAOX template was taken. Colloid In_2O_3 dispersion was synthesized from indium nitrate by means of pH value increase with NH_3.[221] Dynamic light scattering

investigation showed that around 90% of the colloid particles have dimensions between 12 and 21 nm (see Fig. 88).

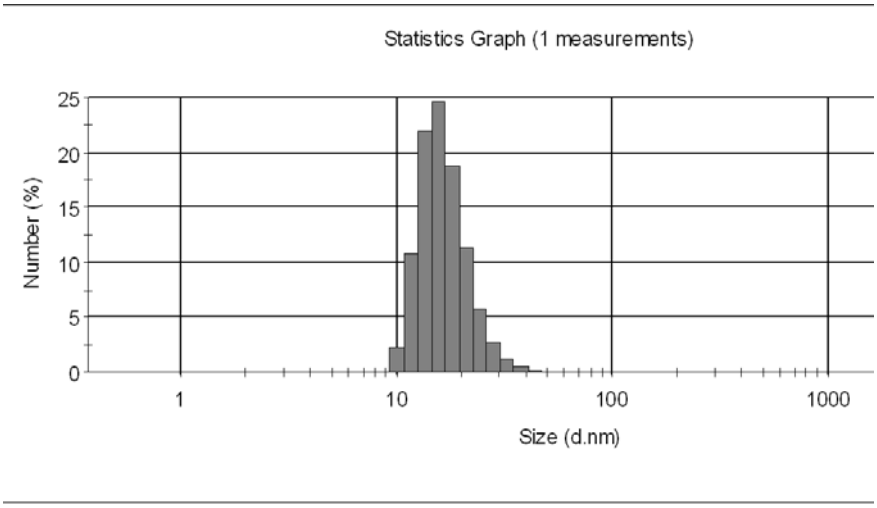

Figure 88. Dynamic light scattering bar chart for In_2O_3 colloid dispersion, used for impregnation into PAOX templates and synthesis of In_2O_3 nanowires.

SEM images demonstrated a good yield of the nanowires (Fig. 89), however, the material turned out to be totally amorphous in XRD.

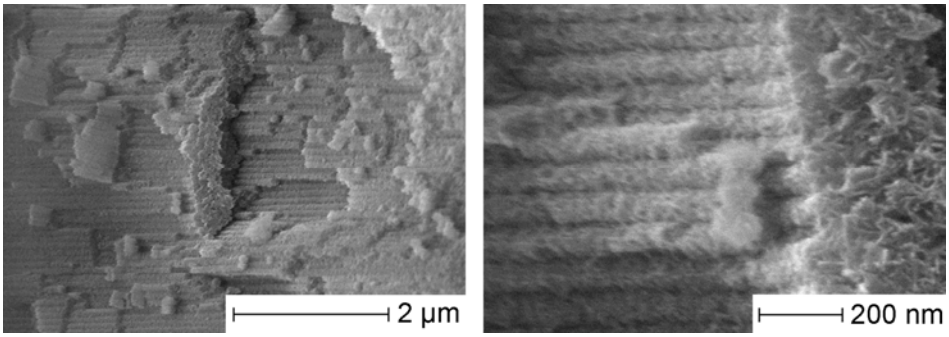

Figure 89. Indium oxide nanowires, composed of colloidal particles. The diameter of the wires is in the range 60-70 nm.

In conclusion, it is obvious that PAOX membranes are less suitable for metal oxide Q1D nanostructures synthesis than polycarbonate templates. Both the PAOX and the metal oxides of interest are amphoterous and are dissolved at practically equal pH values. Thus, the selective etching of the PAOX templates was not possible and did not display reproducible results.

5 Experimental part

5.1 Samples preparation

5.1.1 Preparation of PAOX templates

The two-step anodization of aluminium sheets (PURALUX®, purity 99.93%, thickness 1 mm) was performed in a 0.3 M oxalic acid or in 5-10 wt.-% sulfuric acid solutions as previously described in the literature.[26, 27] The process was carried out under potentiostatic conditions at 60, 40, 27 or 20 V potential differences (pore diameter around 70, 40, 30 and 20 nm respectively). A thermostatic system kept the temperature of the open electrolytic bath (Fig. 90) around 0°C and the solution was intensively agitated with a magnetic stir bar in order to eliminate the heat from the anode effectively.

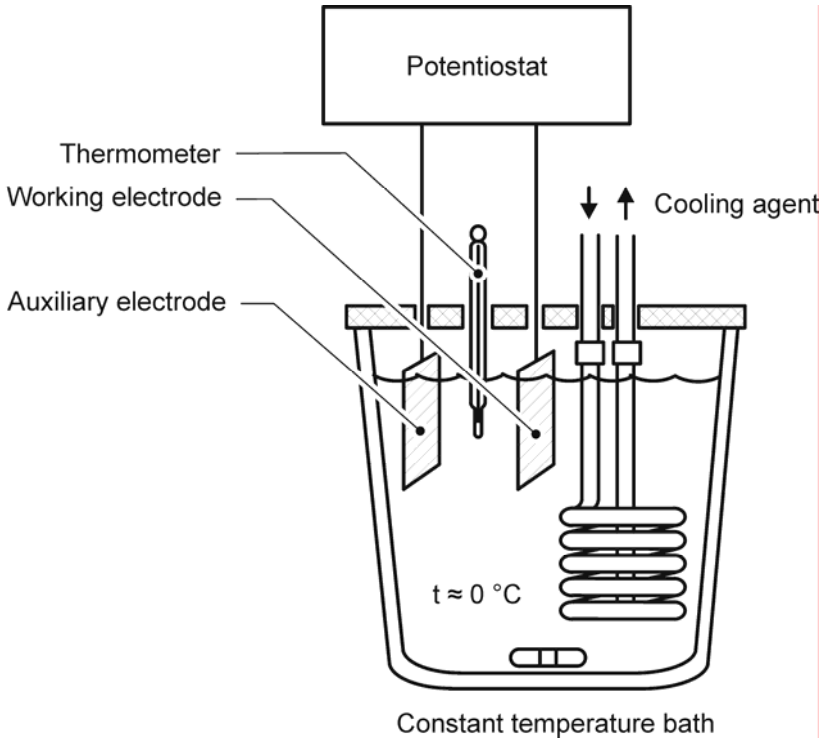

Figure 90. Schematic drawing of the electrolytic bath used for PAOX films preparation.

Since water in the solution is the electro-active reactant in the electrochemical synthesis of anodic alumina,[25] inert materials (e.g. platinum, graphite) may be utilised as a cathode. The shape and surface area of the cathode do not influence so

much as in case of reactive (i.e. consumed) cathodes. In the present work, aluminium sheets of the same surface area, as that of the anode, were used for auxiliary electrodes preparation.

The electrolyte (i.e. oxalic or sulphuric acid) in the solution creates the migration current, but is not consumed during the anodization process. Therefore, the same electrolyte solution may be used to produce porous anodic films routinely.

After the first anodization for 360 min, the Al sheets were immersed in the etching solution (0.16 M $K_2Cr_2O_7$ and 1.5 M H_3PO_4); 24 g $K_2Cr_2O_7$ and 59 ml H_3PO_4 85 wt.-% were filled up to 500 ml with distilled water and pre-anodized Al-sheets were kept in this mixture at 50°C for 30 min to remove the oxide layer and to prepare the pre-structured Al surface for a better following hexagonal nanopore ordering. The second anodization was performed for 17-20 hours (depending on the desired film thickness). Resulting anodic film adheres well to the aluminium substrate and is impossible to separate mechanically. The *redox change technique* (or *polarity reversal*)[171], which is widely used in oxide and hydroxide films preparation by means of electrochemical methods, is a simple yet effective solution to the problem of the porous film and Al substrate separation. Due to the hydrogen release at the substrate/film interface, the PAOX samples were detached from aluminium, and could be completely separated with a knife or blade. Large membranes (surface area of several cm^2) with the backside closed were obtained by this method.

To open the backside of PAOX films, the barrier layer was removed in an etching aqueous solution (0.16 M $K_2Cr_2O_7$ and 1.5 M H_3PO_4, the same as used previously to dissolve the film after pre-anodization stage). At this stage, the pores become widened and their diameter increases. The barrier oxide layer dissolves in an etching solution slower than the porous layer,[166] which may lead to the complete inter-pore walls dissolution even before the channels are completely open from both sides. In connection with this, different masking techniques have been invented to protect the porous side from the etchant.[167, 168] The protective coatings, described in the literature, are a mixture of nitrocellulose and polyester resin in ethyl acetate, butyl acetate, and heptane,[167] or even commercial nail polish,[168] which has a similar composition. After this protective coating application and etching of the barrier layer, the organic rests are removed from a PAOX template with acetone.

Alternatively to wet etching, the contollable barrier layer removal has been reported with other methods, like ion beam etching (uniform holes in the barrier layer with

diameter down to 5 nm, can be obtained using sulfuric PAOX). This method, however, was not available for routine use.[222]

In the present work, the novel technique of barrier layer removal with teflon protective layer has been developed. This method prevented the critical widening of pores and the complete inter-pore wall dissolution. It made the reproducible removal of the barrier layer and opening of a reasonable number of nanochannels from both sides for the subsequent capillary driven infiltration possible. The masking method is schematically shown in Fig. 91.

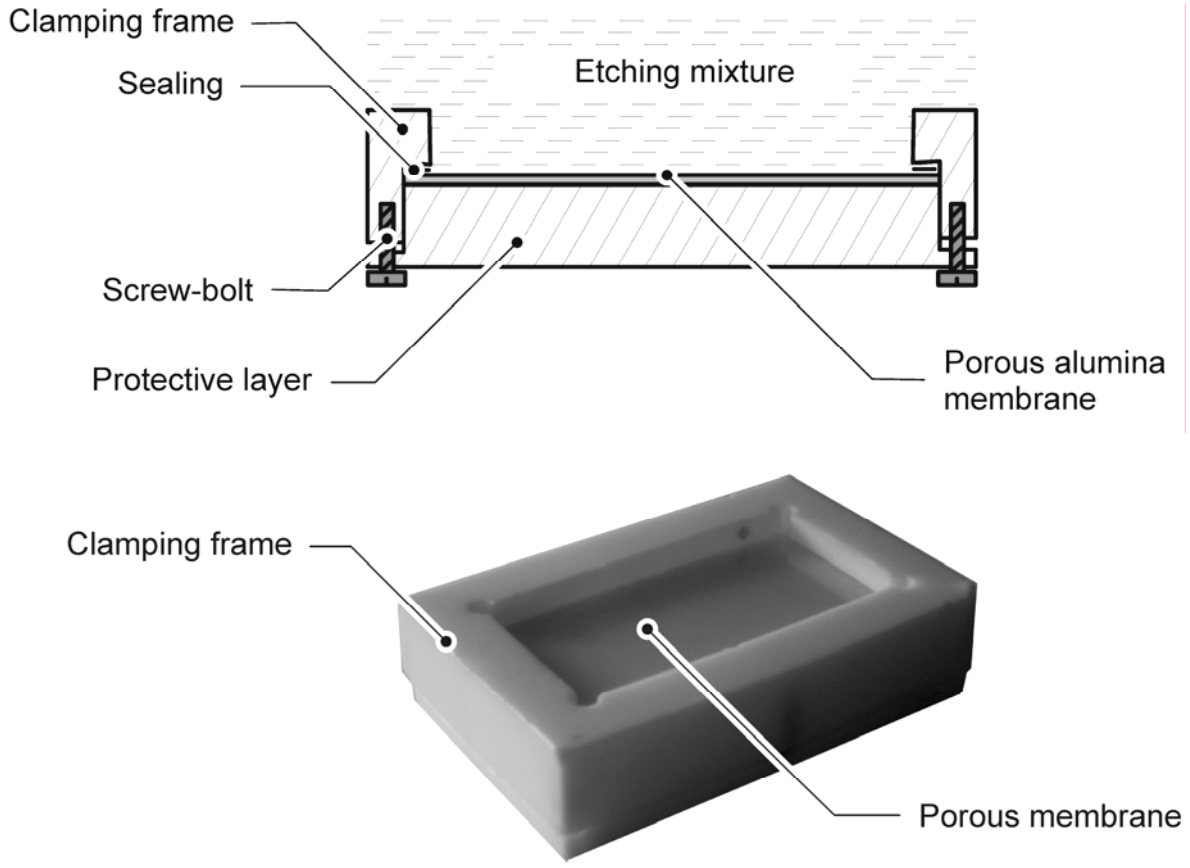

Figure 91. Scheme of the protective teflon construction, used for reproducible barrier layer removal; porous side of PAOX template is pressed to a flat block along the perimeter with a frame, so that only barrier layer stays in contact with the etching solution through the frame window. Laboratory film is used as a sealing. Screw-bolts are made of polypropylene and are resistant towards aggressive etchant.

The main advantages of the method, when compared to the previously reported protective coatings, are:

- reinforcement of brittle PAOX membranes by the flat teflon, which makes it easier to handle the template in a stirred etchant mixture
- no organic rests on highly sorptive surface of the alumina, which are difficult to remove with acetone completely (methods from literature were also tried).

5.1.2 Synthesis of Q1D-SiOC Nanostructures in PAOX Templates of 20 and 40 nm Nominal Pore Diameter

Two commercially available thermosetting resins, Ceraset™ (KiON corporation) polyureasilazane (SiCN precursor) and SP Matrix™ (Starfire Systems company) polymer (SiC precursor) (Fig. 92), were used for the infiltration PAOX templates in a glove box under inert atmosphere (Ar).

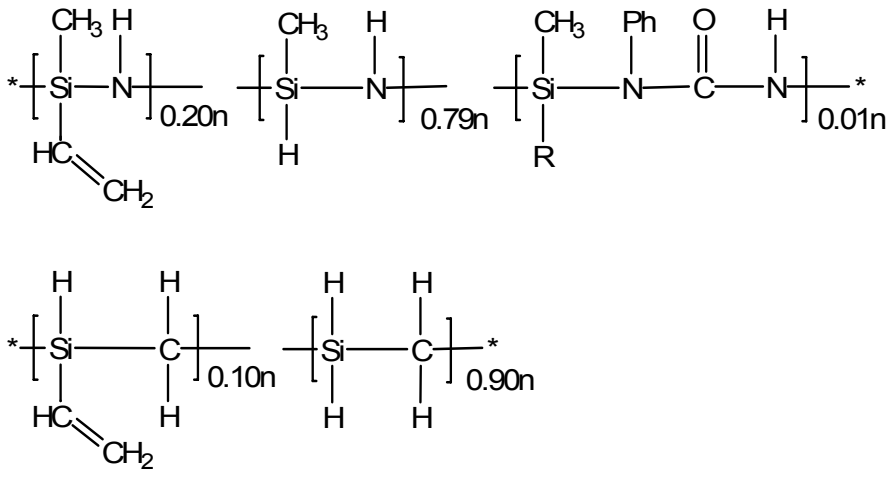

Figure 92. Structural formula of the KiON Ceraset polyureasilazane (top) and of the SP Matrix polymer (bottom).

Several drops of a precursor were placed on a glass slide, and then a PAOX membrane is placed on top of a liquid. The increasing transparency of the membrane indicates filling of the pores by capillary force infiltration. In case with 20 nm pores,

the precursor was diluted with n-hexane (10 vol.-% of n-hexane) and templates were fully immersed in the mixture in a Schlenk flask under argon atmosphere for several hours. After the infiltration, excess of the precursor was wiped from the membrane surface with a cotton tissue. The ceramization reaction was performed in a quartz tube in an argon flow. Setup of this experiment with a special Schlenk-type quartz tube is shown in Fig. 93. After a cross-linking step at 260 °C for 2 h the temperature of the tube furnace was increased and hold for 2 h at 1000 °C to achieve the transition of the precursor to the final ceramic material.

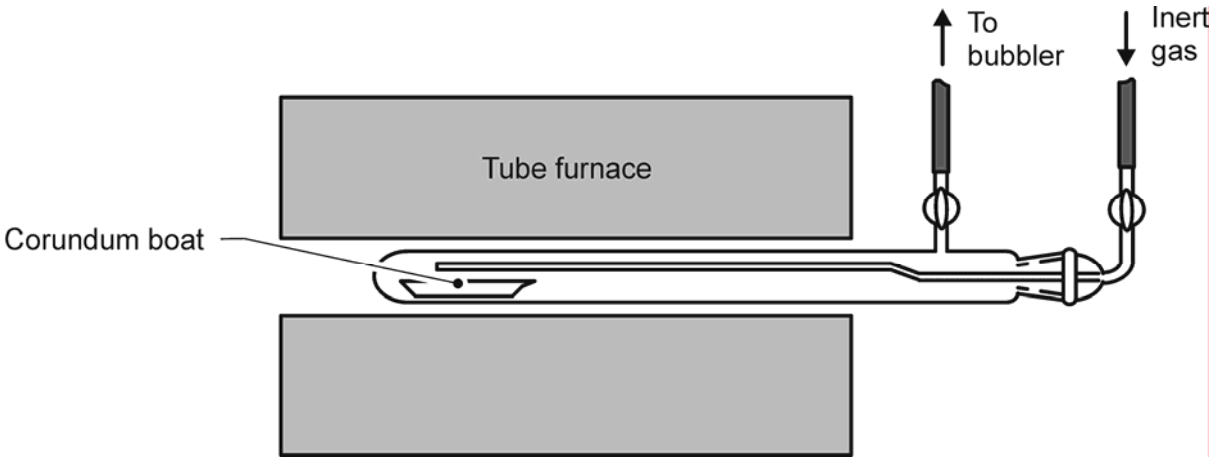

Figure 93. Experimental setup for precursor conversion under inert atmosphere. The inert gas flow was controlled with a standard oil gas bubbler (two bubbles per second).

To dissolve the alumina template, the samples were placed either in a 48 wt.-% HF solution at ambient temperature or in 85 wt.-% H_3PO_4 solution at 110 °C (the etching time varied from 20 to 48 h). The resulting material was thoroughly rinsed with distilled water and dried at 130 °C. A summary of the processing steps is schematically depicted in Scheme 6.

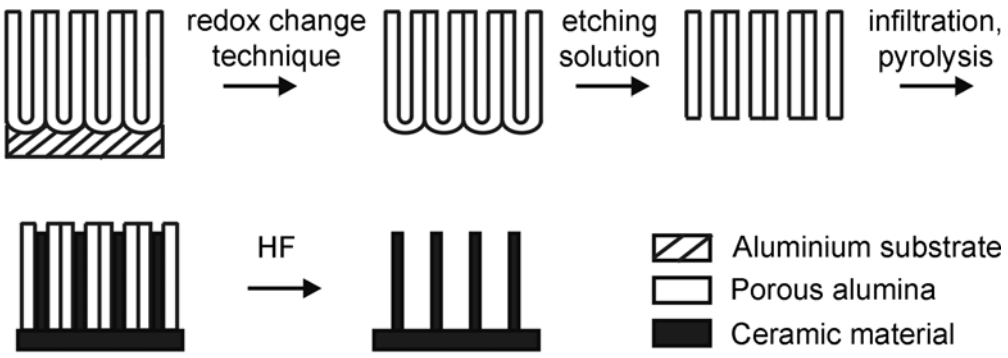

Scheme 6. Schematics of the template-based approach to polymer-derived ceramic wires.

5.1.3 Preparation of metal oxide nanorods and nanotubes from oximato precursors in porous polycarbonate templates

Metal oxide nanorods (ZnO, ZnO:Cu, ZnO:Mn, MgO) and nanotubes (In_2O_3) were prepared using complexes with oximato ligands.

Table 5. Some parameters of the used oximato precursors.

Product	Precursor systematic name	Conversion temperature [°C]	Theoretical inorganic yield [%]
ZnO	Bis[2-(methoxyimino)propanoato]zinc	160	24.42
CuO	Bis[2-(methoxyimino)propanoato]copper	180	23.98
MnO*	Bis[2-(methoxyimino)propanoato]manganese	180	18.89
MgO	Bis[2-(methoxyimino)propanoato]magnesium	450	12.97
In_2O_3	Tris[2-(methoxyimino)propanoato]indium	350	29.97

* Decomposition is carried out in inert atmosphere.

Oximato complex of zinc have been earlier studied in our group in connection with preparation of thin films from single source molecular precursors and development of printable electronics.[11, 186] Metal oximato complexes (Zn, Cu, Mn, Mg, In), were synthesised by following procedures:

Di-aqua-bis[2-(methoxyimino)propanoato]zinc

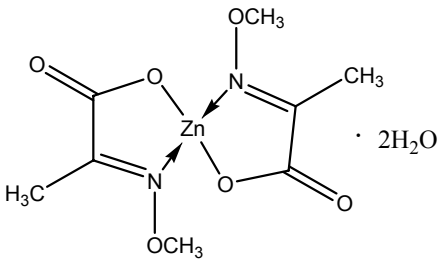

Tetraethylammonium bicarbonate (22.94 g, 120 mmol) was added in small portions to a stirred solution of pyruvic acid (5.28 g, 60 mmol) and methoxylamine hydrochloride (5.02 g, 60 mmol) in 20mL of water. After the termination of visible gas evolution the solution was stirred for two hours. Then $Zn(NO_3)_2 \cdot 6H_2O$ (8.92 g, 30 mmol) was added, the mixture was stirred for another 4 hours and then cooled to 5 °C. The resulting white precipitate was filtered off and recrystallized from hot water.
Yield 5.5 g, (56.7%).

Di-aqua-bis[2-(methoxyimino)propanoato]copper

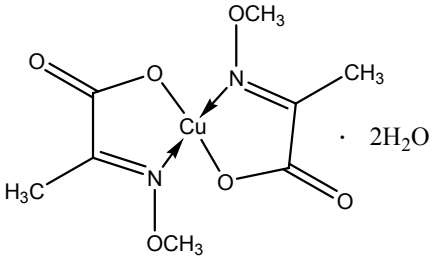

A sample of 4.99 g of copper acetate dihydrate (25 mmol) in 25 ml water was added to a in-situ prepared acid oxime ligand in water. The ligand is prepared by taking 50 mmol each of pyruvic acid (4.40 g, 50 mmol) and O-methylhydroxylamine hydrochloride (4.18 g, 50 mmol). The reaction mixture was stirred for further four hours, during which a pale green product was formed. The product is filtered and washed with water and dried at 50 °C to give pure substance.
Yield 2.26 g (45.3 %).

Di-aqua-bis[2-(methoxyimino)propanoato]manganese

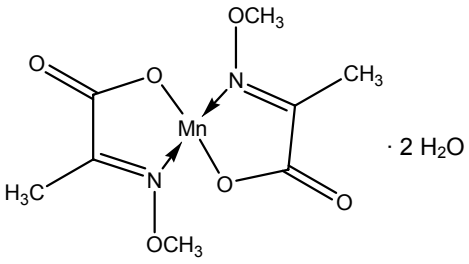

7.52 g (90.0 mmol) of methoxylamine hydrochloride and 9.9 g (90 mmol) sodium pyruvate are dispersed in 30 ml of water. 9.01 g (90.0 mmol) potassium hydrocarbonate is slowly added and stirred at room temperature till all the substances are dissolved. 7.28 g (45.0 mmol) of manganese (II) chloride dihydrate is added and the mixture is stirred for 1 hour. The colourless solid is filtered out and dried in vacuum. For the purification, the solid is dispersed in 400 ml of acetone and the insoluble residues are filtered out. The solution is reduced to 50 ml and the precipitate is filtered and dryed. Yield below 30 wt.-%.

Tris[2-(Methoxyimino)propanoato]indium

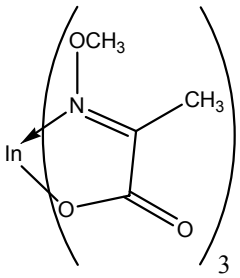

Sodium hydrogencarbonate (3.36 g ; 40 mmol) was added in small portions to the suspension of sodium pyruvate (4.40 g; 40 mmol) and methoxylamine hydrochloride (3.34 g; 40 mmol) in 100 ml of distilled water. After the gas evolution had ceased, the clear solution was stirred for further 30 minutes. The water was removed completely using a rotary evaporator. The remaining white powder was suspended in 100 mL of tetrahydrofuran and a solution of anhydrous indium chloride (2.95 g ; 13.3 mmol) in 150 mL tetrahydrofuran was added dropwise. The reaction mixture was stirred overnight and filtered thereafter. The solvent was removed using a rotary evaporator

until about 50 mL of the solution remained. Precipitation with toluene yielded a white powder, which was filtered off. For further purification the raw product was digested in dichloromethane and the solution filtered. The product was obtained by precipitation with n-hexane, filtered off and dried in vacuum. The obtained product is a white and non-hygroscopic powder. Yield was not determined.

Tris(aqua)-Bis[2-(methoxyimino)-propanoato]magnesium

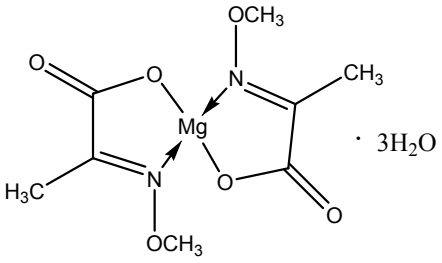

Hydromagnesite $Mg_5(CO_3)_4(OH)_2{\cdot}4H_2O$ (10.00 g; 21.4 mmol) was added in small portions to the solution of pyruvic acid (10.56 g; 120 mmol) and methoxylamine hydrochloride (10.04 g; 120 mmol) in 200 mL of distilled water. After stirring for 2 hours the excess of hydromagnesite was removed by filtration. The solvent was removed to a volume of about 50 mL using a rotation evaporator, whereby the temperature was not allowed to exceed 55 °C. A white powder precipitated at 5°C overnight and was recrystallised from water. The product formed colorless, lustrous flakes. Yield 24.03 g, 64.5%.

To synthesize single-component Q1D materials (from one pure oxide), the saturated solution of a precursor was prepared in an alcohol (optionally ethanol or 2-methoxyethanol). Alternatively, another organic solvent, which does not affect the polymeric template, and is clearly evaporated or decomposed into volatile products, can be used. To make doped materials, mixtures of corresponding oximates in certain proportions have to be prepared, as mentioned below.

ZnO:Mn doped material:

Solutions of oximato precursors in 2-methoxyethanol (50 $g{\cdot}l^{-1}$ of Zn-oximate, M = 333.4 $g{\cdot}mol^{-1}$, and 5 $g{\cdot}l^{-1}$ of Mn-oximate, M = 323 $g{\cdot}mol^{-1}$) were prepared in volumetric flasks. After that, portions of the solutions were mixed with expectation of specified dopant concentrations after evaporation and thermal decomposition into oxides. In the case with 0.1, 0.01, and 0.005 wt.-% doping concentrations, the

volume of Mn-oximate solution was precisely controlled with a 100 µl GCMS-syringe. Summary of the mixed solutions preparation is presented in Tab. 6.

Table 6. Summary of the preparation of MnO doped ZnO from mixed oximate solutions.

Solution portion volume, ml		Dissolved mass, g		Expected metal oxide mass, g		Resulting MnO concentration, wt.-%
Zn-oximato complex, 50 g·l^{-1}	Mn-oximato complex, 5 g·l^{-1}	Zn-oximato complex	Mn-oximato complex	ZnO	MnO	
7.8	4.6	0,389	0,023	0.095	0.005	5
8.1	0.9	0,406	0,005	0.099	0.001	1
8.2	0.091*	0,409	0,00045	0.0999	0.0001	0.1
8.2	0,009*	0,410	0,000046	0.09999	0.00001	0.01
8.2	0,005*	0,410	0,000023	0.099995	0.000005	0.005

* -Volume controlled with a GCMS syringe

ZnO:Cu doped material:

It was prepared in the same way as for ZnO:Mn. Solutions of oximato precursors in 2-methoxyethanol (50 g·l^{-1} of Zn-oximate, and 5 g·l^{-1} of Cu-oximate, M = 331.5 g·mol^{-1}) were prepared in volumetric flasks. In the case with 0.1 wt.-% doping concentration, the volume of Cu-oximate solution was precisely controlled with a 100 µl GCMS-syringe. Summary is presented in Tab. 7.

Table 7. Summary of the preparation of CuO doped ZnO from mixed oximato solutions.

Solution portion volume, ml		Dissolved mass, g		Expected metal oxide mass, g		Resulting CuO concentration, wt.-%
Zn-oximato complex, 50 g·l^{-1}	Cu- oximato complex, 5 g·l^{-1}	Zn-oximato complex	Cu-oximato complex	ZnO	CuO	
7.8	4.2	0.3891	0.0208	0.095	0.005	5
7.9	2.5	0.3973	0.0125	0.097	0.003	3*
8.1	0.8	0.4055	0.0042	0.099	0.001	1
8.2	0.08	0.4092	0.0004	0.0999	0.0001	0.1

* - this concentration does not appear in any analysis methods except XPS.

A porous polycarbonate film (Whatman Nuclepore™ track-etch membrane, nominal pore size 0.1 μm, or 0.03 μm) was immersed into the solution, dried in the air at ambient temperature, and cleaned from the excess precursor with a paper tissue.

Then, the thermal conversion of precursors was carried out in following regimes:

- Plain ZnO nanorods from pure zinc oximate were synthesized in a desiccator at 160 °C for 1 h;
- Mn-doped ZnO nanorods from the mixture of two corresponding oximates were put in a glass tube and then decomposed at 180 °C in inert gas (Ar) flow.

In the case with ZnO or ZnO:Mn nanorods, all the steps mentioned above result in a polycrystalline product. After that, the material was washed with CH_2Cl_2 to remove the polymeric template, decanted after precipitation and dried.

For MgO, ZnO:Cu, or In_2O_3, a dehydrated and solidified 'green body' nanorods are obtained within the pores in a dessicator at 160 °C, which need further thermal processing. After template dissolution with CH_2Cl_2, this 'green body' was put into a muffle furnace for 2 h at following temperatures:

- 350 °C to achieve crystalline ZnO:Cu or In_2O_3;
- 450 °C to synthesize MgO nanorods.

Each calcination temperature was based on thermogravimetric and XRD analysis. All the steps of the template-based process are shown below in the Scheme 7.

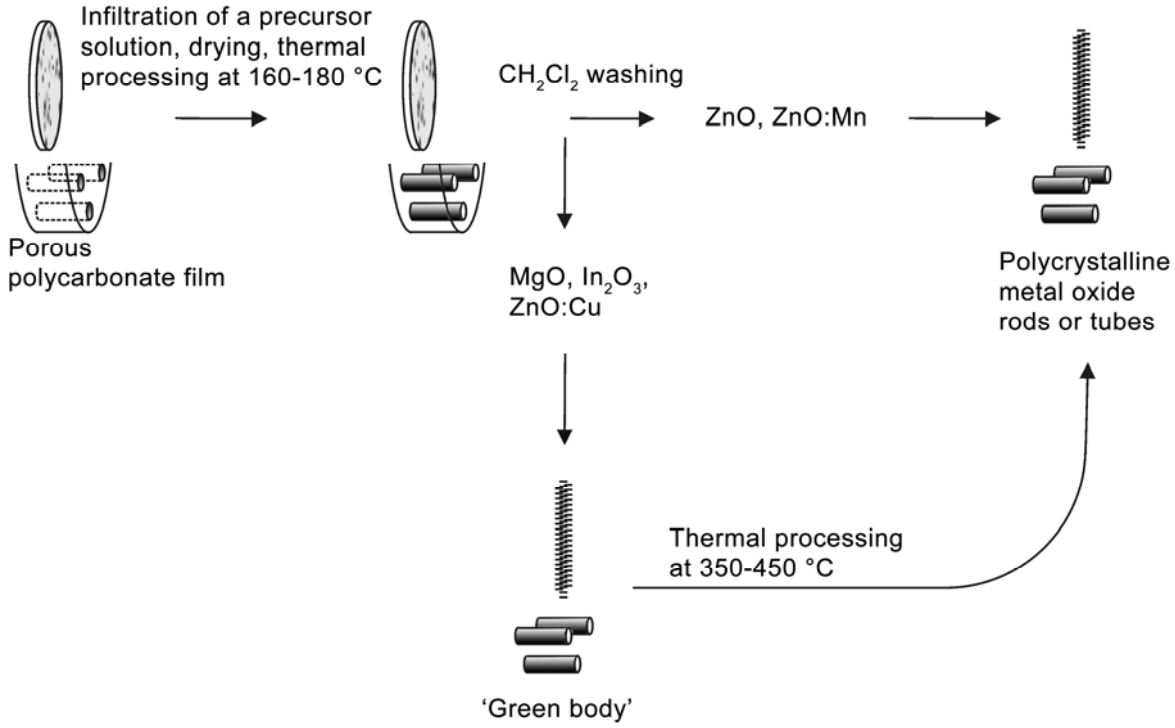

Scheme 7. Template-based route to polycrystalline metal oxide nanorods from oximato precursors.

5.2 Sample characterisation

5.2.1 Scanning Electron Microscopy (SEM) and Energy Dispersive X-Ray analysis (EDX)

The morphology of the commercially available polycarbonate and alumina templates, as well as self made alumina membranes with a smaller pore diameter and the resulting molded one-dimensional materials was studied by high resolution scanning electron microscopy (SEM) using a Philips XL-30 FEG coupled with an energy-dispersive X-ray (EDX) analyser. In all instances, samples were mounted on a metal sample holder with the help of conductive carbon-containing polymeric self-adhesive films. To avoid the negative charging effect, all the species with poor conductivity were sputtered either with 8-12 nm gold or 3.5-4.5 platinum-palladium alloy layers (Cressington 208HR Turbo Sputter Coater and Cressington MTM20 thickness controller). Samples with uneven surface were fixed with conductive silver paint or conductive carbon paste. The topographic analysis was carried out in the secondary electron regime with the accelerating potential between 20 and 25 keV.

In some cases, the qualitative elemental analysis based on characteristic X-radiation was performed.

The generation area of characteristic X-radiation depends on the incident electrons penetration, which, in its turn, depends on the sample material's density and on the accelerating voltage. To obtain contrast micrographs of submicrometer objects and to get the sufficient count rate on the EDX-detector, an accelerating voltage of 20 keV or higher had to be applied. The characteristic X-rays generation depth for analysed species with a density around 3 $g \cdot cm^{-3}$ (e.g. Al, ρ = 2.7 $g \cdot cm^{-3}$) is about 5 µm at the accelerating potential 25 keV. To obtain the depth smaller than 1 µm, one has to decrease the accelerating voltage. For example, the accelerating voltage for aluminosilicates (CuKα curve in Al) must be less than 10 keV, which is insufficient for receiving good images of the analysed nanomaterials at very high magnifications. Therefore, an additional area around isolated nanostructures is usually captured during the elemental EDX-analysis, mainly the underlying conductive carbon-containing film. This leads to excessive values in carbon content and makes the precise quantitative examination nearly impossible.

It is known that characteristic X-radiation is partially absorbed as it passes from the depth of a sample to the surface. Thin layers of sputtered dense noble metals (Au,

Pt/Pd) are necessary to overcome the accumulation of the negative charge on the sample surface, but they also definitely influence the percentage of the transmitted radiation of particular wavelengths and give their own additional peaks in EDX-spectra.

5.2.2 Transmission Electron Microscopy (TEM) and Selected-Area Electron Diffraction (SAED)

The advantage of TEM is the high magnification and the ability to provide both image and diffraction information from a crystallite. With the help of SAED, the crystal structure of different parts of a sample can be obtained. SAED patterns are used to determine lattice parameters by the same procedure used in XRD.
For this investigation, samples were dispersed in high purity grade ethanol with the help of an ultrasonic bath and then deposited on lacy-carbon copper grids of 300 meshes and dried in the air. Before electron microscopy examination, all samples were first checked with an optical microscope to confirm the successful deposition of the material from dispersion onto the sample holder. TEM images and SAED patterns were taken using a Tecnai G2 F20 microscope operated at 200 kV accelerating voltage at Ernst Ruska Zentrum at the Institut für Festkörperforschung (IFF) in Jülich.

5.2.3 Powder X-ray diffraction (XRD)

To follow the structural changes after the thermal treatment, qualitative X-ray analysis (XRD) of the species was carried out on a Stoe&Cie StadiP diffractometer in Debye-Scherrer geometry using Cu $K_{\alpha 1}$ radiation (λ = 1.541 Å) with a Ge (111) monochromator. The method provides information on lattice characteristics of solid crystalline substances, but sometimes can be very useful in amorphous substances analysis as well. The qualitative analysis consists in the interpretation of diffraction patterns, which are the sets of 2θ (diffraction angles) and I (arbitrary intensities). The Bragg condition represents the relationship between the diffraction angle and the interplanar spacing d:

$$2d\sin\theta = n\lambda$$

where *n* is the diffraction order (is a positive integer number, but usually assumed to be equal to 1) and λ is the X-radiation wavelength.

In multicomponent systems (e.g. composite or doped materials), the conclusion about solid solution formation can be made from the main phase lattice parameters change. However, in case of nanocrystalline systems, accurate parameters determination from X-ray diffraction data is often difficult because of the reflexes broadening (lattice constants vary from crystallite to crystallite under inhomogeneous strains). In connection with this, valuable information about components distribution can be additionaly obtained by means of transmission electron microscopy or Raman spectroscopy.

If there is no inhomogeneous strain, the crystallite size (the size of a coherent scattering area) can be estimated from the reflexes broadening using the Scherrer equation:

$$D = \frac{k\lambda}{\beta\cos\theta}$$

where *D* is a mean coherent scattering area size, *β* is the width of a diffraction peak at its half-height, *θ* is the reflection angle, and *k* = 0.9.

5.2.4 Raman Spectroscopy

Raman spectroscopy is more a structural characterisation technique than a chemical analysis. It is very sensitive to the lengths, strengths, and arrangements of chemical bonds in material, but less sensitive to the chemical composition.

Raman scattering is a non-destructive characterisation method for many recent studies of the vibrational properties of nanomaterials. The Raman effect is extremely weak, and, thus, intense monochromatic continuous gas lasers are used as the exciting light.

In the present investigation, Raman spectra were obtained on a Bruker FRA-106 Fourier-transform spectrometer. The character of some samples spectra (silicon-based carbon containing ceramic materials) suggested their thermal sensitivity. To eliminate this effect, the samples were grinded with KBr in an agate mortar, and then pressed onto a metal sample holder. Alternatively to the sample spinning, an

unfocused beam has been employed to reduce the laser beam residence on any one spot.

5.2.5 Infrared Spectroscopy (IR)

With the help of infrared spectroscopy, the type, surrounding environment and the concentration of a functional group in the sample can be determined.
In this method, the intensity of the radiation before and after the interaction with the sample is measured as function of light frequency. A plot of relative intensity versus frequency (or wavenumbers, – values, inverse to wavelength) is the infrared spectrum.

In this work, Fourier transform infrared spectra (FTIR, Nicolet Impact 400) of solid species were taken by a standard KBr discs method. The fluid substances were analysed between two KBr windows.

5.2.6 X-ray Photoelectron Spectroscopy (XPS)

In X-ray photoelectron spectroscopy, relatively low-energy X-rays are used to eject the electrons from the atom via the photoelectric effect. The kinetic energy of the ejected electron (E_E) is determined by both the energy of the incident photon (hv) and the bound electron state (E_B):

$$E_E = hv - E_B$$

Since values of the binding energy are element-specific, atomic identification is possible through measurement of photoelectron energies.

The typical peaks in XPS spectra correspond to the energy of characteristic electrons that leave the sample without energy loss processes. The photoemission from *p*, *d*, and *f* electron conditions with nonzero orbital moment gives spin-orbit doublets with the bands of non equal intensity.
The trails from the direction of a higher energy correspond to the electrons that endured inelastic scattering and energy loss on the way from the sample, a lower kinetic energy results in the apparent binding energy increase.

For the elements with $Z \leq 35$, Auger-processes of relaxation are extensively present. Since Auger peaks in photoelectron spectra are specific for every element, the identification of elements is possible.

The exact binding energy value depends on the chemical environment of an atom. The energy of an electron in the internal shell depends on the coulomb interaction with other electrons and the attractive potential of the nucleus. Any change in chemical environment will cause the electrons charge redistribution, the change of inner electrons potential, and the change in their binding energies. Thus, the electronegative surrounding atoms will shift binding energies to higher values.

In the present work, the chemical states of elements are examined on an Escalab 250 Spectrometer with a monochromatized Al anode. The solid samples are connected to the spectrometer with the help of the electric contact; dielectric samples can be additionally sputtered with a thin gold layer to avoid the charge accumulation.

5.2.7 Photoluminescent (PL) Spectroscopy

In PL, photons are used to induce excited electronic states, and the optical emission is analysed as these states relax. This method provides qualitative and, sometimes, quantitative information about chemical composition, structure and impurities.

A material gains energy by absorbing photon at some wavelength and promoting an electron from a low to a higher energy level (e.g. from valence to conduction band, - so-called electron-hole creation). After a characteristic lifetime, the excited electron returns to the ground state, releasing some energy in the form of light (radiative relaxation).

The wavelength of the emitted light can be transferred into the photon energy with the following folmula:

$$E = \frac{hc}{\lambda} = \frac{12.4 keV}{\lambda}$$

where h is the Planck's constant ($4.136 \cdot 10^{-15}$ eV·s), c = $2.998 \cdot 10^{8}$ m·s^{-1}, λ is measured in Å.

For this work, PL spectra at ambient temperature (so-called room temperature PL) were taken on a Fluorolog-3 (Horiba) with Xenon lamp (at Max-Planck-Institute for

Metal Research, Stuttgart). The samples were paced on thin quartz substrates without any fixation.

5.2.8 Electron Spin Resonance (ESR)

Electron spin resonance (ESR) is a powerful instrument for matter structure analysis. The method is used in the exploration of paramagnetic objects within various systems.

An ESR spectrum characterizes the resonant absorption of electromagnetic radiation by paramagnetic species. The condition of such absorption is the equality of the energy quantum of the monochromatic radiation with the frequency ν to the splitting $\Delta E = E_i - E_j$ of the magnetic sublevels of a system.

$$h\nu = \Delta E \qquad (1)$$

Splitting ΔE is determined by the induction of the magnetic field B and some intramolecular and intermolecular interactions.

$$\Delta E = g\beta B \qquad (2)$$

where β is Bohr magneton equal to $9.27 \cdot 10^{-24}$ J $\cdot$ T^{-1} (in the international system of units SI), g is the constant of proportionality called g-factor, g = 1 at S = 0, i.e. when there is no spin motion of an electron, and only orbital motion is present, and g = 2 if the orbital motion is absent and there is only spin motion (for example, in case of a free electron).

It is possible to get the condition (1) either by change of ν at given B, or by varying of B at a fixed ν value. In existing ESR-spectrometers, the field B is usually varied because it is significantly easier to perform technically.

The energy of magnetic sublevels E_i is, in general form, the sum of such components, as the energy of Zeeman interaction of the electrons magnetic moments with the external magnetic field, the energy of the interaction between the magnetic moments of the electrons (fine coupling) and the energy of the interaction between the magnetic moments of the electrons and nuclei (hyperfine coupling). Thus, the B value, at which the resonance (1) is reached, depends on the influence of the

surrounding of a paramagnetic unit. During the analysis of ESR-spectrum parameters, this lets draw conclusions not only about the properties of a paramagnetic center, but also about the properties of its nearest surrounding.

For this work, ESR spectra were taken on conventional X-band (9.3 GHz, Bruker ESP 300E with a Bruker ER 4102 ST resonator) or Q-band (Bruker ESP300 E EPR/ENDOR spectrometer equipped with two ESR microwave bridges: first an X-band at 9.5 GHz, and second a Q-band at 34 GHz).

5.2.9 X-ray Absorption Near Edge Structure (XANES) and High Energy Resolution Fluorescence Detected (HERFD) Spectroscopy.

In X-ray absorption spectroscopy (XAS), the coefficient of X-rays absorption of a substance is measured. Normalized absorption spectra are often called XANES. In XANES spectrum, the position of the absorption edge depends on the oxidation state of the investigated atom and thus provides information about the valency of the element. This method is also sensitive to the coordination surrounding of absorbing atoms.

X-ray absorption near-edge structure (XANES) measurements were performed at the high-brilliance XAFS–XES beamline ID26 at the European Synchrotron Radiation Facility (ESRF) in Grenoble, France. The electron energy was 6 GeV with a ring current of 170-200 mA. The incident energy was selected via a cryogenically cooled pair of Si (311) crystals. Higher harmonics were suppressed via two Si mirrors at 2.5 μrad. The spectra were recorded using an emission spectrometer with two spherically bent Si analyser crystals exploiting the (444) Bragg reflection to record the Cu $K\alpha_1$ emission line at 8.046 keV with an energy bandwidth of 0.9 eV. Recording the Cu K absorption edge (8.979 keV) by monitoring the Cu $K\alpha_1$ emission line (at 8.0492 keV) allows high energy resolution fluorescence detected (HERFD) spectra to be recorded with a reduced spectral broadening due to the core hole lifetime compared to standard XANES.[223, 224] An avalanche photodiode (APD) was used as the photon detector.

By recording the absorption spectra in HERFD mode, spectral features are recorded with reduced broadening allowing easier identification of small features, particularly in the pre-edge region, and subtle differences between similar samples are clearer to identify.

5.2.10 Gas Adsorption (BET Measurements)

Physical and chemical adsorption is a powerful method in determining the surface area and characteristic sizes of porous structures (the corresponding theory is named after S. Brunauer, P.H. Emmet, and E. Teller - BET). When a gas comes in contact with a solid surface, under suitable temperature and pressure, gas molecules will adsorb onto the surface either physically (such adsorbed molecules can be readily removed from the surface by reducing the partial pressure) or chemically (removable only by heating). For physical adsorption, the amount of gas needed to form a monolayer or to fill pores in various sizes can be measured as a function of gas pressure (the plot is called 'gas adsorption isotherm'), and this is practically useful to determine the specific surface area and pore volume in mesopores and micropores.

In the present work, BET measurements were performed on a Nova 3000e surface area and pore size analyser.

5.2.11 Sensor tests (DC measurements)

DC electrical measurements (sensor tests) were performed to monitor the sensor response of In_2O_3 to CO and H_2 in dry nitrogen. The measurements were done with a set of two In_2O_3 sensors placed symmetrically in a test chamber made of teflon and operated at the same conditions. The operating temperature of the sensors was 250 °C. The sensor response is given in the following as the resistance ratio R_{N2}/R_{gas}, where R_{gas} and R_{N2} denote the sensors' resistances in the presence and in the absence of CO/H_2, respectively. A computer driven gas-mixing system provided the analyte gas. A typical gas mixing bench consists of a combination of computer controlled mass flow controllers and computer controlled valves. Defined concentration of CO (20, 50 and 200 ppm) were obtained in the PC controlled gas mixing bench by mixing certified N_2 and CO/N_2 test gases.

Conclusions

To summarize, the major results of the present work are the template-assisted (PAOX or polycarbonate) manufacturing of Q1D nanomaterials with tailored dimensions, composition, and physical-chemical properties, as well as optimisation of routine producing of PAOX templates with the nanochannels open through from both ends. However, during the compositional analysis of templates and Q1D products, some limitations of this approach were found.

A successful attempt to alter the geometry of silicon-based ceramic nanowires by means of PAOX pore size tailoring has been made. However, diverse optical, spectral and structural characterization methods confirm the active participation of the PAOX matrix in reactions with the Si-based pre-ceramic precursors within the nanochannels and the influence on the chemical composition of the nanostructures synthesized therein. Aluminium oxide obtained during anodic oxidation of aluminium usually displays a complex composition formulated as $AlO(OH)•(H_2O)_n$. Water-free surfaces are accessible via calcination at 300 – 400 °C, but still this process leaves up to 10% of the porous surface covered with hydroxyl groups. At the same time, many organosilicon polymers are hydrolytically sensitive substances. The results of the present work show that alumina templates composed of such rich in water boehmite do react at higher temperatures with both precursors employed in this study (KiON Ceraset polyureasilazane and polycarbosilane SP Matrix Polymer) to form one dimensional SiO(N)C materials. Under high temperature conditions PAOX templates are even further reactive towards these Si based ceramic precursors. The results of the investigations will certainly have a practical importance for the design of further PAOX template-based experiments and shed new light on the chemical reactivity of widely used PAOX templates as structure directing matrix and as reaction partner in solid state reactions. The sensitivity of the infiltrated precursors with respect to its oxidative behaviour has thus to be taken into account in order to apply alumina templates successfully for the synthesis of non-oxide nanostructures. The release of water at high temperatures, the reactivity of residual hydroxyl groups, as well as the phase transitions of alumina restricts the utilization of alumina templates in the fabrication of non-oxide systems. In the case of the present experiments the ceramization of the precursor occurs at 1000 °C and in the common temperature range up to 1000 °C the precursors are oxidable. We have shown that

oxygen was introduced at low temperature into the SiCN and SiC precursors and SiO(N)C nanowires are formed in PAOX templates during pyrolysis. Thus, it can be concluded that PAOX is not innocent, just structure directing template under high temperature conditions, however it has significant impact on the reaction chemistry under such conditions.

Solutions of the oximato precursor complexes of Zn, Mn, Mg, Cu, In can be successively used for the synthesis of polycrystalline Q1D structures via the impregnation into polymeric templates.

The magnesium (II) oximato complex has proved itself to be a suitable precursor for the synthesis of nanoscale Q1D MgO structures. Its decomposition reaction is straightforward and the final ceramisation occurs at relatively low temperature (starting above 190 °C), while already at temperatures around 160° C formation of a dehydrated pre-ceramic green body takes place. Polycrystalline MgO can be obtained in a further step by calcination up to 450 °C. Polycarbonate membranes were used for the first time for the synthesis of MgO nanostructures by means of thermal conversion. The ease of removal of polymer templates by dissolution in organic solvents or combustion makes them an interesting alternative as template for porous alumina or silica mebranes in the synthesis of Q1D inorganic ceramics.

In_2O_3 nanotubes were successfully made via template based approach. Indium complexes with oximato ligands were suitable precursors for the synthesis, the decomposition reaction and transition into inorganic components occurs at relatively low temperature (350 °C). The polycrystalline nanotubes were easily accessible by immersion of track-etched polymer membranes into the precursor solution and removal of polymer templates by dissolution in organic solvent. The resulting material consists of indium oxide crystals with slightly hydroxylated surface. Spectroscopic investigations showed practical absence of organic rests. Nanotubes are not entire and are composed of smaller nanoparticles. They combine optimal grain size and a high accessible surface like most of the superior state-of-the-art gas sensors do. Sensors tests showed the superior performance of the nanotubes to that of the unformed Q0D particles, synthesised from the same parent material. The templated nanostructures approved themselves a promising material for gas sensitive devices.

Plain and Mn-doped ZnO nanorods were synthesized at a low temperature around 160-180 °C. This prevents phase separation and favours uniform distribution of Mn

ions in the ZnO lattice. According to the analysis, manganese ions have only oxidation state +II and can be distributed within the ZnO matrix, adsorbed on ZnO grains surface, or form manganese-related small clusters.

The novel approach to the synthesis of Cu-doped ZnO resulted in homogeneously distributed copper ions in ZnO matrix. The analysis methods point to the oxidation state +II, the photoluminescent spectra show systematic narrowing of the band gap with the Cu-doping concentration increase. The advantage of the presented template-based assembly is that different morphologies of the material are accessible in future prospects, depending on the substrate geometry – films, nanorods or nanowires, or spherical particles, which may be important for further design of nanoelectronic devices.

Results of the additional experiments show that there are new possibilities of further optimisation of PAOX templates morphology, chemical modification of its surface, of fabrication of novel multi-component superlattice structures, as well as provide a better understanding of the template influence on the process of different pre-ceramic precursors thermal conversion.

Zusammenfassung

Die Hauptergebnisse der vorliegenden Arbeit sind die Optimierung der PAOX-assistierten Herstellung von Q1D-Materialien definierter Größe, Zusammensetzung und physikalisch-chemischen Eigenschaften sowie die Herstellung der PAOX-Template mit beidseitig geöffneten Nanokanälen. Auch konnten die Grenzen dieser Herangehensweise, bezüglich der Zusammensetzung der Template und Q1D-Produkte, gezeigt werden. Durch Anpassungen der PAOX-Porengröße konnten die Geometrien von keramischen Nanodrähten auf Si-Basis gezielt verändert werden. Weitgefächerte optische, spektrale und strukturelle Charakterisierungen zeigten, dass die PAOX-Matrix aktiv an der Reaktion der Si-basierten keramischen Precursoren (Vorläufersubstanzen) in den Nanokanälen teilnimmt und die chemische Zusammensetzung der Produkte beeinflusst. Aluminiumoxid/-hydroxid, welches durch anodische Oxidation von Aluminiummetall erhalten wurde, zeigt gewöhnlich eine komplexe Zusammensetzung und lässt sich durch die Formel $AlO(OH)\cdot(H_2O)n$ beschreiben. Eine weitgehend wasserfreie Oberfläche wird durch Calcinierung bei 300-400°C erhalten, wobei allerdings 10% der Porenoberfläche mit OH-Gruppen bedeckt bleibt. Allerdings sind jedoch viele Organo-Silicium-Verbindungen hydrolyseempfindlich und es kann zu ungewünschten Nebenreaktionen kommen. Die vorgestellten Ergebnisse belegen, dass Aluminiumoxid-Template aus wasserreichem Böhemit mit beiden in der Arbeit eingesetzten Precursoren (KiON Ceraset Polyharnstoffsilazane und Polycarbosilane SP Matrix Polymer) reagieren und eindimensionale SiO(N)C-Materialien formen. Bei hohen Temperaturen zeigen die PAOX-Template auch Reaktivität gegenüber den Si-basierten pre-keramischen Precursoren. Auch wird neues Licht auf die chemische Reaktivität der vielgebrauchten PAOX-Template als strukturdirigierende Matrix und als Reaktionspartner in Festkörperreaktionen geworfen. Die Empfindlichkeit der einzubringenden Precursoren, bezüglich ihres Oxidationsverhaltens, muss natürlich beachtet werden, wenn Al_2O_3-Template bei der Synthese von Oxid-freien Nanostrukturen genutzt werden sollen. Die Wasserfreisetzung bei höheren Temperaturen, die Reaktivität der verbleibenden OH-Gruppen sowie Phasenübergänge im Al_2O_3 begrenzen jedoch den Einsatz dieser Template bei der Darstellung Oxid-freier Systeme. Im Fall der vorliegenden Experimente werden die Precursoren bei 1000°C keramisiert, wobei sie in diesem Temperaturbereich

oxidierbar sind. Wir haben gezeigt, dass in den PAOX-Templaten während der Pyrolyse bei niedrigen Temperaturen Sauerstoff in die SiCN/SiC-Precursoren eingebaut wird und es somit zur Bildung von SiO(N)C-Nanodrähten kommt. Es kann daher geschlussfolgert werden, dass PAOX nicht unschuldig ist, sondern bei hohen Temperaturen ein strukturgebendes Templat ist und damit Einfluss auf die ablaufenden chemischen Reaktionen hat.

Zn, Mn, Mg, Cu, In Oximat-Precursor-Lösungen können erfolgreich für die Synthese von polykristallinen Q1D Strukturen, via Imprägnierung polymerer Template, genutzt werden.

Der Mg-Oximat-Komplex hat sich als geeigneter Precursor für die Synthese von nanostrukturierten Q1D MgO erwiesen. Die Zersetzung verläuft direkt und die Keramisierung beginnt bei relativ niedriger Temperatur (190 °C), wobei schon ab 160°C die Bildung eines dehydrierten pre-keramischen Grünkörpers erfolgt. Polykristallienes MgO wird in einem folgenden Calcinierungsschritt bei 450°C erhalten. Erstmalig wurden Polycarbonat-Membranen für die Synthese von MgO durch thermische Überführung genutzt. Das einfache Entfernen der polymeren Template, durch auflösen in organischen Lösungsmitteln oder Verbrennung, macht diese Methode für die Herstellung anorganischer Q1D-Keramiken zu einer interessanten Alternative gegenüber Al_2O_3 bzw. SiO_2-Membranen.

In_2O_3-Nanoröhren wurden über den Templat-basierten Zugang erfolgreich hergestellt, wobei sich In-Oximat-Komplexe als geeignete Precursoren für die Synthese erwiesen. Die Zersetzung, sowie die Überführung in eine anorganische Keramik erfolgen bei relativ niedrigen Temperaturen (350°C). Die polykristallinen Nanoröhren waren leicht zugänglich. Hierzu wurden die „track-etched“-Membranen in die Precursorlösung getaucht und das Polymertemplat anschließend durch ein organisches Lösungsmittel entfernt. Die erhaltenen In_2O_3-Kristalle hatten nur wenige OH-Gruppen auf der Oberfläche, wobei spektroskopische Untersuchungen für die Abwesenheit von organischen Resten sprechen und die Nanoröhren aus mehreren einzelnen Nanopartikeln zusammengesetzt waren. Die Nanoröhren vereinen optimale Partikelgröße, sowie eine sehr gut zugängliche Oberfläche, wie es bei den derzeitig hochwertigen Gassensoren der Fall ist. In Sensortests zeigten sich die Nanoröhren den entsprechenden Pulvern als überlegen und sind somit ein vielversprechendes Material für Gassensoren.

Reine, sowie Mn-dotierte, ZnO-Nanostäbe wurden bei niedrigen Temperaturen (160-180°C) synthetisiert. Bei den Mn-dotierten Nanostäben wurde durch die niedrigen Temperaturen einer Phasentrennung vorgebeugt und eine einheitliche Verteilung der Mn-Ionen im ZnO-Gitter begünstigt. Gemäß den Analysen liegen die Mn-Ionen ausschließlich zweiwertig vor, sind in der ZnO-Matrix verteilt, an den ZnO-Partikeln gebunden oder als Mn(reiche)-Cluster gebunden. Ein neuartiger Syntheseweg für Cu-dotiertes ZnO resultierte in einer homogenen Verteilung der Cu-Ionen in der ZnO-Matrix. Die Analysen deuten auf Cu in der Oxidationsstufe (+2) hin; die Photoluminiszensspektren zeigen eine systematische Verengung der Bandlücke mit zunehmenden Cu-Gehalt. Der Vorteil des gezeigten Templat-basierten Synthesewegs ist, dass unterschiedliche Materialmorphologien, abhängig von der Substratgeometrie, in Zukünft zugänglich sind. Dies können Filme, Nanostäbe, Nanodrähte oder auch sphärische Partikel sein.

Die in der Arbeit vorgestellten zusatzlichen Experimente zeigen, dass sich bei einer weiteren Optimierung der PAOX-Templatmorphologie, der chemischen Oberflächenmodifizierung, der Herstellung von Mehrkomponenten-Hybrid Materialien neue Wege eröffnen. Hierdurch erhält man ein besseres Verständnis des Templat-Einflusses auf verschiedene keramische Precursoren und deren thermische Umwandlung.

References

[1] G. Z. Cao, *Nanostructures and Nanomaterials, Synthesis Properties and Applications*, Imperial College Press, London, **2004**.

[2] C. N. R. Rao, G. U. Kulkarni, P. J. Thomas, P. P. Edwards, *Chemistry-a European Journal* **2002**, *8*, 29.

[3] G. Z. Cao, *Journal of Physical Chemistry B* **2004**, *108*, 19921.

[4] A. J. Mieszawska, R. Jalilian, G. U. Sumanasekera, F. P. Zamborini, *Small* **2007**, *3*, 722.

[5] J. C. Hulteen, C. R. Martin, *Journal of Materials Chemistry* **1997**, *7*, 1075.

[6] T. L. Wade, J. E. Wegrowe, *European Physical Journal-Applied Physics* **2005**, *29*, 3.

[7] R. L. Rice, D. C. Arnold, M. T. Shaw, D. Iacopina, A. J. Quinn, H. Amenitsch, J. D. Holmes, M. A. Morris, *Advanced Functional Materials* **2007**, *17*, 133.

[8] C. T. Kresge, J. C. Vartuli, W. J. Roth, M. E. Leonowicz, J. S. Beck, K. D. Schmitt, C. T. W. Chu, D. H. Olson, E. W. Sheppard, S. B. McCullen, J. B. Higgins, J. L. Schlenker, *Science and Technology in Catalysis 1994* **1995**, *92*, 11.

[9] J. S. Beck, J. C. Vartuli, W. J. Roth, M. E. Leonowicz, C. T. Kresge, K. D. Schmitt, C. T. W. Chu, D. H. Olson, E. W. Sheppard, S. B. Mccullen, J. B. Higgins, J. L. Schlenker, *Journal of the American Chemical Society* **1992**, *114*, 10834.

[10] H. F. Yang, D. Y. Zhao, *Journal of Materials Chemistry* **2005**, *15*, 1217.

[11] J. J. Schneider, R. C. Hoffmann, J. Engstler, S. Dilfer, A. Klyszcz, E. Erdem, P. Jakes, R. A. Eichel, *Journal of Materials Chemistry* **2009**, *19*, 1449.

[12] G. D. Bengough, J. M. Stuart, patent 23 994, UK, **1923**.

[13] *Anodic Oxidation of Aluminium and its Alloys*, in *Information Bulletin, Vol. 14*, The Aluminium Development Association, London, **1947**.

[14] E. Stoyanova, S. Takeva, Z. Kostov, D. Stoychev, *Transactions of the Institute of Metal Finishing* **2004**, *82*, 157.

[15] K. Nielsch, F. Muller, A. P. Li, U. Gosele, *Advanced Materials* **2000**, *12*, 582.

[16] J. W. Diggle, T. C. Downie, C. W. Goulding, *Journal of Electroanalytical Chemistry* **1968**, *18*, 192.

[17] V. Sadasivan, C. P. Richter, L. Menon, P. F. Williams, *Aiche Journal* **2005**, *51*, 649.

[18] F. Keller, M. S. Hunter, D. L. Robinson, *Journal of the Electrochemical Society* **1953**, *100*, 411.

[19] J. P. O'Sullivan, G. C. Wood, *Proceedings of the Royal Society of London Series a-Mathematical and Physical Sciences* **1970**, *317*, 511.

[20] G. E. Thompson, R. C. Furneaux, G. C. Wood, J. A. Richardson, J. S. Goode, *Nature* **1978**, *272*, 433.

[21] G. E. Thompson, G. C. Wood, in *Treatise on Materials Science and Technology Vol. 23: Corrosion: Aqueous Process and Passive Films, Vol. 5* (Ed.: J. C. Scully), Academic Press Inc., New York, **1983**, pp. 205.

[22] G. E. Thompson, *Thin Solid Films* **1997**, *297*, 192.

[23] F. Brown, Mackinto.Wd, *Journal of the Electrochemical Society* **1973**, *120*, 1096.

[24] K. Shimizu, K. Kobayashi, G. E. Thompson, G. C. Wood, *Journal of Applied Electrochemistry* **1985**, *15*, 781.

[25] F. Y. Li, L. Zhang, R. M. Metzger, *Chemistry of Materials* **1998**, *10*, 2470.

[26] H. Masuda, K. Fukuda, *Science* **1995**, *268*, 1466.

[27] H. Masuda, F. Hasegwa, S. Ono, *Journal of the Electrochemical Society* **1997**, *144*, L127.

[28] H. Masuda, H. Yamada, M. Satoh, H. Asoh, M. Nakao, T. Tamamura, *Applied Physics Letters* **1997**, *71*, 2770.

[29] H. Masuda, K. Yada, A. Osaka, *Japanese Journal of Applied Physics Part 2-Letters* **1998**, *37*, L1340.

[30] H. Masuda, K. Takenaka, T. Ishii, K. Nishio, *Japanese Journal of Applied Physics Part 2-Letters & Express Letters* **2006**, *45*, L1165.

[31] Y. Matsui, K. Nishio, H. Masuda, *Small* **2006**, *2*, 522.

[32] S. Z. Chu, K. Wada, S. Inoue, S. Todoroki, Y. K. Takahashi, K. Hono, *Chemistry of Materials* **2002**, *14*, 4595.

[33] X. Y. Zhang, L. D. Zhang, M. J. Zheng, G. H. Li, L. X. Zhao, *Journal of Crystal Growth* **2001**, *223*, 306.

[34] A. P. Li, F. Muller, A. Birner, K. Nielsch, U. Gosele, *Journal of Applied Physics* **1998**, *84*, 6023.

[35] X. Y. Zhang, L. D. Zhang, G. H. Li, L. X. Zhao, *Materials Science and Engineering a-Structural Materials Properties Microstructure and Processing* **2001**, *308*, 9.

[36] O. Jessensky, F. Muller, U. Gosele, *Applied Physics Letters* **1998**, *72*, 1173.

[37] C. X. Xu, Q. H. Xue, Y. Zhong, Y. P. Cui, L. Ba, B. Zhao, N. Gu, *Nanotechnology* **2002**, *13*, 47.

[38] J. C. Bao, Z. Xu, *Chinese Journal of Inorganic Chemistry* **2002**, *18*, 965.

[39] F. H. Kaatz, M. P. Siegal, D. L. Overmyer, P. P. Provencio, J. L. Jackson, *Materials Science & Engineering C-Biomimetic and Supramolecular Systems* **2003**, *23*, 141.

[40] P. Apel, *Radiation Measurements* **2001**, *34*, 559.

[41] C. R. Martin, L. S. Vandyke, Z. H. Cai, W. B. Liang, *Journal of the American Chemical Society* **1990**, *112*, 8976.

[42] C. J. Brumlik, V. P. Menon, C. R. Martin, *Journal of Materials Research* **1994**, *9*, 1174.

[43] C. Schonenberger, B. M. I. vanderZande, L. G. J. Fokkink, M. Henny, C. Schmid, M. Kruger, A. Bachtold, R. Huber, H. Birk, U. Staufer, *Journal of Physical Chemistry B* **1997**, *101*, 5497.

[44] A. Davis, J. H. Golden, *Journal of the Chemical Society B-Physical Organic* **1968**, 45.

[45] L. Becker, D. Lenoir, G. Matuschek, A. Kettrup, *Journal of Analytical and Applied Pyrolysis* **2001**, *60*, 55.

[46] K. L. Erickson, *Journal of Thermal Analysis and Calorimetry* **2007**, *89*, 427.

[47] X. G. Li, M. R. Huang, *Polymer International* **1999**, *48*, 387.

[48] T. H. Yoon, H. J. Lee, J. Yan, D. P. Kim, *Journal of the Ceramic Society of Japan* **2006**, *114*, 473.

[49] Q. M. Cheng, L. V. Interrante, M. Lienhard, Q. H. Shen, Z. Z. Wu, *Journal of the European Ceramic Society* **2005**, *25*, 233.

[50] H. Wang, S. Y. Zheng, X. D. Li, D. P. Kim, *Microporous and Mesoporous Materials* **2005**, *80*, 357.

[51] H. Wang, X. D. Li, T. S. Kim, D. P. Kim, *Applied Physics Letters* **2005**, *86*.

[52] M. Mehregany, C. A. Zorman, S. Roy, A. J. Fleischman, C. H. Wu, N. Rajan, *International Materials Reviews* **2000**, *45*, 85.

[53] Y. Ryu, B. Park, Y. Song, K. J. Yong, *Journal of Crystal Growth* **2004**, *271*, 99.

[54] W. M. Zhou, X. Liu, Y. F. Zhang, *Applied Physics Letters* **2006**, *89*.

[55] K. W. Wong, X. T. Zhou, F. C. K. Au, H. L. Lai, C. S. Lee, S. T. Lee, *Applied Physics Letters* **1999**, *75*, 2918.

[56] G. W. Meng, L. D. Zhang, C. M. Mo, S. Y. Zhang, Y. Qin, S. P. Feng, H. J. Li, *Journal of Materials Research* **1998**, *13*, 2533.

[57] Z. W. Pan, H. L. Lai, F. C. K. Au, X. F. Duan, W. Y. Zhou, W. S. Shi, N. Wang, C. S. Lee, N. B. Wong, S. T. Lee, S. S. Xie, *Advanced Materials* **2000**, *12*, 1186.

[58] M. Zhang, Y. Bando, K. Wada, *Journal of Materials Research* **2000**, *15*, 387.

[59] B. Yao, D. Fleming, M. A. Morris, S. E. Lawrence, *Chemistry of Materials* **2004**, *16*, 4851.

[60] W. Y. Yang, Z. P. Xie, J. J. Li, H. Z. Miao, L. G. Zhang, L. N. An, *Solid State Communications* **2004**, *132*, 263.

[61] J. J. Schneider, J. Engstler, in *Ceramics Science and Technology, Vol. 1* (Eds.: R. Riedel, I.-W. Chen), Wiley-VCH, Weinheim, Germany, **2008**, pp. 297.

[62] R. Riedel, G. Mera, R. Hauser, A. Klonczynski, *Journal of the Ceramic Society of Japan* **2006**, *114*, 425.

[63] L. Majoli, A. Evstratov, J. M. Guillot, J. F. Chapat, J. L. Le Loarer, *Journal of Analytical and Applied Pyrolysis* **2005**, *74*, 290.

[64] G. Gorokh, A. Mozalev, D. Solovei, V. Khatko, E. Llobet, X. Correig, *Electrochimica Acta* **2006**, *52*, 1771.

[65] L. H. Little, *Infrared Spectra of Adsorbed Species*, Academic Press, London, New York, **1966**.

[66] G. W. Wagner, P. W. Bartram, O. Koper, K. J. Klabunde, *Journal of Physical Chemistry B* **1999**, *103*, 3225.

[67] G. Pacchioni, T. Minerva, *Surface Science* **1992**, *275*, 450.

[68] S. H. C. Liang, I. D. Gay, *Langmuir* **1985**, *1*, 593.

[69] N. Takezawa, H. Kobayashi, *Journal of Catalysis* **1982**, *73*, 120.

[70] S. L. Parrott, J. W. Rogers, J. M. White, *Applied Surface Science* **1978**, *1*, 443.

[71] I. D. Gay, *Journal of Physical Chemistry* **1980**, *84*, 3230.

[72] N. Takezawa, C. Hanamaki, H. Kobayashi, *Journal of Catalysis* **1975**, *38*, 101.

[73] S. H. C. Liang, I. D. Gay, *Journal of Catalysis* **1986**, *101*, 293.

[74] S. Zhang, F. Y. Cheng, Z. L. Tao, F. Gao, J. Chen, *Journal of Alloys and Compounds* **2006**, *426*, 281.

[75] P. D. Yang, C. M. Lieber, *Science* **1996**, *273*, 1836.

[76] Z. Cui, G. W. Meng, W. D. Huang, G. Z. Wang, L. D. Zhang, *Materials Research Bulletin* **2000**, *35*, 1653.

[77] H. S. Jung, J. K. Lee, M. Nastasi, S. W. Lee, J. Y. Kim, J. S. Park, K. S. Hong, H. Shin, *Langmuir* **2005**, *21*, 10332.

[78] B. Luo, J. W. Johnson, J. Kim, R. M. Mehandru, F. Ren, B. P. Gila, A. H. Onstine, C. R. Abernathy, S. J. Pearton, A. G. Baca, R. D. Briggs, R. J. Shul, C. Monier, J. Han, *Applied Physics Letters* **2002**, *80*, 1661.

[79] Y. B. Li, Y. Bando, D. Golberg, Z. W. Liu, *Applied Physics Letters* **2003**, *83*, 999.

[80] M. C. Gallagher, M. S. Fyfield, J. P. Cowin, S. A. Joyce, *Surface Science* **1995**, *339*, L909.

[81] C. Bondoux, P. Prene, P. Belleville, F. Guillet, S. Lambert, B. Minot, R. Jerisian, *Journal of the European Ceramic Society* **2005**, *25*, 2795.

[82] A. Bhargava, J. A. Alarco, I. D. R. Mackinnon, D. Page, A. Ilyushechkin, *Materials Letters* **1998**, *34*, 133.

[83] J. T. Hu, K. Kurumada, M. Tanigaki, *Journal of Non-Crystalline Solids* **2003**, *325*, 124.

[84] G. B. Sergeev, *Nanochemistry*, Elsevier B. V., Amsterdam, **2006**.

[85] H. W. Kim, S. H. Shim, *Advanced Engineering Materials* **2007**, *9*, 92.

[86] L. Yan, J. Zhuang, X. M. Sun, Z. X. Deng, Y. D. Li, *Materials Chemistry and Physics* **2002**, *76*, 119.

[87] J. Zhang, L. Zhang, X. Peng, X. Wang, *Applied Physics a-Materials Science & Processing* **2001**, *73*, 773.

[88] Q. Wei, C. M. Lieber, *Nanophase and Nanocomposite Materials Iii* **2000**, *581*, 3.

[89] C. C. Tang, Y. Bando, T. Sato, *Journal of Physical Chemistry B* **2002**, *106*, 7449.

[90] Y. G. Yan, L. X. Zhou, J. Zhang, H. B. Zeng, Y. Zhang, L. D. Zhang, *Journal of Physical Chemistry C* **2008**, *112*, 10412.

[91] M. Zhao, X. L. Chen, W. J. Wang, Y. J. Ma, Y. P. Xu, H. Z. Zhao, *Materials Letters* **2006**, *60*, 2017.

[92] K. Nagashima, T. Yanagida, H. Tanaka, T. Kawai, *Journal of Applied Physics* **2007**, *101*.

[93] H. W. Kim, M. H. Kong, J. H. Yang, *Acta Physica Polonica A* **2008**, *113*, 1021.

[94] H. B. Lu, L. Liao, H. Li, D. F. Wang, Y. Tian, J. C. Li, Q. Fu, B. P. Zhu, Y. Wu, *European Journal of Inorganic Chemistry* **2008**, 2727.

[95] H. J. Fan, M. Knez, R. Scholz, K. Nielsch, E. Pippel, D. Hesse, U. Gosele, M. Zacharias, *Nanotechnology* **2006**, *17*, 5157.

[96] M. J. Madou, S. R. Morrison, *Chemical Sensing with Solid State Devices*, Academic Press, San Diego, **1989**.

[97] D. Kohl, *Journal of Physics D-Applied Physics* **2001**, *34*, R125.

[98] A. Gurlo, M. Sahm, A. Oprea, N. Barsan, U. Weimar, *Sensors and Actuators B-Chemical* **2004**, *102*, 291.

[99] G. Eranna, B. C. Joshi, D. P. Runthala, R. P. Gupta, *Critical Reviews in Solid State and Materials Sciences* **2004**, *29*, 111.

[100] A. Oprea, A. Gurlo, N. Barsan, U. Weimar, *Sensors and Actuators B-Chemical* **2009**, *139*, 322.

[101] G. Korotcenkov, M. Ivanov, I. Blinov, J. R. Stetter, *Thin Solid Films* **2007**, *515*, 3987.

[102] C. S. Rout, K. Ganesh, A. Govindaraj, C. N. R. Rao, *Applied Physics a-Materials Science & Processing* **2006**, *85*, 241.

[103] A. Gurlo, M. Ivanovskaya, N. Barsan, U. Weimar, *Inorganic Chemistry Communications* **2003**, *6*, 569.

[104] M. Epifani, E. Comini, J. Arbiol, R. Diaz, N. Sergent, T. Pagnier, P. Siciliano, G. Faglia, J. R. Morante, *Sensors and Actuators B-Chemical* **2008**, *130*, 483.

[105] V. V. Sysoev, B. K. Button, K. Wepsiec, S. Dmitriev, A. Kolmakov, *Nano Letters* **2006**, *6*, 1584.

[106] D. Sanders, U. Simon, *Journal of Combinatorial Chemistry* **2007**, *9*, 53.

[107] T. Waitz, T. Wagner, T. Sauerwald, C. D. Kohl, M. Tiemann, *Advanced Functional Materials* **2009**, *19*, 653.

[108] T. Wagner, T. Sauerwald, C. D. Kohl, T. Waitz, C. Weidmann, M. Tiemann, *Thin Solid Films* **2009**, *517*, 6170.

[109] Z. M. Zeng, K. Wang, Z. X. Zhang, J. J. Chen, W. L. Zhou, *Nanotechnology* **2009**, *20*.

[110] K. Yao, D. Caruntu, Z. M. Zeng, J. J. Chen, C. J. O'Connor, W. L. Zhou, *Journal of Physical Chemistry C* **2009**, *113*, 14812.

[111] *Metal Oxides: Chemistry and Applications*, Fierro, J. L. G. ed., Taylor & Francis Group, Boka Raton, London, New York, **2006**.

[112] K. I. Choi, H. R. Kim, J. H. Lee, *Sensors and Actuators B-Chemical* **2009**, *138*, 497.

[113] D. Lutic, M. Strand, A. Lloyd-Spetz, K. Buchholt, E. Ieva, P. O. Kall, M. Sanati, *Topics in Catalysis* **2007**, *45*, 105.

[114] A. Kolmakov, M. Moskovits, *Annual Review of Materials Research* **2004**, *34*, 151.

[115] G. Cheng, E. Stern, S. Guthrie, M. A. Reed, R. Klie, Y. Hao, G. Meng, L. Zhang, *Applied Physics a-Materials Science & Processing* **2006**, *85*, 233.

[116] E. Comini, C. Baratto, G. Faglia, M. Ferroni, A. Vomiero, G. Sberveglieri, *Progress in Materials Science* **2009**, *54*, 1.

[117] D. Calestani, M. Z. Zha, A. Zappettini, L. Lazzarini, L. Zanotti, *Chemical Physics Letters* **2007**, *445*, 251.

[118] C. J. Chen, W. L. Xu, M. Y. Chern, *Advanced Materials* **2007**, *19*, 3012.

[119] A. Qurashi, E. M. El-Maghraby, T. Yamazaki, Y. Shen, T. Kikuta, *Journal of Alloys and Compounds* **2009**, *481*, L35.

[120] Z. X. Cheng, X. B. Dong, Q. Y. Pan, J. C. Zhang, X. W. Dong, *Materials Letters* **2006**, *60*, 3137.

[121] S. C. Chang, M. H. Huang, *Journal of Physical Chemistry C* **2008**, *112*, 2304.

[122] C. Y. Kuo, S. Y. Lu, T. Y. Wei, *Journal of Crystal Growth* **2005**, *285*, 400.

[123] H. Q. Cao, X. Q. Qiu, Y. Liang, Q. M. Zhu, M. J. Zhao, *Applied Physics Letters* **2003**, *83*, 761.

[124] K. H. Wu, S. Y. Lu, *Electrochemical and Solid State Letters* **2005**, *8*, D9.

[125] Z. D. Xiao, L. D. Zhang, X. K. Tian, X. S. Fang, *Nanotechnology* **2005**, *16*, 2647.

[126] M. Zhong, M. J. Zheng, L. Ma, Y. B. Li, *Nanotechnology* **2007**, *18*.

[127] D. H. Kuo, C. W. Hsu, C. H. Liang, *Journal of the Electrochemical Society* **2008**, *155*, K156.

[128] X. P. Shen, H. J. Liu, X. Fan, Y. Jiang, J. M. Hong, Z. Xu, *Journal of Crystal Growth* **2005**, *276*, 471.

[129] B. Cheng, E. T. Samulski, *Journal of Materials Chemistry* **2001**, *11*, 2901.

[130] M. J. Zheng, L. D. Zhang, G. H. Li, X. Y. Zhang, X. F. Wang, *Applied Physics Letters* **2001**, *79*, 839.

[131] M. Willander, O. Nur, Q. X. Zhao, L. L. Yang, M. Lorenz, B. Q. Cao, J. Z. Perez, C. Czekalla, G. Zimmermann, M. Grundmann, A. Bakin, A. Behrends, M. Al-Suleiman, A. El-Shaer, A. C. Mofor, B. Postels, A. Waag, N. Boukos, A. Travlos, H. S. Kwack, J. Guinard, D. L. Dang, *Nanotechnology* **2009**, *20*.

[132] Y. Lei, Z. Jiao, M. H. Wu, G. Wilde, *Advanced Engineering Materials* **2007**, *9*, 343.

[133] W. Chen, L. F. Zhao, Y. Q. Wang, J. H. Miao, S. Liu, Z. C. Xia, S. L. Yuan, *Solid State Communications* **2005**, *134*, 827.

[134] P. Sharma, A. Gupta, K. V. Rao, F. J. Owens, R. Sharma, R. Ahuja, J. M. O. Guillen, B. Johansson, G. A. Gehring, *Nature Materials* **2003**, *2*, 673.

[135] X. P. Shen, A. H. Yuan, Y. M. Hu, Y. Jiang, Z. Xu, Z. Hu, *Nanotechnology* **2005**, *16*, 2039.

[136] J. M. Baik, J. L. Lee, *Advanced Materials* **2005**, *17*, 2745.

[137] C. Min, X. Shen, W. Sheng, *Applied Physics a-Materials Science & Processing* **2009**, *96*, 799.

[138] L. Xu, Y. L. Hu, C. Pelligra, C. H. Chen, L. Jin, H. Huang, S. Sithambaram, M. Aindow, R. Joesten, S. L. Suib, *Chemistry of Materials* **2009**, *21*, 2875.

[139] Y. Hara, J. Brownson, M. Anderson, *Physica Status Solidi a-Applications and Materials Science* **2009**, *206*, 711.

[140] G. Clavel, M. G. Willinger, D. Zitoun, N. Pinna, *Advanced Functional Materials* **2007**, *17*, 3159.

[141] T. L. Phan, R. Vincent, D. Cherns, N. X. Nghia, V. V. Ursaki, *Nanotechnology* **2008**, *19*.

[142] Y. Guo, X. B. Cao, X. M. Lan, C. Zhao, X. D. Xue, Y. Y. Song, *Journal of Physical Chemistry C* **2008**, *112*, 8832.

[143] B. B. Lakshmi, C. J. Patrissi, C. R. Martin, *Chemistry of Materials* **1997**, *9*, 2544.

[144] G. S. Wu, T. Xie, X. Y. Yuan, Y. Li, L. Yang, Y. H. Xiao, L. D. Zhang, *Solid State Communications* **2005**, *134*, 485.

[145] Y. H. Xiao, L. Li, Y. Li, M. Fang, L. D. Zhang, *Nanotechnology* **2005**, *16*, 671.

[146] Y. Li, G. W. Meng, L. D. Zhang, F. Phillipp, *Applied Physics Letters* **2000**, *76*, 2011.

[147] Q. T. Wang, G. Z. Wang, B. Xu, J. S. Jie, X. H. Han, G. P. Li, Q. S. Li, J. G. Hou, *Materials Letters* **2005**, *59*, 1378.

[148] F. J. Owens, *Journal of Magnetism and Magnetic Materials* **2009**, *321*, 3734.

[149] M. Shuai, L. Liao, H. B. Lu, L. Zhang, J. C. Li, D. J. Fu, *Journal of Physics D-Applied Physics* **2008**, *41*.

[150] T. S. Herng, S. P. Lau, S. F. Yu, S. H. Tsang, K. S. Teng, J. S. Chen, *Journal of Applied Physics* **2008**, *104*.

[151] D. B. Buchholz, R. P. H. Chang, J. H. Song, J. B. Ketterson, *Applied Physics Letters* **2005**, *87*.

[152] K. S. Ahn, T. Deutsch, Y. Yan, C. S. Jiang, C. L. Perkins, J. Turner, M. Al-Jassim, *Journal of Applied Physics* **2007**, *102*.

[153] T. Ghosh, M. Dutta, S. Mridha, D. Basak, *Journal of the Electrochemical Society* **2009**, *156*, H285.

[154] T. Ghosh, D. Basak, *Journal of Physics D-Applied Physics* **2009**, *42*.

[155] Y. Y. Wei, D. L. Hou, S. Qiao, C. M. Zhen, G. D. Tang, *Physica B-Condensed Matter* **2009**, *404*, 2486.

[156] Y. S. Sonawane, K. G. Kanade, B. B. Kale, R. C. Aiyer, *Materials Research Bulletin* **2008**, *43*, 2719.

[157] H. C. Zhu, J. Iqbal, H. J. Xu, D. P. Yu, *Journal of Chemical Physics* **2008**, *129*.

[158] G. H. Kim, D. L. Kim, B. D. Ahn, S. Y. Lee, H. J. Kim, *Microelectronics Journal* **2009**, *40*, 272.

[159] X. B. Wang, D. M. Li, F. Zeng, F. Pan, *Journal of Physics D-Applied Physics* **2005**, *38*, 4104.

[160] Q. Ma, D. B. Buchholz, R. P. H. Chang, *Physical Review B* **2008**, *78*.

[161] G. Z. Xing, J. G. Tao, G. P. Li, Z. Zhang, L. M. Wong, S. J. Wang, C. H. A. Huan, T. Wu, *2008 2nd Ieee International Nanoelectronics Conference, Vols 1-3* **2008**, 462.

[162] N. Kouklin, *Advanced Materials* **2008**, *20*, 2190.

[163] G. Z. Xing, J. B. Yi, J. G. Tao, T. Liu, L. M. Wong, Z. Zhang, G. P. Li, S. J. Wang, J. Ding, T. C. Sum, C. H. A. Huan, T. Wu, *Advanced Materials* **2008**, *20*, 3521.

[164] Z. Zhang, J. B. Yi, J. Ding, L. M. Wong, H. L. Seng, S. J. Wang, J. G. Tao, G. P. Li, G. Z. Xing, T. C. Sum, C. H. A. Huan, T. Wu, *Journal of Physical Chemistry C* **2008**, *112*, 9579.

[165] D. Q. Gao, D. S. Xue, Y. Xu, Z. J. Yan, Z. H. Zhang, *Electrochimica Acta* **2009**, *54*, 2392.

[166] D. A. Brevnov, G. V. R. Rao, G. P. Lopez, P. B. Atanassov, *Electrochimica Acta* **2004**, *49*, 2487.

[167] H. Masuda, M. Satoh, *Japanese Journal of Applied Physics Part 2-Letters* **1996**, *35*, L126.

[168] T. T. Xu, R. D. Piner, R. S. Ruoff, *Langmuir* **2003**, *19*, 1443.

[169] M. E. Mata-Zamora, J. M. Saniger, *Revista Mexicana De Fisica* **2005**, *51*, 502.

[170] J. Randon, P. P. Mardilovich, A. N. Govyadinov, R. Paterson, *Journal of Colloid and Interface Science* **1995**, *169*, 335.

[171] J. J. Schneider, N. Engstler, K. P. Budna, C. Teichert, S. Franzka, *European Journal of Inorganic Chemistry* **2005**, 2352.

[172] T. T. Xu, F. T. Fisher, L. C. Brinson, R. S. Ruoff, *Nano Letters* **2003**, *3*, 1135.

[173] G. S. May, S. M. Sze, *Fundamentals of Semiconductor Fabrication*, Wiley, **2001**.

[174] Y. L. Li, E. Kroke, R. Riedel, C. Fasel, C. Gervais, F. Babonneau, *Applied Organometallic Chemistry* **2001**, *15*, 820.

[175] G. Socrates, *Infrared Characteristics Group Frequencies Tables and Charts*, II ed., John Wiley & Sons, **1994**.

[176] F. Tuinstra, J. L. Koenig, *Journal of Chemical Physics* **1970**, *53*, 1126.

[177] S. Trassl, G. Motz, E. Rossler, G. Ziegler, *Journal of the American Ceramic Society* **2002**, *85*, 239.

[178] N. Janakiraman, F. Aldinger, *Journal of the European Ceramic Society* **2009**, *29*, 163.

[179] A. Saha, R. Raj, D. L. Williamson, *Journal of the American Ceramic Society* **2006**, *89*, 2188.

[180] J. B. Peri, *Journal of Physical Chemistry* **1965**, *69*, 220.

[181] A. Fissel, B. Schroter, W. Richter, *Applied Physics Letters* **1995**, *66*, 3182.

[182] A. A. Lebedev, *Semiconductor Science and Technology* **2006**, *21*, R17.

[183] Y. Zhang, T. Ichihashi, E. Landree, F. Nihey, S. Iijima, *Science* **1999**, *285*, 1719.

[184] G. C. Xi, S. J. Yu, R. Zhang, M. Zhang, D. K. Ma, Y. T. Qian, *Journal of Physical Chemistry B* **2005**, *109*, 13200.

[185] X. Q. Chen, D. R. Cantrell, K. Kohlhaas, S. Stankovich, J. A. Ibers, M. Jaroniec, H. S. Gao, X. D. Li, R. S. Ruoff, *Chemistry of Materials* **2006**, *18*, 753.

[186] J. J. Schneider, R. C. Hoffmann, J. Engstler, O. Soffke, W. Jaegermann, A. Issanin, A. Klyszcz, *Advanced Materials* **2008**, *20*, 3383.

[187] N. Audebrand, C. Bourgel, D. Louer, *Powder Diffraction* **2006**, *21*, 190.

[188] M. Hanchen, V. Prigiobbe, R. Baciocchi, M. Mazzotti, *Chemical Engineering Science* **2008**, *63*, 1012.

[189] V. Vagvolgyi, R. L. Frost, M. Hales, A. Locke, J. Kristof, E. Horvath, *Journal of Thermal Analysis and Calorimetry* **2008**, *92*, 893.

[190] C. Chizallet, G. Costentin, H. Lauron-Pernot, J. M. Krafft, M. Che, F. Delbecq, P. Sautet, *Journal of Physical Chemistry C* **2008**, *112*, 19710.

[191] G. P. Summers, T. M. Wilson, B. T. Jeffries, H. T. Tohver, Y. Chen, M. M. Abraham, *Physical Review B* **1983**, *27*, 1283.

[192] R. Hacquart, J. M. Krafft, G. Costentin, J. Jupille, *Surface Science* **2005**, *595*, 172.

[193] S. Stankic, M. Muller, O. Diwald, M. Sterrer, E. Knozinger, J. Bernardi, *Angewandte Chemie-International Edition* **2005**, *44*, 4917.

[194] M. Anpo, Y. Yamada, Y. Kubokawa, S. Coluccia, A. Zecchina, M. Che, *Journal of the Chemical Society-Faraday Transactions I* **1988**, *84*, 751.

[195] E. Hammarberg, A. Prodi-Schwab, C. Feldmann, *Thin Solid Films* **2008**, *516*, 7437.

[196] H. Sobotta, H. Neumann, G. Kuhn, V. Riede, *Crystal Research and Technology* **1990**, *25*, 61.

[197] K. Nakamoto, *Infrared and Raman Spectra of Inorganic and Coordination Compounds*, John Wiley and Sons, **2009**.

[198] N. Barsan, U. Weimar, *Journal of Electroceramics* **2001**, *7*, 143.

[199] N. Yamazoe, K. Shimanoe, *Sensors and Actuators B-Chemical* **2008**, *128*, 566.

[200] A. Gurlo, *Chemphyschem* **2006**, *7*, 2041.

[201] T. Sahm, A. Gurlo, N. Barsan, U. Weimar, *Sensors and Actuators B-Chemical* **2006**, *118*, 78.

[202] T. Sahm, A. Gurlo, N. Barsan, U. Weimar, L. Madler, *Thin Solid Films* **2005**, *490*, 43.

[203] G. K. Mor, O. K. Varghese, M. Paulose, K. Shankar, C. A. Grimes, *Solar Energy Materials and Solar Cells* **2006**, *90*, 2011.

[204] Y. S. Wang, P. J. Thomas, P. O'Brien, *Journal of Physical Chemistry B* **2006**, *110*, 21412.

[205] Y. S. Wang, P. J. Thomas, P. O'Brien, *Journal of Physical Chemistry B* **2006**, *110*, 4099.

[206] P. Uthirakumar, B. Karunagaran, S. Nagarajan, E. K. Suh, C. H. Hong, *Journal of Crystal Growth* **2007**, *304*, 150.

[207] S. Ramanathan, S. Patibandla, S. Bandyopadhyay, J. D. Edwards, J. Anderson, *Journal of Materials Science-Materials in Electronics* **2006**, *17*, 651.

[208] R. Laiho, L. S. Vlasenko, M. P. Vlasenko, *Journal of Applied Physics* **2008**, *103*.

[209] L. A. Kappers, O. R. Gilliam, S. M. Evans, L. E. Halliburton, N. C. Giles, *Nuclear Instruments & Methods in Physics Research Section B-Beam Interactions with Materials and Atoms* **2008**, *266*, 2953.

[210] Y. Hu, H. J. Chen, *Materials Research Bulletin* **2008**, *43*, 2153.

[211] V. R. Galakhov, M. A. Korotin, N. A. Ovechkina, E. Z. Kurmaev, V. S. Gorshkov, D. G. Kellerman, S. Bartkowski, M. Neumann, *European Physical Journal B* **2000**, *14*, 281.

[212] A. Baykal, Y. Koseoglu, M. Senel, *Central European Journal of Chemistry* **2007**, *5*, 169.

[213] H. A. Kuska, M. T. Rogers, *Electron Spin Resonance of First Row Transition Metal Complex Ions*, Wiley & Sons, New-York - London - Sydney, **1968**.

[214] B. Bleaney, R. S. Rubins, in *Proceedings Physical Review, Vol. 119*, **1960**, p. 132.

[215] P. B. Dorain, *Physical Review* **1958**, *112*, 1058.

[216] T. P. Hall, W. Hayes, F. I. Williams, *Proceedings of the Physical Society of London* **1961**, *78*, 883.

[217] P. Auzins, J. W. Orton, J. E. Wertz, in *Paramagnetic Resonance, Proceedings of the 1st International Conference, Vol. 1*, Jerusalem, **1962**, p. 90.

[218] Z. Zhang, R. M. Liu, M. Zhao, Y. T. Qian, *Materials Chemistry and Physics* **2001**, *71*, 161.

[219] C. K. Xu, K. K. Yang, L. W. Huang, H. W. Wang, *Journal of Chemical Physics* **2009**, *130*.

[220] A. Lagashetty, V. Havanoor, S. Basavaraja, S. D. Balaji, A. Venkataraman, *Science and Technology of Advanced Materials* **2007**, *8*, 484.

[221] A. Gurlo, N. Barsan, U. Weimar, M. Ivanovskaya, A. Taurino, P. Siciliano, *Chemistry of Materials* **2003**, *15*, 4377.

[222] J. Gong, W. H. Butler, G. Zangari, *Nanoscale* **2010**, *2*, 778.

[223] K. Hamalainen, D. P. Siddons, J. B. Hastings, L. E. Berman, *Physical Review Letters* **1991**, *67*, 2850.

[224] P. Glatzel, U. Bergmann, *Coordination Chemistry Reviews* **2005**, *249*, 65.

Lebenslauf

Persönliche Daten

Geburtsdatum	10.07.1982
Geburtsort	Minsk / Belarus (Weißrussland)
Nationalität	belarussisch (weißrussisch)
Familienstand	ledig

Schulbildung:

09/1998 - 06/2000	Lyzeum an der Belarussischen Staatlichen Universität in Minsk, Belarus Abschluss: Allgemeine Hochschulreife, Note: Ausgezeichnet

Studium:

09/2000 - 06/2005	Belarussische Staatliche Universität, Fakultät für Chemie, Minsk, Belarus Abschluss: Diplom in Chemie, Note: Ausgezeichnet Thema der Diplomarbeit: „*Thermodynamic properties of Menthol*“

Berufstätigkeit:

09/2003 - 05/2005	Studentische Hilfskraft, Fachbereich für Physikalische Chemie, Belarussische Staatliche Universität
09/2005 - 11/2005	Wissenschaftlicher Assistent, Forschungslabor für Analytische und Physicalische Chemie, Belarussische Staatliche Universität
Seit 02/2006	Doktorand, Technische Universität Darmstadt, Fachbereich Chemie, Eduard-Zintl-Institut für Anorganische und Physikalische Chemie, Arbeitsgruppe Prof. Schneider

Sonstiges:

Sprachkenntnisse	Weißrussisch: Muttersprache Russisch: Muttersprache Englisch: verhandlungssicher Deutsch: verhandlungssicher

Darmstadt, den
Heidelbergerstr. 30A
64285, Darmstadt

Eidesstattliche Erklärung

Ich erkläre hiermit an Eides Statt, dass ich meine Dissertation selbständig und nur mit den angegebenen Hilfsmitteln angefertigt habe.

Mikhail Pashchanka

Darmstadt, den
Heidelbergerstr. 30A
64285, Darmstadt

Erklärung

Ich erkläre hiermit, noch keinen Promotionsversuch unternommen zu haben.

Mikhail Pashchanka